

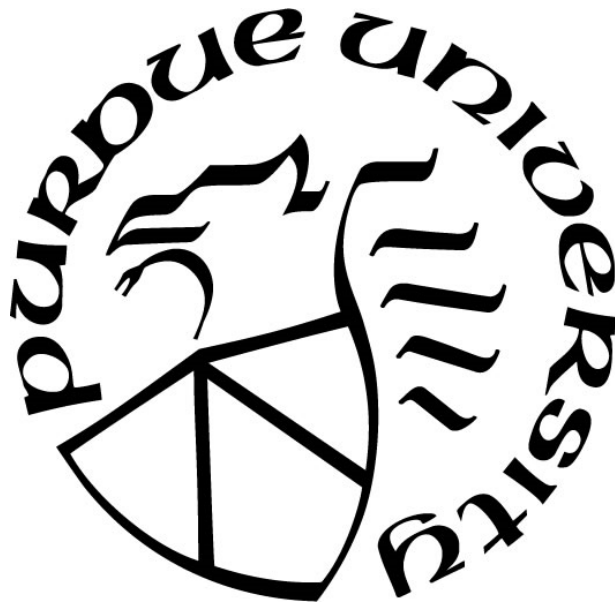
**INTERDIFFUSION BETWEEN A NI-CR ALLOY AND W, AND THE USE
OF NI FOR LIQUID PHASE BONDING OF ZRC/W COMPOSITES**

by
Supattra Singnisai

A Dissertation

*Submitted to the Faculty of Purdue University
In Partial Fulfillment of the Requirements for the degree of*

Doctor of Philosophy



School of Materials Engineering

West Lafayette, Indiana

May 2021

**THE PURDUE UNIVERSITY GRADUATE SCHOOL
STATEMENT OF COMMITTEE APPROVAL**

Dr. Kenneth Sandhage, Chair
School of Materials Engineering

Dr. John Blendell
School of Materials Engineering

Dr. Mysore Dayananda
School of Materials Engineering

Dr. Eric Kvam
School of Materials Engineering

Approved by:

Dr. David Bahr

*To my supervisor, and instructors who patiently provided guidance and to my family and friends
who kindly provided support*

ACKNOWLEDGMENTS

Funding for this research was provided by the U.S. Department of Energy, award No. DE-EE0008369: Robust, High-Temperature Heat Exchangers.

TABLE OF CONTENTS

LIST OF TABLES.....	7
LIST OF FIGURES	8
ABBREVIATIONS	12
ABSTRACT.....	13
1. INTERDIFFUSION STUDY BETWEEN NICKEL CHROMIUM ALLOY AND TUNGSTEN IN THE 1000 °C – 1200 °C TEMPERATURE RANGE	15
1.1 Abstract.....	15
1.2 Introduction.....	15
1.3 Experimental procedure	21
1.4 Theoretical background	28
1.5 Results.....	32
1.5.1 Microstructure of diffusion couples.....	32
1.5.2 Calculation of interdiffusion coefficients	39
1.5.3 Activation Energy for diffusion.....	45
1.6 Discussion.....	46
1.7 Conclusion	49
2. EFFECT OF GRAIN SIZE OF TUNGSTEN ON THE INTERDIFFUSION OF NICKEL CHROMIUM ALLOY/ TUNGSTEN DIFFUSION COUPLES.....	50
2.1 Abstract.....	50
2.2 Introduction.....	50
2.3 Experimental procedure	51
2.3.1 Production of fine grain tungsten plate.....	51
2.3.2 Diffusion bonding and annealing of FGW diffusion couples.....	54
2.3.3 Investigation of diffusion of Ni and Cr into FGW using TEM	57
2.3.4 Method used to obtain grain size measurement.....	57
2.4 Results.....	58
2.4.1 Characterization of as-received nano W powder.....	58
2.4.2 Microstructure of the produced FGW.....	60
2.4.3 Diffusion of Ni and Cr into W with different grain size.....	64

2.5	Discussion.....	70
2.6	Conclusion	71
3.	LIQUID PHASE BONDING OF ZrC/W TO ZrC/W WITH NICKEL-INTERLAYER ...	72
3.1	Abstract.....	72
3.2	Introduction.....	72
3.3	Experimental Procedure.....	75
3.3.1	Production of ZrC/W-based composite via DCP process.....	75
3.3.2	Removal of residual Cu from the DCP-derived ZrC/W-based composite	77
3.3.3	Liquid phase bonding of ZrC/W to ZrC/W	77
3.3.4	Wetting experiment	80
3.4	Results.....	81
3.4.1	Removal of residual Cu from the ZrC/W-based composite	81
3.4.2	Microstructure of the bonded materials.....	83
3.4.3	Effect of bonding temperature on the mechanical behavior of bonded ZrC/W specimens.....	88
3.4.4	Wetting behavior of Ni on ZrC/W.....	91
3.5	Discussion.....	93
3.6	Conclusion	95
	APPENDIX A. SUPPLEMENTARY MATERIALS FOR CHAPTER 1: INTERDIFFUSION STUDY BETWEEN NICKEL CHROMIUM ALLOY AND TUNGSTEN IN THE 1000 °C-1200°C TEMPERATURE RANGE	96
	APPENDIX B. SUPPLEMENTARY MATERIALS FOR CHAPTER 2: EFFECT OF GRAIN SIZE OF TUNGSTEN ON THE INTERDIFFUSION OF NICKEL CHROMIUM ALLOY/ TUNGSTEN DIFFUSION COUPLES.....	103
	APPENDIX C. SUPPLEMENTARY MATERIALS FOR CHAPTER 3: LIQUID PHASE BONDING OF ZrC/W TO ZrC/W WITH NICKEL-INTERLAYER.....	107
	REFERENCES	113

LIST OF TABLES

Table 1.1. Location of Matano plane as calculated from concentration profiles.....	39
Table 1.2. Composition at the α/β interface (x_1)	41
Table 1.3. Average effective interdiffusion coefficients and characteristic interdiffusion depths for the regions on the α -phase (Ni-rich) and the β -phase (W-rich)	43
Table 1.4. Activation energies determined from average effective interdiffusion coefficients....	45
Table 2.1. Average effective interdiffusion coefficients and characteristic depth of penetration for the regions on the LHS, and on the RHS of the α/β interface for the FGW/80Ni20Cr couple, and the LGW/80Ni20Cr couple.....	65
Table 3.1. Chemical composition (at%) and possible phase of each spot in Figure 3.19.....	91
Table 3.2. Student's t-test analyses of difference in the shear strength data for different bonding temperatures.....	94

LIST OF FIGURES

Figure 1.1. Ni-W phase diagram [32]	19
Figure 1.2. Ni-Cr-W phase diagrams at 1000°C and 1250°C [33].....	20
Figure 1.3. BSE image of polished and etched cross-section of the starting W plate (99.95% purity, Midwest Tungsten Inc., USA)	21
Figure 1.4. a) BSE image with the SEM-EDX elemental maps from a cross-section of the annealed 80Ni20Cr button, b) X-ray diffraction patterns of the annealed 80Ni20Cr button with Cu used as reference.....	23
Figure 1.5. X-ray diffraction patterns of the as-received alumina powders ($\leq 10\mu\text{m}$ average particle size, 99.5% purity, Sigma Aldrich, USA).....	24
Figure 1.6. BSE image and SEM-EDX elemental maps of alumina particles on a polished W plate	25
Figure 1.7. Schematic drawing of the Mo-based fixture for bonding the 80Ni20Cr/W diffusion couples	26
Figure 1.8. Schematic drawing of a set up for quenching diffusion couples.....	26
Figure 1.9. SE image and EDX elemental maps from a cross-section of a Ni-W-Cr standard	28
Figure 1.10. BSE image of polished cross-section from a 80Ni20Cr/W diffusion couple annealed at 1200 °C for 50 hours	33
Figure 1.11. Diffusion path from the 80Ni20Cr/W couples annealed at 1000°C for 100 hours overlaying on the 1000°C isothermal cross-section of the Ni-Cr-W phase diagram [33]	33
Figure 1.12. X-ray diffraction patterns from a diffusion couple annealed at a) 1000°C for 100 hours, and b) 1200°C for 100 hours.....	34
Figure 1.13. BSE images and SEM-EDX elemental maps from the polished cross-section of the 80Ni20Cr/W diffusion couples: a) annealed at 1000°C for 100 hours, and b) annealed at 1200°C for 100 hours	35
Figure 1.14. Concentration profile of 80Ni20Cr/W couple annealed at a) 1000 °C for 50 hours, b) 1000 °C for 100 hours, c) 1100 °C for 50 hours, d) 1100 °C for 100 hours, e) 1200 °C for 50 hours, and f) 1200 °C for 100 hours. The vertical dash lines represent the locations of Matano planes, and the vertical solid lines represent the locations of the α/β interface.	36
Figure 1.15. Magnified view of plots in Figure 1.14 showing Cr concentration profiles in the β -phase	37
Figure 1.16. Magnified view of plots in Figure 1.14 showing Ni concentration profiles in the β -phase	38

Figure 1.17. C_i , Y_i , and J_i (calculated from eq. 1.5) plots from the 80Ni20Cr/W diffusion couple annealed at 1200°C for 100 hours.....	40
Figure 1.18. Diffusion profiles from all diffusion couples as calculated by eq. 1.17 and 1.18 (lines) comparing with the experimental data (dots): a) 1000 °C for 50 hours, b) 1000 °C for 100 hours, c) 1100 °C for 50 hours, d) 1100 °C for 100 hours, e) 1200 °C for 50 hours, and f) 1200 °C for 100 hours. The vertical dash lines represent the locations of Matano planes, and the vertical solid line represent the locations of the α/β interface.	44
Figure 1.19. Arrhenius plot of $\ln(D_i, \Delta C_{eff})$ as a function of $1/T$	46
Figure 2.1. Temperature and profiles for producing FGW specimen via a pre-compaction and pressureless sintering method.	52
Figure 2.2. Temperature and pressure profiles for producing FGW discs via the hot pressing using two different conditions; a) 3 hours at a peak temperature of 1250 °C (HP1250C), and b) 1.5 hours at a peak temperature of 1500 °C (HP1500C)	54
Figure 2.3. Schematic drawing of the Mo-based fixture for bonding the 80Ni20Cr/FGW diffusion couple.....	55
Figure 2.4. Schematic drawing of a set up for quenching diffusion couples.....	56
Figure 2.5. a) X-ray diffraction patterns of the as-received "80-nm" W powder, and b) TEM image of the powder together with the SAED analysis in c).....	59
Figure 2.6. STEM-EDX elemental maps of the as-received "80-nm" W powders	60
Figure 2.7. SE images of fracture surfaces from FGW disks produced via: a) compaction followed by pressureless sintering for 50 hours at 1250 °C, b) hot pressing at peak temperature of 1250 °C for 3 hours, and c) hot pressing at peak temperature of 1500 °C for 1.5 hours.	61
Figure 2.8. SEM images from the FGW_HP1500C disk after annealing at 1200°C for 50 hours: a) a fracture surface, b) a polished cross-section, and c) the thermal etched polished cross-section.	61
Figure 2.9. Different graphical displays generated from EBSPs collected from the polished cross-section of the FGW_HP1500C disk.....	63
Figure 2.10. BSE images of an etched polished cross-section of the LGW (99.95% purity, Midwest Tungsten Inc., USA) used in this study	64
Figure 2.11. Concentration profiles from FGW/80Ni20Cr couple annealed at 1000 °C for 50 hours (in black color), and LGW/80Ni20Cr couple annealed at 1000 °C for 50 hours (in red color) ...	66
Figure 2.12. Elemental maps obtained from SEM-EDX analyses of polished cross-sections of the FGW/80Ni20Cr and LGW/80Ni20Cr diffusion couples annealed at 1000 °C for 50 hours	67
Figure 2.13. High-resolution STEM-EDX analyses of an ion-milled cross-section of a FGW/80Ni20Cr diffusion couple annealed at 1000°C for 50 hours; a) elemental maps, b) line scans showing composition deviation across the W grains as indicated by the dotted lines in a)	68

Figure 2.14. SAED patterns from two regions; the Ni-rich phase (box A), and the W-rich phase (box B) together with the measure composition of each regio	69
Figure 3.1. Ni-W phase diagram [32]	74
Figure 3.2. Ni-ZrC phase diagram[77]	74
Figure 3.3. Schematic illustration of the assembly for static reactive melt infiltration	76
Figure 3.4. XRD pattern obtained from a plate generated by the static reactive infiltration DCP method.....	77
Figure 3.5. Elemental mapping of ZrC/W substrate after etching in nitric acid (15.8 M) for 30 minutes.....	78
Figure 3.6. Assembly for bonding ZrC/W shear test specimen.....	79
Figure 3.7. Schematic illustration of the shear test assembly used in this study	80
Figure 3.8. Photographs of a DCP-derived ZrC/W-based specimen: a) after polishing, b) after annealing in Ar atmosphere at 1100 °C for 4 hours, and c) after etching in nitric acid for 1 hour	81
Figure 3.9. Weight loss of DCP-derived ZrC/W composite specimens as a function of annealing time at 1100 °C in Ar atmosphere.....	82
Figure 3.10. Elemental mapping of cross-section of a ZrC/W specimen annealed at 1100 °C for 40 hours after etching in nitric acid for 1 hour a) at the middle of the cross-section, b) at the edge of the cross-section.....	83
Figure 3.11. Collages of BSE images from ZrC/W specimen bonded at a) 1300 °C, b) 1400 °C, and c) 1500 °C.....	84
Figure 3.12. EDX elemental maps of polished cross-sections at the bonded interfaces from specimens joined at 1300 °C, 1400 °C, and 1500 °C	85
Figure 3.13. Distribution of elements away from the bonding interface from the specimen bonded at a) 1300°C for 2 hours, b)1400°C for 2 hours, and c) 1500°C for 2 hours.....	86
Figure 3.14. Compositions at the bonded interface regions for different bonding temperatures .	87
Figure 3.15. Effect of bonding temperature on the shear strength of the bonded ZrC/W specimens	88
Figure 3.16. Collage of SE images from a fracture surface obtained from the specimens that were bonded at 1400 °C for 2 hours; a) a specimen that failed within ZrC/W-based composite, and b) a fracture surface from a specimen that fail at the bonded interface	89
Figure 3.17. BSE image and EDX elemental maps of a fracture surface from the debonded ZrC/W at a high magnification.....	90
Figure 3.18. Ni-Cu phase diagram [80]	91
Figure 3.19. BSE image and EDX elemental maps of a top view of a ZrC/W specimen after exposure to Ni foil at 1400 °C for 30 minutes	92

Figure 3.20. BSE image with EDX mapping of the bonded interface at higher magnification from a polished cross-section of a specimen bonded at a)1300 °C for 2 hours, b)1400 °C for 2 hours, and c)1500 °C for 2 hours 93

ABBREVIATIONS

Acronym	Definition
DCP	Displacive Compensation of Porosity
IMC	Intermetallic Compound
EDM	Electric Discharge Machining
UHP Ar	Ultra-High Purity Argon
SEM-EDX	Scanning Electron Microscopy with Energy Dispersive X-ray spectroscopy
ICP-MS	Inductively Coupled Plasma Mass Spectrometry
LHS	Left-hand Side
RHS	Right-hand Side
LGW	Large grain tungsten
FGW	Fine grain tungsten
EBSD	Electron Backscatter Diffraction
EBSP	Electron Backscatter Diffraction Pattern
TEM	Transmission Electron Microscope
STEM-EDX	Scanning Transmission Electron Microscope with Energy Dispersive X-ray spectroscopy
SAED	Selected Area Diffraction
BSE	Back-scatter Electron
SE	Secondary Electron
MLI	Mean Linear Intercept

ABSTRACT

The Ni-Cr-W system is of significant technological and scientific interest due to the oxidation resistance provided by Cr and the excellent high-temperature mechanical properties of Ni-Cr-based alloys and W. Several active phenomena during the processing of such materials (such as solidification, precipitation, sintering) or during the service of such materials (such as oxidation) are governed by diffusion of elements in this system. In this study, interdiffusion in the Ni-Cr-W ternary system was investigated at 1000-1200°C. Diffusion couples, consisting of a Ni-20wt%Cr alloy and pure W, were used to evaluate interdiffusion coefficients in the Ni-Cr-W system using a method developed by Dayananda and coworkers. The effective average interdiffusion coefficients obtained by this method were used to reproduce a concentration profile with a good fit to the profiles as measured from experiments. The activation energies for interdiffusion of Ni, Cr, and W were within the range of 318 ± 27 kJ/mol for diffusion in the Ni-rich phase, and 271 ± 32 kJ/mol for diffusion in the W-rich phase. These values were consistent with values reported in other studies of similar systems. The role of W grain boundaries on the interdiffusion behavior of Ni, Cr, and W was also investigated. This study was conducted at 1000°C using a diffusion couple between fine-grained, hot-pressed W ($d_{ave}= 2.3 \mu\text{m}$) and a Ni-20wt%Cr alloy. Although a slight preference for Ni and Cr diffusion along W grain boundaries was detected through STEM-EDX analysis, the temperature was sufficiently high that the volume diffusion rates of Ni and Cr were appreciable compared to the grain boundary diffusion of Ni and Cr, so that the overall concentration profiles were similar to those obtained from diffusion couples with coarse-grained W ($d_{ave}=29.3 \mu\text{m}$).

A liquid phase bonding technique to join ZrC/W-based composites was also evaluated. ZrC/W composites exhibit superior thermal conductivity and failure strength at high temperatures relative to nickel-based alloys. ZrC/W composites produced by the Displacive Compensation of Porosity (DCP) method were joined together by a liquid-phase bonding technique using Ni as an interlayer material. The effects of the bonding temperatures, ranging from 1300-1500°C, on the microstructure and microchemistry of the bonded area, and on the bonding strength at room temperature, were investigated. The cross-section from a specimen bonded at 1300 °C exhibited several 25 – 90 μm voids along the bonded interface while the cross-sections from specimens bonded at 1400 °C and 1500 °C exhibited no such voids. The Zr, and C contents at the bonded

interface increased as the bonding temperature increased from 1400 °C to 1500 °C. On the other hand, the Ni content at the bonded interface area decreased as the bonding temperature increased. The shear strength values obtained after bonding at 1300-1500°C for the same time of 2 hours were similar and in the range of 127.0 ± 63.0 MPa.

1. INTERDIFFUSION STUDY BETWEEN NICKEL CHROMIUM ALLOY AND TUNGSTEN IN THE 1000 °C – 1200 °C TEMPERATURE RANGE

1.1 Abstract

Interdiffusion in the Ni-Cr-W ternary system was investigated with solid-solid diffusion couples assembled with disks of a 80Ni20Cr (α) alloy and pure W (β) after annealing at temperatures of 1000°C, 1100°C, and 1200°C for various times. A planar α/β interface developed in the diffusion zones of all annealed couples with the growth of the α phase at the expense of the β phase. Average effective interdiffusion coefficient for Ni, Cr and W were estimated in both α and β phases using a method developed by Dayananda from profiles of interdiffusion fluxes directly determined from concentration profiles. The average effective interdiffusion coefficients determined from couples annealed at the same temperature but for different diffusion times yielded similar values of interdiffusion coefficients. The average effective interdiffusion coefficients were successfully employed to reproduce the experimental concentration profiles through error function solutions appropriate for two-phase solid-solid diffusion couples. Experimental diffusion paths determined from the concentration profiles were represented on ternary isotherms. The activation energies for diffusion of W, Cr, and Ni in both α and β phases were determined from the average effective interdiffusion coefficients evaluated at different temperatures on the basis of Arrhenius plots. The activation energies for diffusion of W, Cr, and Ni on the Ni-rich region (α -phase) were higher than those for the W-rich region (β -phase). However, the activation energies for interdiffusion of each element in a given phase, were similar with values in the range of 318 ± 27 kJ/mol for the α -phase, and 271 ± 32 kJ/mol for the β -phase. These values were consistent with those reported in other studies. Characteristic interdiffusion depths were also determined for each component on either side of the planar α/β interface for all diffusion couples.

1.2 Introduction

Several active phenomena during the processing of materials (such as solidification, precipitation, sintering) or during service of materials (such as oxidation), are governed by diffusion of elements in the system [1]–[7]; hence, understanding diffusion of elements in solids is key for understanding, designing, and optimizing materials processing and performance.

Multicomponent systems, like Ni-based superalloys or emerging high-entropy alloys, are considered among the top candidates for several high-temperature applications in corrosive environments; such as high-temperature heat exchangers, heat engines, turbine blades, and nuclear reactors [8]–[15]. Many processing steps and applications of such alloys involve the materials being held at high temperatures [8], [11], [13], [16]; hence, understanding diffusion phenomena in multicomponent systems is vital to tailor the metal alloys to a given application as well as to anticipate their life span and failure mechanisms.

The Ni-Cr-W system is of great technological and scientific interest due to the oxidation resistance provided by Cr and the excellent high-temperature mechanical properties of Ni and W [10], [14], [17]. The work in this thesis was funded by the U.S. Department of Energy (DOE) toward the development of a ZrC/W based heat exchanger. As part of the development, chemical stability testing of the ZrC/W composite in supercritical CO₂ has been conducted. These tests indicated that the ZrC/W composite is corroded in high temperature supercritical CO₂. Applying a protective coating layer is one of several possible approaches to mitigate the corrosion of ZrC/W. A study by Firouzdor, et al. [18] suggested that a Ni-based alloy with Cr can form a protective chrome oxide scale under a high service temperature in supercritical CO₂. To determine a proper bonding process and a proper thickness to achieve an effective protective layer for the given service condition, one needs to understand the interdiffusion and reaction of elements at the bonded interface. Dense ZrC/W prepared by the Displacive Compensation of Porosity (DCP) process consists of W-based particles in a ZrC-based matrix in the amounts of 34 vol% and 55 vol%, respectively [19]. However, including multiple phases into one diffusion study tended to complicate the analysis process. Hence, in this study, a Ni-Cr alloy was selected to be diffusion bonded to pure W first to serve as an initial diffusion study for such an application.

The diffusion couple technique is a direct method for studying solid-state diffusion that is widely used in many studies [20]. By using only a single diffusion couple, the interdiffusion coefficient with respect to temperature and composition in a binary system can be extracted by Matano-based analytical methods, since there is only one interdiffusion coefficient to describe the diffusion at that particular temperature and composition [21]. Therefore, the diffusion behavior in binary systems can be relatively well understood. However, materials being used in industrial applications typically consist of more than two components. Unlike diffusion in binary systems, the diffusion behavior of multicomponent systems can be more complicated since there are more

combinations of interactions between different elements in the system. To evaluate diffusion at any temperature and composition, one needs to know $(n-1)^2$ interdiffusion coefficients, where n is the number of components in the system [1]. Several approaches, including the Matano-based approaches, and numerical inverse approaches have been pursued [22]. In order to use the numerical inverse approach, thermodynamic and atomic mobility data are needed as inputs for the reverse numerical fitting [22], and reliable databases are not fully available for this system yet. In this study, the Matano-based approach was applied to the study of the ternary Ni-Cr-W system.

While diffusion of one element through a crystalline lattice may be relatively well understood and described by Fick's laws with a single interdiffusion coefficient, simultaneous diffusion of several elements within a material can be more difficult to model and interpret [23]. Such a case has been studied by Dayananda and Sohn [2] who proposed analytical models for estimating interdiffusion in a ternary system using a single diffusion couple. This model considers the effects of compositional gradients on the interdiffusion coefficients. They proposed a Matano-based analytical approach that uses only a single diffusion couple to derive average interdiffusion coefficients over selected composition ranges in an n -component system [2]. The analysis to calculate average interdiffusion coefficients applying their proposed method can be processed in Multidiflux 1.2 software developed by Dayananda, Ram-mohan, and Day [24]–[26]. This method has been applied to the Ni-Cr-Al system at 1100 °C, the Fe-Ni-Al system at 1000 °C, and the Cu-Ni-Zn system at 775 °C [2], [27]. The goal for this study is to apply this method to determine diffusion coefficients in Ni-Cr-W system. However, the published version of this software was most suitable for single phase diffusion couples. Therefore, the software was not satisfactory in this study where two phases, Ni-Cr phase (α), and W-rich phase (β), were involved in the diffusion zone. Hence, an alternative approach involving the determination of average effective interdiffusion coefficients and characteristic diffusion depths for each component on either side of the α/β interface were employed on the basis of studies by Dayananda and coworkers [27]–[29].

In 1974, Karpinos, et al. [30] studied diffusion in the Ni-Cr-W system at 1000 -1200 °C. In their study, they did not use the conventional diffusion couple technique of measuring a diffusion profile from a planar interface between two terminal alloys. They instead measured a diffusion profile from the diffusion zone of a 0.3-mm-diameter tungsten fiber in a Nichrome matrix. They reported the diffusion coefficients, which they called “mutual diffusion coefficients”, at only 1100 °C for different W compositions ranging from 5 wt% to 35 wt%. The diffusion coefficient values

reported did not differentiate between elements involved in an interdiffusion process (e.g. diffusion of W into Ni-Cr matrix or diffusion of Ni, Cr into W fiber).

Inomata and Kajihara [31] studied solid-state diffusion in the binary Ni-W system in the temperature range of 750 – 900 °C. They reported the formation of Ni₄W growing toward Ni. The formation of the Ni₄W layer was governed by a combination of grain boundary diffusion and volume diffusion, while a reduced contribution of boundary diffusion was observed at 900 °C from their study. From the Ni-W phase diagram [32] (Figure 1.1), no Ni-W intermetallic compounds are stable above 1068 °C.

From Ni-Cr-W phase diagrams at 1000 °C and 1250 °C [33] , as shown in Figure 1.2, possible diffusion paths between Ni-Cr alloys with ≤ 20 at% (37wt%) Cr and a pure W were not likely to cross into stability regions with the σ -phase (Cr_{0.57}Ni_{0.36}W_{0.07}). Hence, to avoid complications involving intermetallic compound formation, the present diffusion study was conducted in the 1000-1200 °C temperature range with 80Ni20Cr (Ni-20wt%Cr) / W diffusion couples.

The purpose of this study is to investigate interdiffusion behavior in the Ni-Cr-W system to obtain a better understanding as to how Ni, Cr, and W interdiffuse in α and β phases at different temperatures. The average effective interdiffusion coefficients representing interdiffusion of each element were determined in each phase region developed in the diffusion zone from Ni-Cr (α) alloy vs W (β) diffusion couple experiments conducted at 1000 °C, 1100 °C, and 1200 °C. For each temperature, the diffusion couples were annealed for two times of 50 hours and 100 hours to verify the validity of the calculated diffusion coefficients at each temperature. The average effective interdiffusion coefficients determined from couples annealed at three different temperatures were used to calculate an activation energy for diffusion for each diffusing element in both α and β phases.

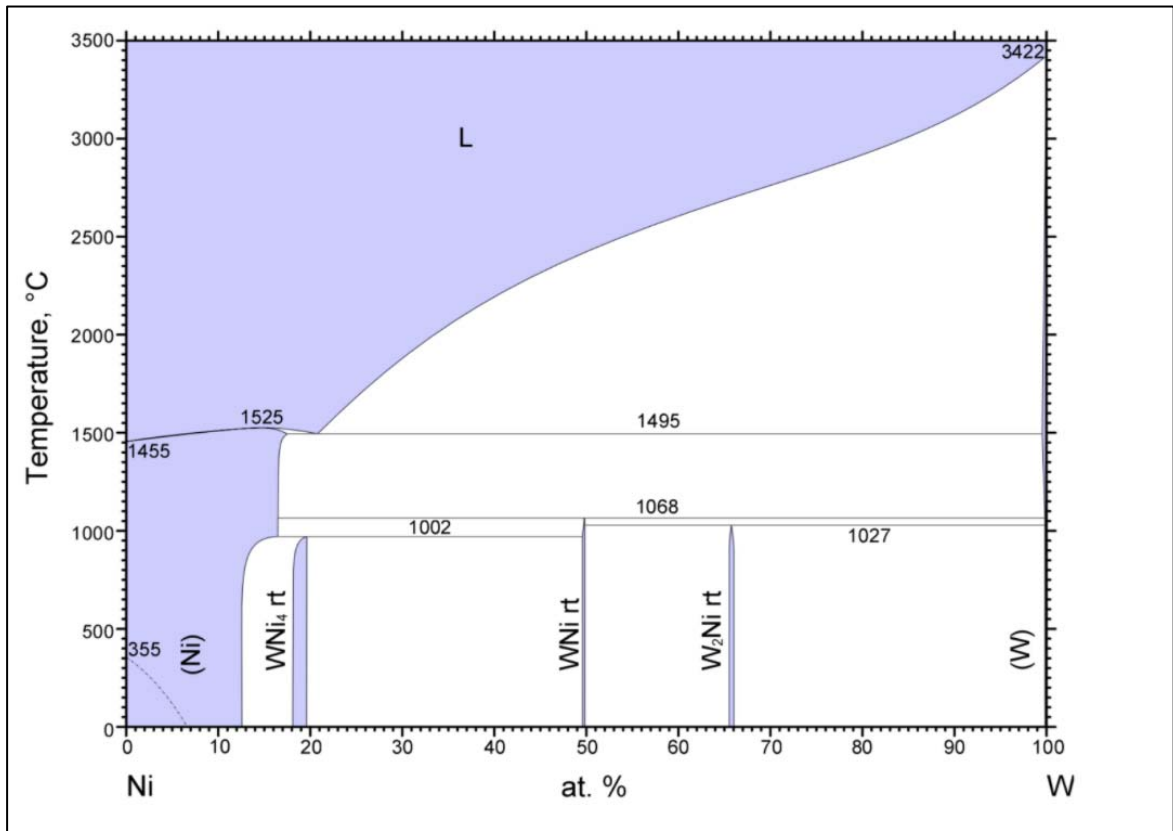


Figure 1.1. Ni-W phase diagram [32]

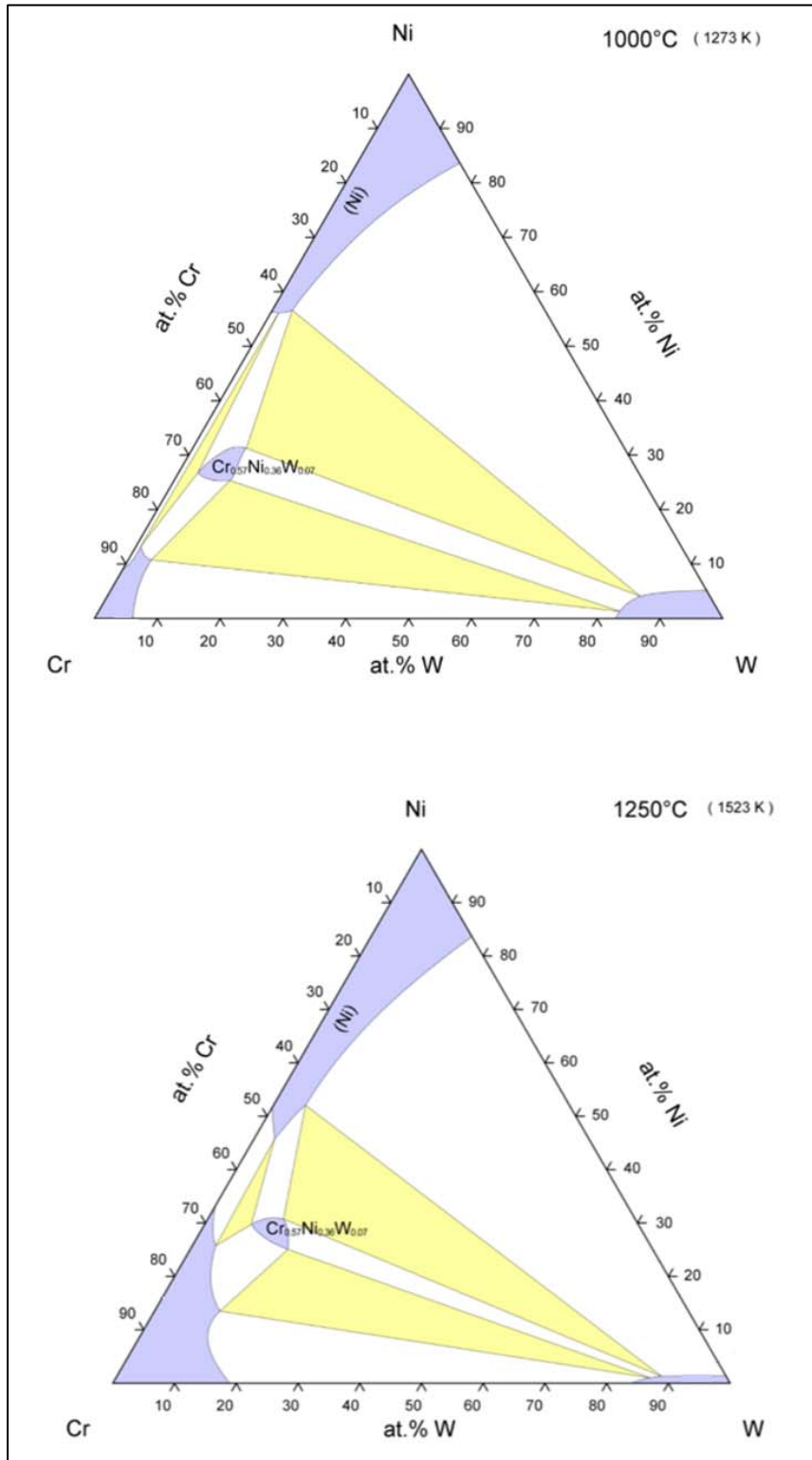


Figure 1.2. Ni-Cr-W phase diagrams at 1000°C and 1250°C [33]

1.3 Experimental procedure

The diffusion couples were prepared from a commercially available, 1-mm-thick tungsten sheet (Midwest Tungsten Service, Willowbrook, IL USA, 99.95% purity, 0.002%Fe, 0.001%Al, 0.001%Ni, 0.001%Si, 0.001%C, 0.002%Ni₂, 0.005%O₂) and in-house alloyed Nichrome (80Ni20Cr) generated by melting the pure components. The as-received W plate possessed density of $19.1 \pm 0.1 \text{ g/cm}^3$, which corresponded to a relative density of $99.0 \pm 0.7\%$. A backscattered electron (BSE) image of a polished cross-section of the W plate is shown in Figure 1.3. Prior to imaging, the polished cross-section was etched by immersion in a mixture of 3 parts of hydrochloric acid (12.1 M) and 1 part of nitric acid (15.8 M) at 80 °C for 2 minutes. The micrograph was used to determine \bar{L}_3 (the mean intercept length of three-dimensional bodies) which represents the average grain size of the specimen [34]. The \bar{L}_3 measurement was conducted, following the standardize method indicated in ASTM E1382-97 standard [35], by placing random circles on the micrograph and counting the number of grains intercepted by perimeter of the circles. The \bar{L}_3 as determined from the micrograph of the polished and etched W plate was $29.3 \pm 3.2 \text{ }\mu\text{m}$. Details of the \bar{L}_3 measurement from micrographs in this study are provided in Appendix A1.

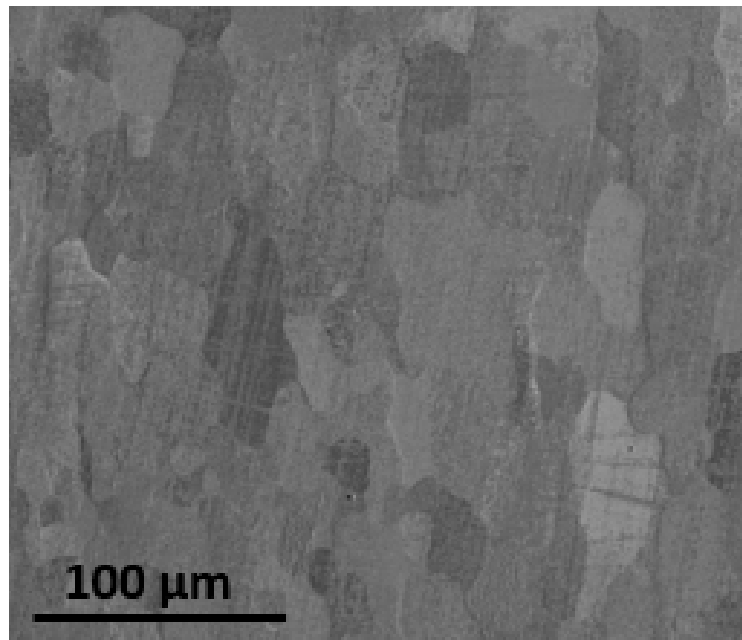


Figure 1.3. BSE image of polished and etched cross-section of the starting W plate (99.95% purity, Midwest Tungsten Inc., USA)

The Ni-Cr alloy was prepared by arc melting nickel (Ni, Alfa Aesar, Tewksbury, MA, USA, 99.5% purity, 150 ppm C, 100 ppm Cu, 200 ppm Mg, 10 ppm S, 40 ppm Ti, 10 ppm Co, 10 ppm Fe, 1800 ppm Mn, 200 ppm Si) and chromium (Zr Industrial Ltd, Shanghai, China, 99.9% purity, C 0.007%, Cu 0.002%, Fe 0.006%, P 0.002%, Si 0.006%, Al 0.005%, Cr balance) in an Ar atmosphere (Airgas, UHP Ar 99.999% purity). The arc melter used in this study consisted of a single arc electrode in a glass cylinder chamber and a chilled Cu hearth. Weighed amounts of the pure components were piled together on the chilled Cu hearth. A Ti getter was also placed on the hearth beside the pile of pure components. Prior to melting, the furnace chamber was evacuated (80 mbar) and backfilled 3 times with an Ar (UHP, 99.999%, Airgas USA). Prior to melting the pure component, the arc was focused on the Ti first to initiate the gettering of residual oxygen. To ensure homogenization of the melt, the melted button was flipped over and re-melted, and this process was repeated 5 times. After melting, the button was annealed in an Ar atmosphere at 1250 °C for 50 hours to homogenize the alloy [36], [37]. A BSE image with the SEM-EDX (FEI Nova Nano SEM, with X-ray analysis EDX Oxford Aztec Xstream-2 silicon drift detector) elemental maps from a cross-section of the annealed button is shown in Figure 1.4 a). From the elemental maps, Ni and Cr were uniformly distributed. XRD analysis (D2 Phaser diffractometer, Bruker, Billerica, MA, USA) was conducted on the annealed 80Ni20Cr button, and the X-ray diffraction pattern is presented in Figure 1.4 b). The Cu peaks in the X-ray pattern were used as a reference for x-offset in the analysis. The locations of the Ni(200) peak, and the Ni(400) peak were 0.8 to 1.5 degrees less than the peaks from pure Ni (PDF 00-004-0850) because of the Cr dissolved in the Ni lattice. The atomic radius of Cr is 0.166 nm which is larger than the values of 0.149 nm for Ni [38].

Prior to imaging, the polished cross-section was etched in 15.8 M Nitric acid for 3 minutes to reveal microstructure of the alloy. The \bar{L}_3 as determined from the micrograph of the annealed 80Ni20Cr was $332.9 \pm 47.1 \mu\text{m}$. The bulk density of the annealed 80Ni20Cr is $8.5 \pm 0.1 \text{ g/cm}^3$. Densities of commercially available Ni-Cr alloys (Ni/14-64Cr) are in the range of 7.75-8.65 g/cm³ [39].

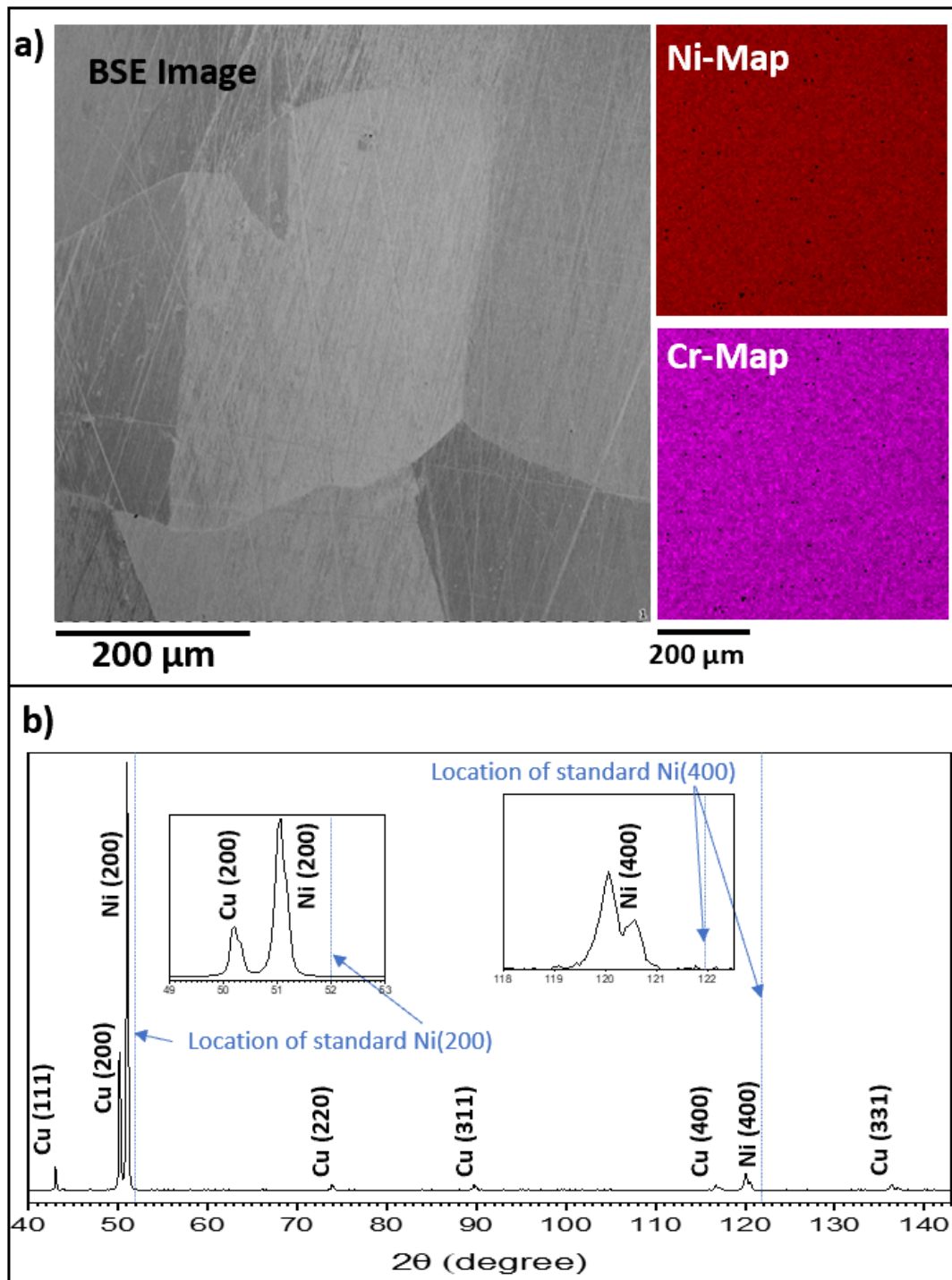


Figure 1.4. a) BSE image with the SEM-EDX elemental maps from a cross-section of the annealed 80Ni20Cr button, b) X-ray diffraction patterns of the annealed 80Ni20Cr button with Cu used as reference.

The metal specimens (W and 80Ni20Cr) were cut by electrical discharge machining (EDM, Mitsubishi FX20K) into rectangular plates with lateral dimensions of 10 mm x 12 mm. The surface to be diffusion bonded was mechanically polished with SiC paper (grit sizes 320-1200) and diamond paste down to a 1 μm finish. A final polishing was conducted with 0.05 μm colloidal silica. After polishing, the specimens were cleaned by sonication in acetone for 10 minutes.

Alumina powder (Aluminum oxide, Al_2O_3 , $\leq 10 \mu\text{m}$ average particle size, 99.5% purity, Sigma Aldrich, USA) was used as an inert marker in the diffusion experiments. An X-ray diffraction pattern of the as-received alumina powder is shown in Figure 1.5. For such purpose, alumina particles were deposited on the W surface using a dilute alumina (2 mg of alumina in 20 g of acetone) dispersion by sonication (Branson 3800 Tabletop ultrasonic), for 5 seconds. Excess liquid was removed by bringing a Kimwipe close to the edge of the droplet that was sitting on top of the W plate. The W plate with alumina powder was left to dry in air for 10 minutes to ensure that residual acetone had evaporated. A BSE image with SEM-EDX elemental maps showing the distribution of Alumina powder on a W plate is shown in Figure 1.6.

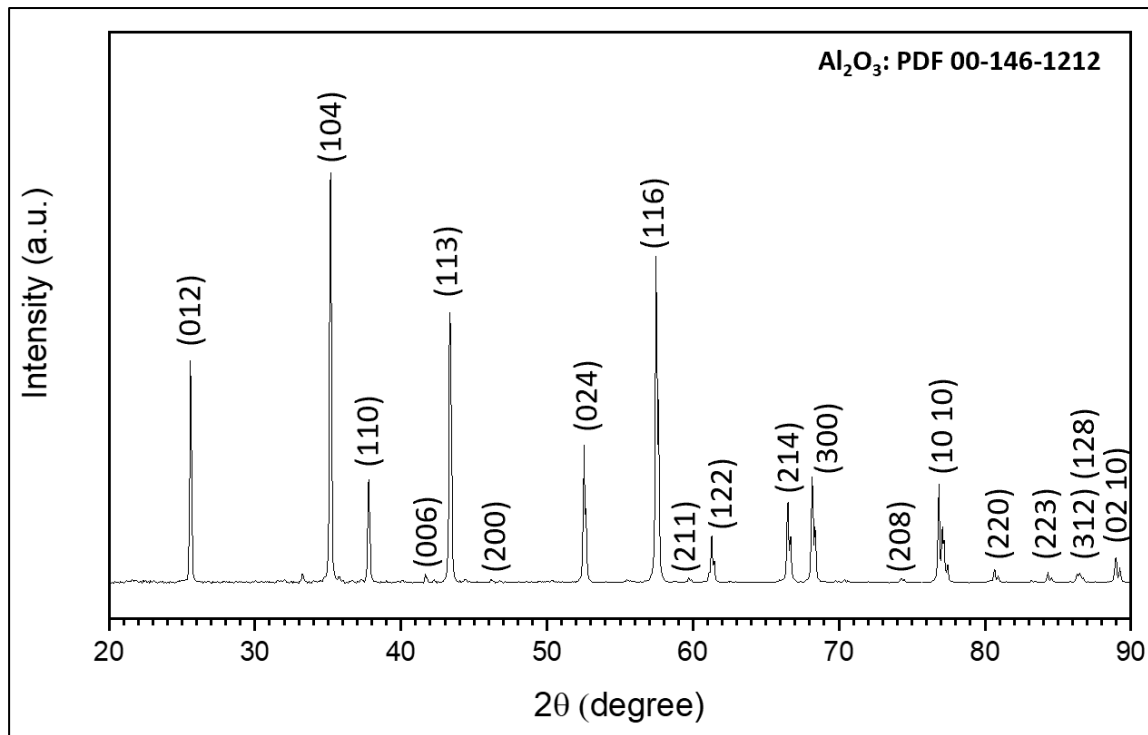


Figure 1.5. X-ray diffraction patterns of the as-received alumina powders ($\leq 10\mu\text{m}$ average particle size, 99.5% purity, Sigma Aldrich, USA)

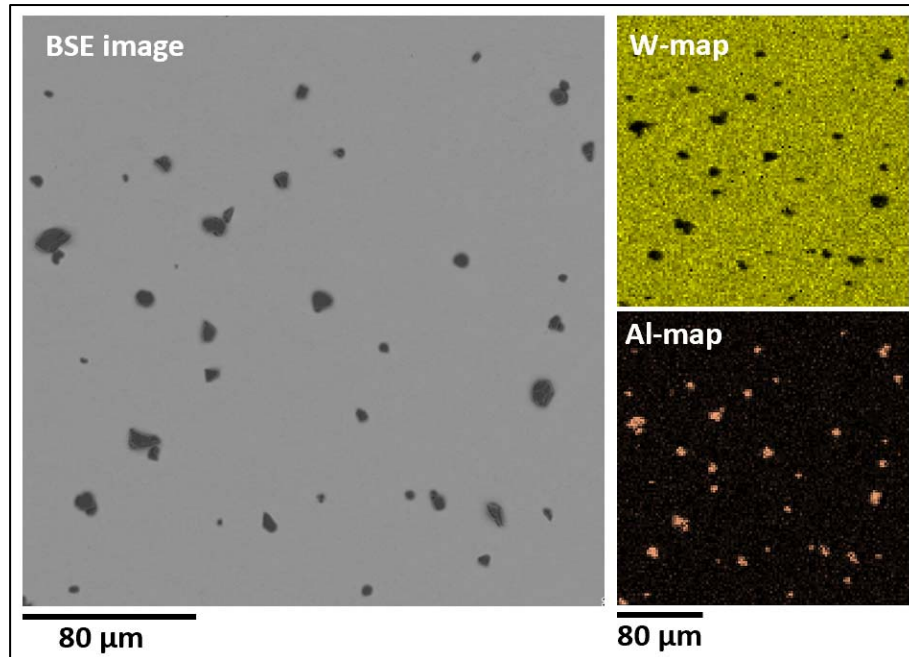


Figure 1.6. BSE image and SEM-EDX elemental maps of alumina particles on a polished W plate

The W plate with deposited alumina and the 80Ni20Cr plate were then diffusion bonded in a graphite-element furnace (Top loading graphite furnace, Oxy-Gon Industries Inc., Epsom, NH, USA) under an Ar atmosphere using a compression jig made of Molybdenum as shown in Figure 1.7. To prevent the reaction between the Mo plates and the diffusion couples, the W plates and the 80Ni20Cr plate were sandwiched between two 0.5-mm-thick alumina plates. The couple assembled in the molybdenum jig was heated at 20 °C/minute to the target temperature (1000 °C, 1100 °C, or 1200 °C). After reaching the target temperature, the diffusion couple was diffusion annealed under isothermal conditions for 2 hours. The sample was then cooled at 20 °C/minute to 400 °C, which is the temperature at which the controller of the furnace could no longer maintain the 20°C cooling rate, and the sample was then left to cool to room temperature over a period of 1 hour in the furnace. A pair of diffusion couples were prepared for use at each target temperature.

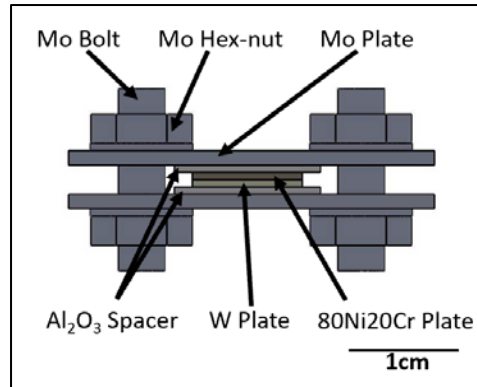


Figure 1.7. Schematic drawing of the Mo-based fixture for bonding the 80Ni20Cr/W diffusion couples

The diffusion-bonded couples (W/80Ni20Cr) were further annealed under Ar atmosphere at the bonding temperature (1000 °C, 1100 °C, or 1200 °C respectively) for an additional 48 hours, or 98 hours. In total, the annealing time for each metal couple at a given target temperature (1000 °C, 1100 °C or 1200 °C) was 50 hours or 100 hours (including the holding time of 2 hours during the bonding of the couples). At the end of the annealing treatment, a given diffusion couple was quenched by pulling it from the furnace, quickly dropping it on a Cu plate, and blowing with UHP Ar through a ¼ inch diameter tube connected to a regulator with 10 psi flow setting. The gas hose was placed about 1 inch away from the specimen on the Cu plate. Figure 1.8 shows the schematic of the quenching set up. It took about 20 seconds to pull the specimen from the hot zone of the furnace and dropping it on the Cu plate, and about another 5 seconds of continuous blowing with an Ar gas until the specimen was cool enough to touch. Hence, it took about 30 seconds in total for temperature of the specimens to drop from $\geq 1000^{\circ}\text{C}$ to $\leq 100^{\circ}\text{C}$ which corresponded to the quenching rate of $\sim 30^{\circ}\text{C/s}$.

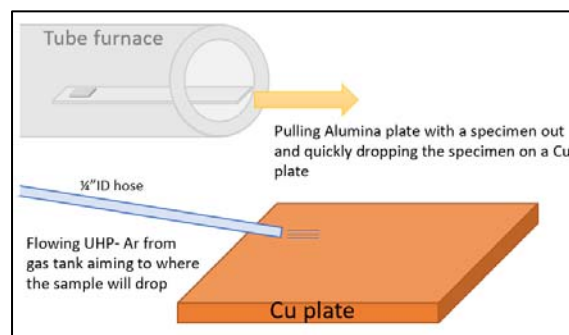


Figure 1.8. Schematic drawing of a set up for quenching diffusion couples

Each diffusion couple was then mounted in epoxy resin (EpoxyMount, Allied High Tech Products, Inc., Rancho Dominguez, CA, USA), and cross-sectioned using a low-speed diamond saw (Techcut 4TM Precision Low Speed Saw, Allied High Tech Products, Inc., Rancho Dominguez, CA, USA). The mounted cross-sectioned couples were mechanically polished up to 1 μm diamond paste finish, followed by a final polish using 0.05 μm colloidal silica. After polishing, the cross-sections were etched in a nitric acid solution (15.8 M) for 5 minutes followed by rinsing in DI water. The specimens were then lightly polished again by hand using 0.05 μm colloidal silica, followed by rinsing in DI water and drying in air for 30 minutes at room temperature.

Scanning electron microscopy with energy dispersive X ray spectroscopy (SEM-EDS) (FEI Nova Nano SEM with Oxford INCA Energy 250 EDX system) with 15 kV acceleration voltage, 0.7 nA current was used to measure chemical compositions across the diffusion zone. The spacing between each spot measurement was 1 μm for the diffusion couples annealed at 1000 $^{\circ}\text{C}$, and 3 μm for the diffusion couples annealed at 1100 $^{\circ}\text{C}$ and 1200 $^{\circ}\text{C}$. To quantify the chemical composition derived from the EDX spectra of the samples, the spectra from a known Ni-W-Cr standard (71.2 wt%Ni, 6.0 wt%Cr, 23.5 wt%W), was collected using the same measurement parameters. Aztec software was used in this process. EDX spectra were collected from the standard and then the known composition, as determined by ICP-MS (Laboratory for Environmental Analysis, Center for Applied Isotope Studies, University of Georgia, Athen, GA, USA), was introduced to the software. The software stored the input composition with respect to the collected EDX spectra of the standard. Later, the stored standardized spectra was used to quantify the EDS spectra collected from specimens. The standard used here was prepared by arc-melting Ni (Alfa Aesar, Tewksbury, MA, USA, 99.5% purity), Cr (Zr Industrial Ltd, Shanghai, China, 99.9% purity), and W (Midwest Tungsten Service, Willowbrook, IL USA, 99.95% purity). The SE image with EDX elemental maps from a cross-section of the standard is shown in Figure 1.9. Ni, Cr, and W were uniformly distributed.

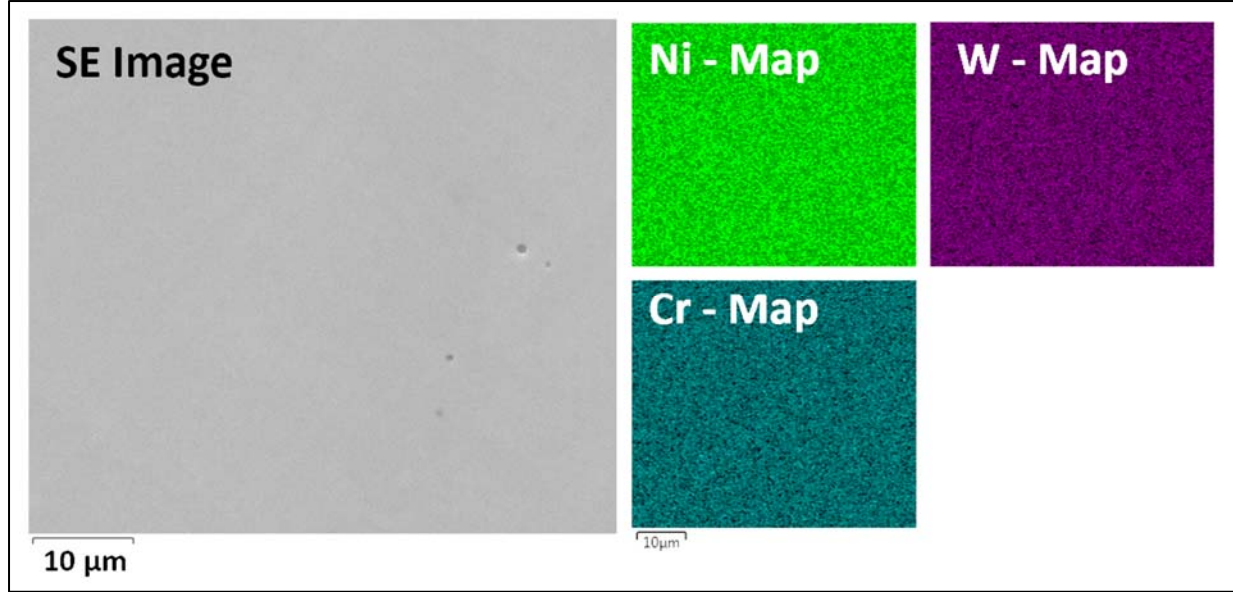


Figure 1.9. SE image and EDX elemental maps from a cross-section of a Ni-W-Cr standard

1.4 Theoretical background

Onsager's Equation (eq. 1.1) describes how the interdiffusion flux of component i in a multicomponent system depends not only on its own concentration gradient but also depends on the concentration gradient of the other components. For the system with n components, there can be $(n-1)$ independent interdiffusion fluxes [1].

$$\tilde{J}_i = - \sum_{j=1}^{n-1} \tilde{D}_{ij}^n \frac{\partial C_j}{\partial x} \quad (i = 1, 2, \dots, n-1) \quad (1.1)$$

Here \tilde{J}_i is the interdiffusion flux of component i . \tilde{D}_{ij}^n are the $(n-1)^2$ interdiffusion coefficients, C_j is the concentration of component j and x is the location of the section where the concentration gradient is determined.

In the case of a ternary system ($n=3$) Onsager's Equation becomes

$$\tilde{J}_i = -\tilde{D}_{i1}^3 \frac{\partial C_1}{\partial x} - \tilde{D}_{i2}^3 \frac{\partial C_2}{\partial x} \quad (i = 1, 2) \quad (1.2)$$

If the concentration profile is known, one can calculate the interdiffusion flux directly from the relation shown in eq. 1.4 [1], [2], [40] where x_0 is the location of the Matano plane. The Matano plane is the location where the mass loss on the left-hand side (LHS) of the Matano plane is equal

to the mass gain on the right-hand side (RHS) areas under the C_i vs. x curve [2] [1]. The location of the Matano plane can be determined from the concentration profile following eq.1.3 [1].

$$x_0 = \frac{\int_{C_i^{-\infty}}^{C_i^{+\infty}} x dC_i}{C_i^{+\infty} - C_i^{-\infty}} \quad (1.3)$$

$$\tilde{J}_i = \frac{1}{2t} \int_{c_i^- \text{ or } c_i^+}^{c_i(x)} (x - x_0) dC_i \quad (i = 1, 2, 3, \dots, n) \quad (1.4)$$

For this study, C_i is expressed in atomic fraction, t in seconds, and x in μm . Therefore, \tilde{J}_i as calculated by eq. 1.4 is expressed in unit of [atomic fraction. $\mu\text{m}/\text{s}$]. To use eq. 1.4, one can assume a constant molar volume in the diffusion zone of a couple. However, if this assumption cannot be made, an alternative expression is available for the evaluation of the interdiffusion flux as indicated in the next paragraph.

Roper and Whittle [41] proposed an equation to calculate the interdiffusion flux by taking into account of the change in molar volume as a function of composition, as shown in eq. 1.5

$$\tilde{J}_i(x) = \frac{\Delta C_i}{2t} \left[Y_i \int_{-\infty}^x \frac{(1 - Y_i)}{V_m} dx + (1 - Y_i) \int_x^{\infty} \frac{Y_i}{V_m} dx \right] \quad (i = 1, 2, \dots, n) \quad (1.5)$$

The Y_i in this equation is defined as $Y_i(x) = \frac{[C_i(x) - C_i(\infty)]}{[C_i(-\infty) - C_i(\infty)]}$, where C_i is in atomic fraction. V_m in this equation is molar volume at location x . For this study, $V_{m,x}$ for a composition at a given x was estimated by the thermodynamic definition of molar volume in terms of partial molar volumes of the individual components, $V_{m,x} = C_{Ni,x} \bar{V}_{Ni} + C_{Cr,x} \bar{V}_{Cr} + C_{W,x} \bar{V}_W$, where $\bar{V}_{Ni} = V_{m,Ni} = 6.59 \times 10^{12} \frac{\mu\text{m}^3}{\text{mol}}$, $\bar{V}_{Cr} = V_{m,Cr} = 7.23 \times 10^{12} \frac{\mu\text{m}^3}{\text{mol}}$, and $\bar{V}_W = V_{m,W} = 9.47 \times 10^{12} \frac{\mu\text{m}^3}{\text{mol}}$ [42]. Here, the assumption is made that the \bar{V}_i of each component is invariant with composition within each phase region developed in the diffusion zone and is equal to molar volumes, $V_{m,i}$, of the pure components. Note that the flux $\tilde{J}_i(x)$ from eq. 1.5 is expressed as $[\text{mol}/\mu\text{m}^2 \cdot \text{s}]$. For this study, eq. 1.5 was used to calculate \tilde{J}_i .

By integrating eq. 1.2 over a given region from x_1 to x_2 , average values for each of 4 ternary interdiffusion coefficients over the range between x_1 and x_2 can be obtained [2]:

$$\int_{x_1}^{x_2} \tilde{J}_i dx = - \int_{C_1(x_1)}^{C_1(x_2)} \tilde{D}_{i1}^3 dC_1 - \int_{C_2(x_1)}^{C_2(x_2)} \tilde{D}_{i2}^3 dC_2$$

$$= \bar{\bar{D}}_{i1}^3 [C_1(x_1) - C_1(x_2)] + \bar{\bar{D}}_{i2}^3 [C_2(x_1) - C_2(x_2)] \quad (i = 1, 2) \quad (1.6)$$

From the above equation $\bar{\bar{D}}_{ij}^3$ is an average value of the interdiffusion coefficients and is defined as [2],

$$\bar{\bar{D}}_{ij}^3 = \int_{C_j(x_1)}^{C_j(x_2)} \tilde{D}_{ij}^3 dC_j / \int_{C_j(x_1)}^{C_j(x_2)} dC_j \quad (i = 1, 2) \quad (1.7)$$

Thus, if one uses the average values of interdiffusion coefficients, $\bar{\bar{D}}_{ij}^3$, eq. 1.2 becomes.

$$\tilde{J}_i = \bar{\bar{D}}_{i1}^3 \frac{\partial C_1}{\partial x} - \bar{\bar{D}}_{i2}^3 \frac{\partial C_2}{\partial x} \quad (i = 1, 2) \quad (1.8)$$

By multiplying eq. 1.8 by $(x-x_0)^n$ and integrating over the diffusion region between x_1 and x_2 , one obtains eq 1.9 in general terms [2].

$$\int_{x_1}^{x_2} \tilde{J}_i (x - x_0)^n dx = -\bar{\bar{D}}_{i1}^3 \int_{C_1(x_1)}^{C_1(x_2)} (x - x_0)^n dC_1 - \bar{\bar{D}}_{i2}^3 \int_{C_2(x_1)}^{C_2(x_2)} (x - x_0)^n dC_2 \quad (i = 1, 2) \quad (1.9)$$

For $n=0$ eq 1.9 becomes eq 1.6, and for $n=1$ eq 1.9 becomes

$$\int_{x_1}^{x_2} \tilde{J}_i (x - x_0) dx = -\bar{\bar{D}}_{i1}^3 \int_{C_1(x_1)}^{C_1(x_2)} (x - x_0) dC_1 - \bar{\bar{D}}_{i2}^3 \int_{C_2(x_1)}^{C_2(x_2)} (x - x_0) dC_2$$

$$= 2t \left\{ \bar{\bar{D}}_{i1}^3 [\tilde{J}_1(x_1) - \tilde{J}_1(x_2)] + \bar{\bar{D}}_{i2}^3 [\tilde{J}_2(x_1) - \tilde{J}_2(x_2)] \right\} \quad (i = 1, 2) \quad (1.10)$$

By solving the 4 equations derived from eq 1.9 (for $n=0$, and $n=1$), one can obtain the value of $\bar{\bar{D}}_{11}^3$, $\bar{\bar{D}}_{12}^3$, $\bar{\bar{D}}_{21}^3$, and $\bar{\bar{D}}_{22}^3$.

From the set of average main interdiffusion coefficients, $\bar{\bar{D}}_{ii}^n$, and average cross interdiffusion coefficients, $\bar{\bar{D}}_{ij}^n$, the average effective interdiffusion coefficient can be calculated. The average effective interdiffusion coefficient is defined by eq. 1.11 [27],

$$D_{i,\Delta C}^{eff} = \bar{\bar{D}}_{ii}^n + \sum_{j \neq i}^{n-2} \bar{\bar{D}}_{ij}^n \frac{[C_j(x_1) - C_j(x_2)]}{[C_i(x_1) - C_i(x_2)]} \quad (1.11)$$

This equation shows that the average effective value includes the average main interdiffusion coefficients, \bar{D}_{ii}^n , the average cross interdiffusion coefficients, \bar{D}_{ij}^n , and the effect of the concentration difference in the region of interest (from x_1 to x_2).

In this study, the average effective interdiffusion coefficients on the LHS and on the RHS of the α/β interface, $\tilde{D}_{i,\alpha}^{eff}$, and $\tilde{D}_{i,\beta}^{eff}$ were calculated by numerically integrating the area under the curve of the $\tilde{J}_i(x)$ vs. x plots as defined by eq. 1.12 and 1.13. Equations 1.12-1.15 defined and adapted in the studies by Dayananda and coworkers [26]–[29] are considered to be applicable in this study where the diffusion zone contained two phases that were separated by a planar interface. For each diffusion couple examined in this study, the concentration profile was divided into two regions: one from $x = 0$ to $x = x_1$, and one from $x = x_1$ to $x = x_n$, where x_1 is the location of the α/β interface, and x_n is the end of the diffusion zone.

$$\tilde{D}_{i,\alpha}^{eff} = \frac{\int_0^{x_1} \tilde{J}_i dx}{C_i(0) - C_i^\alpha(x_1)} \quad (1.12)$$

$$\tilde{D}_{i,\beta}^{eff} = \frac{\int_{x_1}^{x_n} \tilde{J}_i dx}{C_i^\beta(x_1) - C_i(x_n)} \quad (1.13)$$

Together with the $\tilde{D}_{i,\alpha}^{eff}$ and $\tilde{D}_{i,\beta}^{eff}$ values, the characteristic diffusion depth parameters $d_{i,\alpha}$, and $d_{i,\beta}$ can be calculated from the $\tilde{J}_i(x)$ vs. x plots following the expression in equation 1.14 and 1.15. The characteristic diffusion depth parameter is the ratio between the mean square of the penetration depth, $\overline{(x - x_1)^2}$, and the mean penetration depth, $\overline{(x - x_1)}$, and is determined [26]–[29] for each component by.

$$d_{i,\alpha} = \frac{\int_0^{x_1} \tilde{J}_i(x) dx}{\tilde{J}_i(x_1)} \quad (1.14)$$

$$d_{i,\beta} = \frac{\int_{x_1}^{x_n} \tilde{J}_i(x) dx}{\tilde{J}_i(x_1)} \quad (1.15)$$

The average effective interdiffusion coefficients for the various components calculated over the α and β phase regions at different annealing temperatures can also be used to calculate the activation energy for diffusion, $Q_{d,i}$, by using the Arrhenius equation.

$$D = D_{0,i} \exp\left(\frac{-Q_{d,i}}{RT}\right) \quad (1.16)$$

In this case D will be $\tilde{D}_{i,\alpha}^{eff}$ or $\tilde{D}_{i,\beta}^{eff}$. $D_{0,i}$ is a pre-exponential term having the same unit as D, R is a gas constant (R=8.31 J/mol·K) and T is temperature in K. Therefore, by plotting lnD vs. (1/T), Q_d can be extracted from the slope of the linearly fitted line.

1.5 Results

1.5.1 Microstructure of diffusion couples

An example of a polished cross-section of the diffusion couple is shown in Figure 1.10. The alumina marker appears in the 80Ni20Cr side. From the Z-contrast of the BSE image, there is a clear interface between the darker area and the brighter area. The darker area is a Ni-rich (fcc) phase, which will be referred to as α -phase. The brighter area is a W-rich (bcc) phase, which will be referred to as β -phase. The SE images of the diffusion couples from all experimental conditions are provided in Appendix A2.

The diffusion path from the diffusion couple annealed at 1000°C for 100 hours plotted on the 1000°C isothermal section of the Ni-Cr-W phase diagram [33] is shown in Figure 1.11. The diffusion path (continuous red line) from the Ni-rich (α) phase ended outside the Ni-rich single phase region on the published isotherm. This observation suggests that the single phase region in the Ni corner of the isotherm could cover a larger region with greater solubility of W. The experimental diffusion path crossing the two-phase ($\alpha+\beta$) region of the isotherm, shown by dashed line is parallel to a tie-line, which is consistent with the development of a planar α/β interface. Furthermore, the solubility of Ni in the W (β phase) in the W corner of the isotherm appears to be lower than that allowed by the 1000°C isotherm.

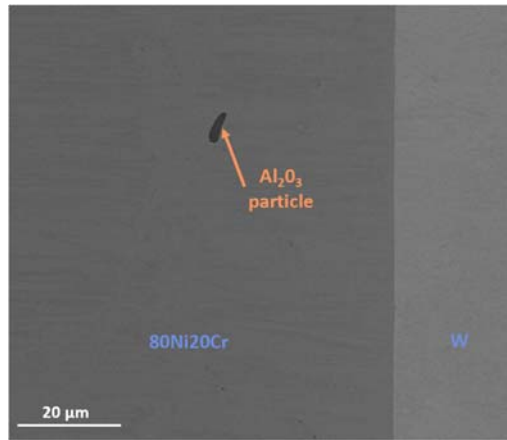


Figure 1.10. BSE image of polished cross-section from a 80Ni20Cr/W diffusion couple annealed at 1200 °C for 50 hours

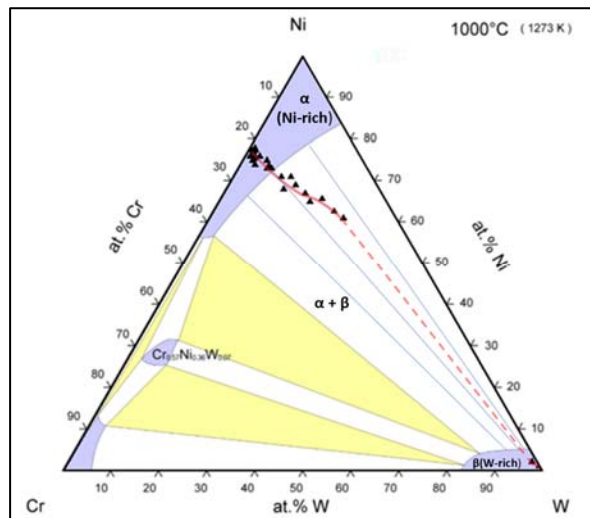


Figure 1.11. Diffusion path from the 80Ni20Cr/W couples annealed at 1000°C for 100 hours overlaying on the 1000°C isothermal cross-section of the Ni-Cr-W phase diagram [33]

Higher magnification SEM-EDX analyses were performed on polished cross-sections of the 80Ni20Cr/W diffusion couples around the interface area to determine whether intermetallic compounds had formed in the diffusion zone. Figure 1.13 a), and b) present BSE images with the corresponding elemental maps from the 80Ni20Cr/W diffusion couples annealed at 1000°C for 100 hours, and 1200°C for 100 hours. As can be seen in Figure 1.13, there was no detectable intermetallic layer near the interface. X-ray diffraction patterns were also collected from these diffusion couples and the patterns are presented in Figure 1.12. There were no detectable peaks for

intermetallic compounds which was consistent with the elemental maps from SEM-EDX analyses. Note that pure Cu tapes were attached to surfaces of the specimens during the XRD analysis as a reference for standardized peak locations.

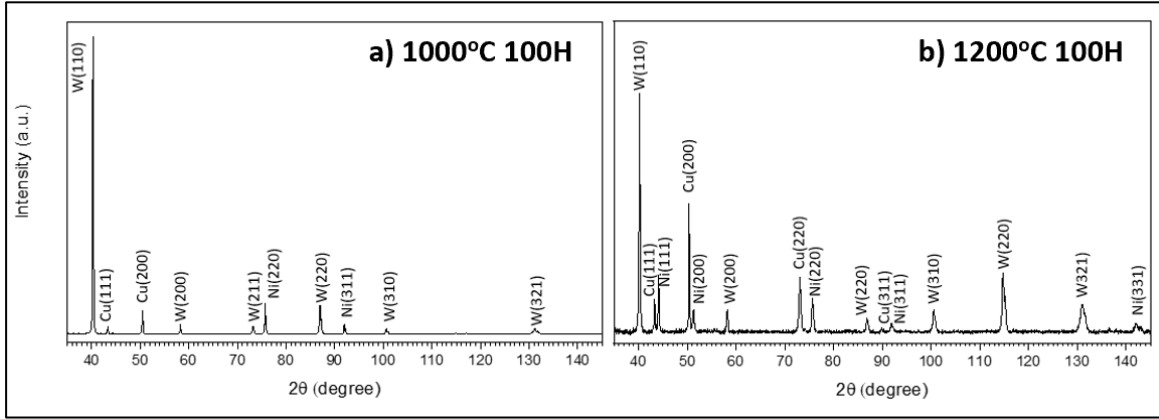


Figure 1.12. X-ray diffraction patterns from a diffusion couple annealed at a) 1000°C for 100 hours, and b) 1200°C for 100 hours

Concentration profiles of the diffusion couples annealed at 1000 °C for 50 hours, 1000 °C for 100 hours, 1100 °C for 50 hours, 1100 °C for 100 hours, 1200 °C for 50 hours, and 1200 °C for 100 hours are presented in Figure 1.14. The plots show both the experimental data (dots), and the interpolated data (line) obtained from Least Square Regression curve fitting. The vertical dash line on each profile indicates the location of the Matano plane ($x = x_0$), and the vertical solid line indicates the location of the α/β interface. Here α is a Ni-rich (fcc) phase, and β is a W-rich (bcc) phase. Since the concentrations of Ni and Cr in β -phase are very low, the concentration profiles of these two components in β -phase are not apparent in the plots. Figure 1.15, and Figure 1.16 present the magnified views of the Cr and Ni concentration profiles in the β -phase region. The concentration profile data from all diffusion couples as measured by quantitative EDX analyses are presented in Appendix A3.

The concentration profiles for all experiments share similar characteristics. All profiles exhibit a gradual change in composition on both side of the interface with discontinuity at the location of the interface. Matano planes (x_0) for all experimental conditions were on the α -phase (Ni-rich side). This observation implies that the α phase grow at the expense of the β phase and the α/β interface moved from x_0 to x_t over the diffusion period. Note that x_t is the location of the interface as determined from micrographs of the diffusion couples.

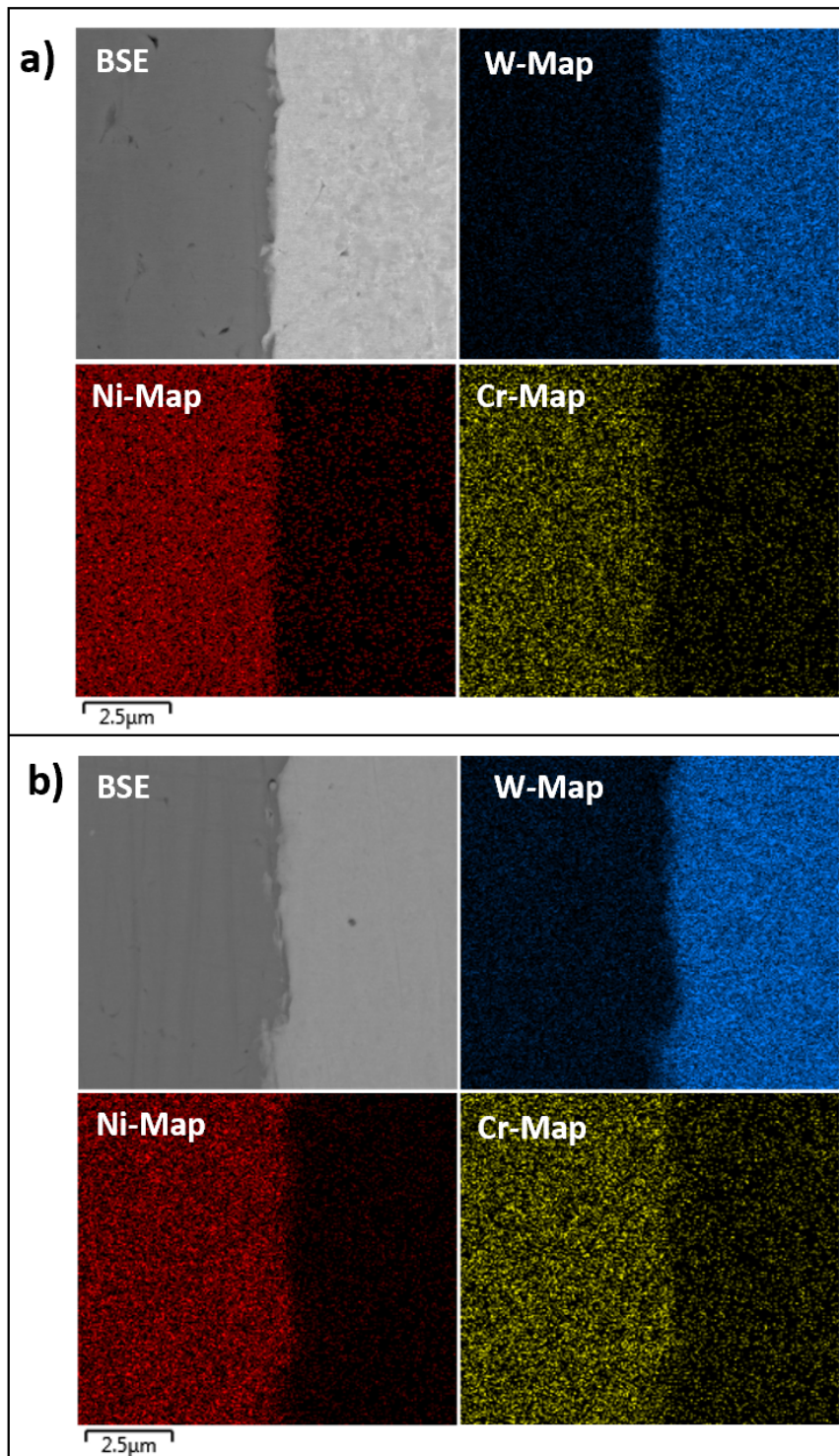


Figure 1.13. BSE images and SEM-EDX elemental maps from the polished cross-section of the 80Ni20Cr/W diffusion couples: a) annealed at 1000°C for 100 hours, and b) annealed at 1200°C for 100 hours

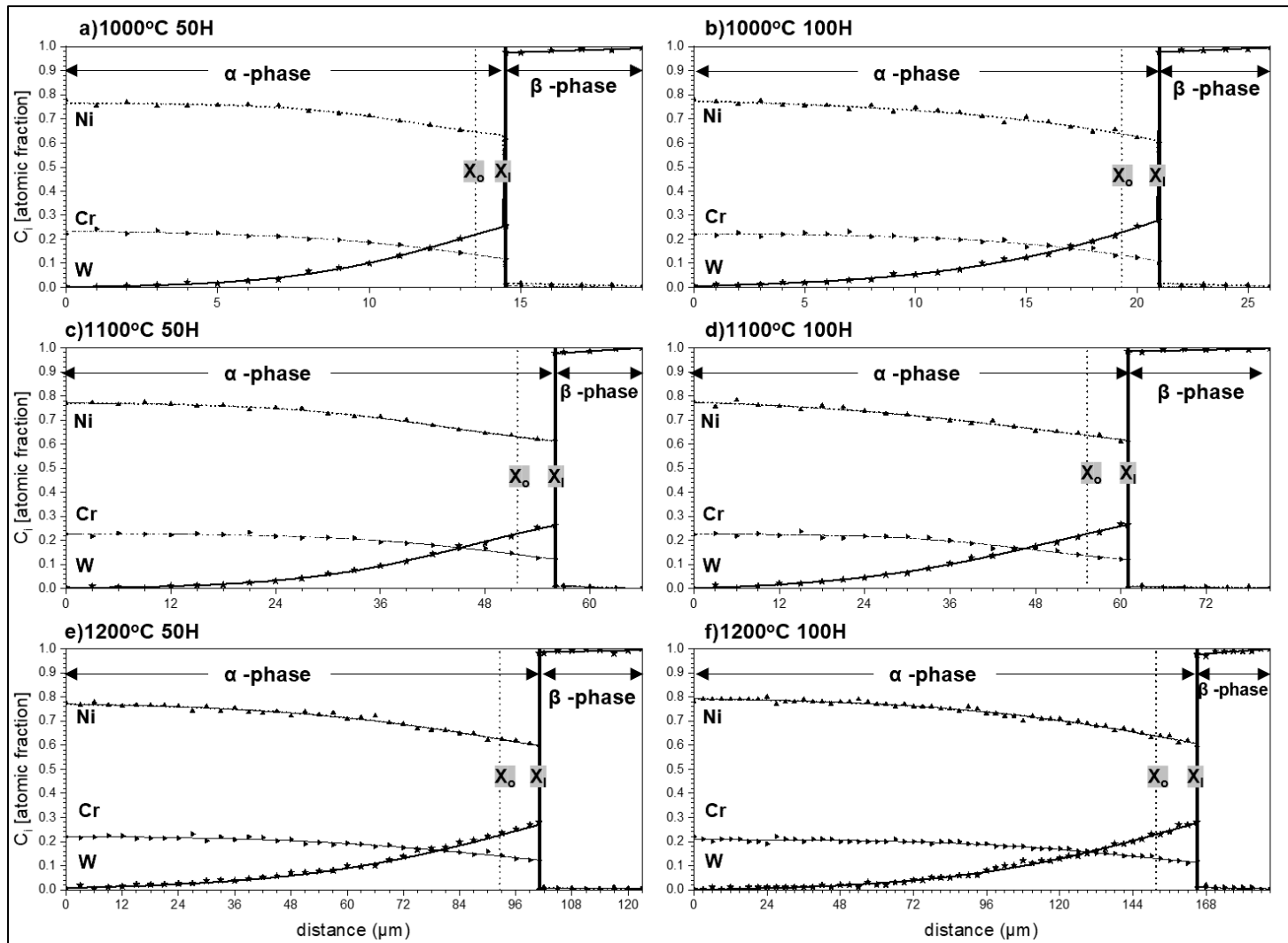


Figure 1.14. Concentration profile of 80Ni20Cr/W couple annealed at a) 1000 °C for 50 hours, b) 1000 °C for 100 hours, c) 1100 °C for 50 hours, d) 1100 °C for 100 hours, e) 1200 °C for 50 hours, and f) 1200 °C for 100 hours. The vertical dash lines represent the locations of Matano planes, and the vertical solid lines represent the locations of the α/β interface.

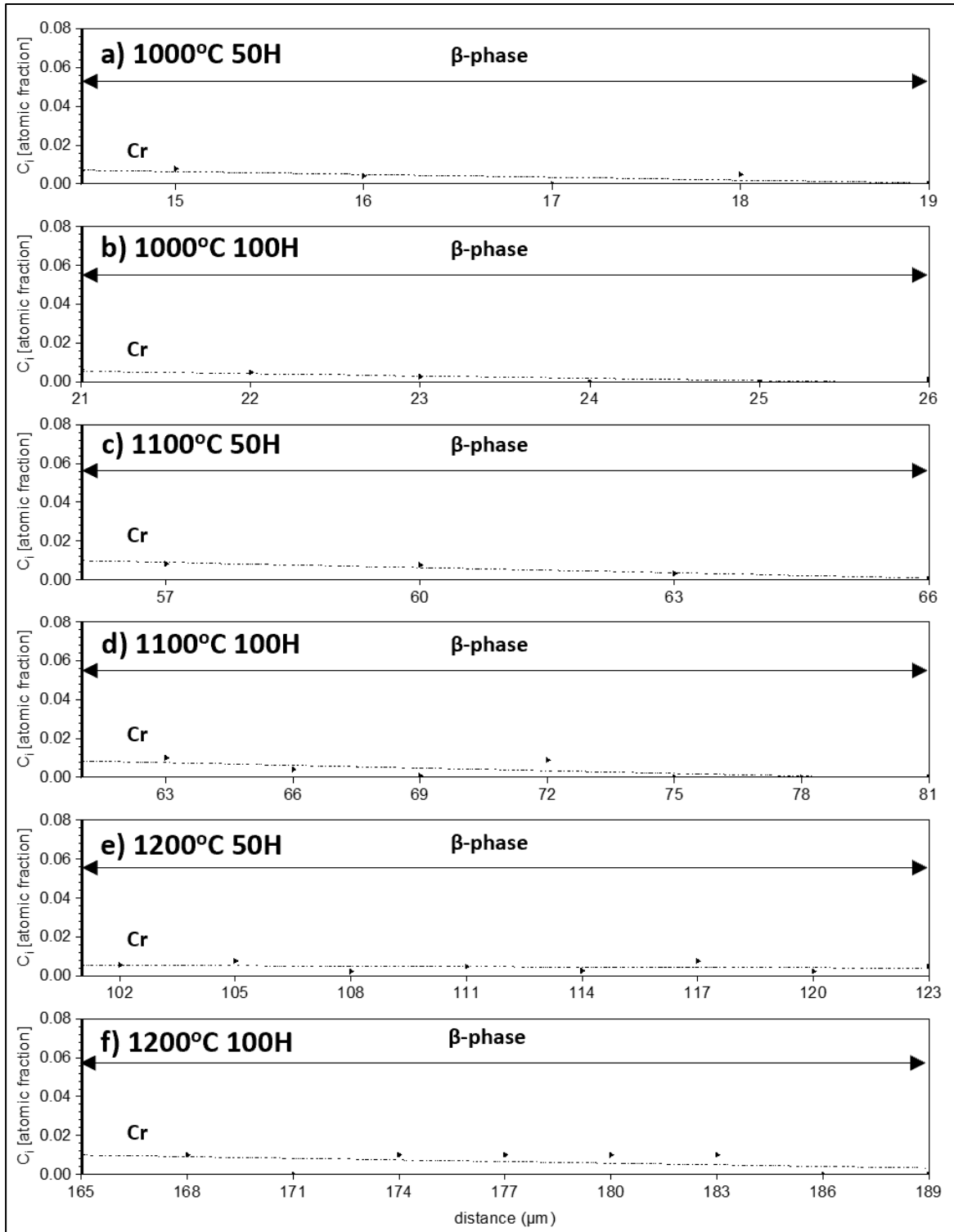


Figure 1.15. Magnified view of plots in Figure 1.14 showing Cr concentration profiles in the β -phase

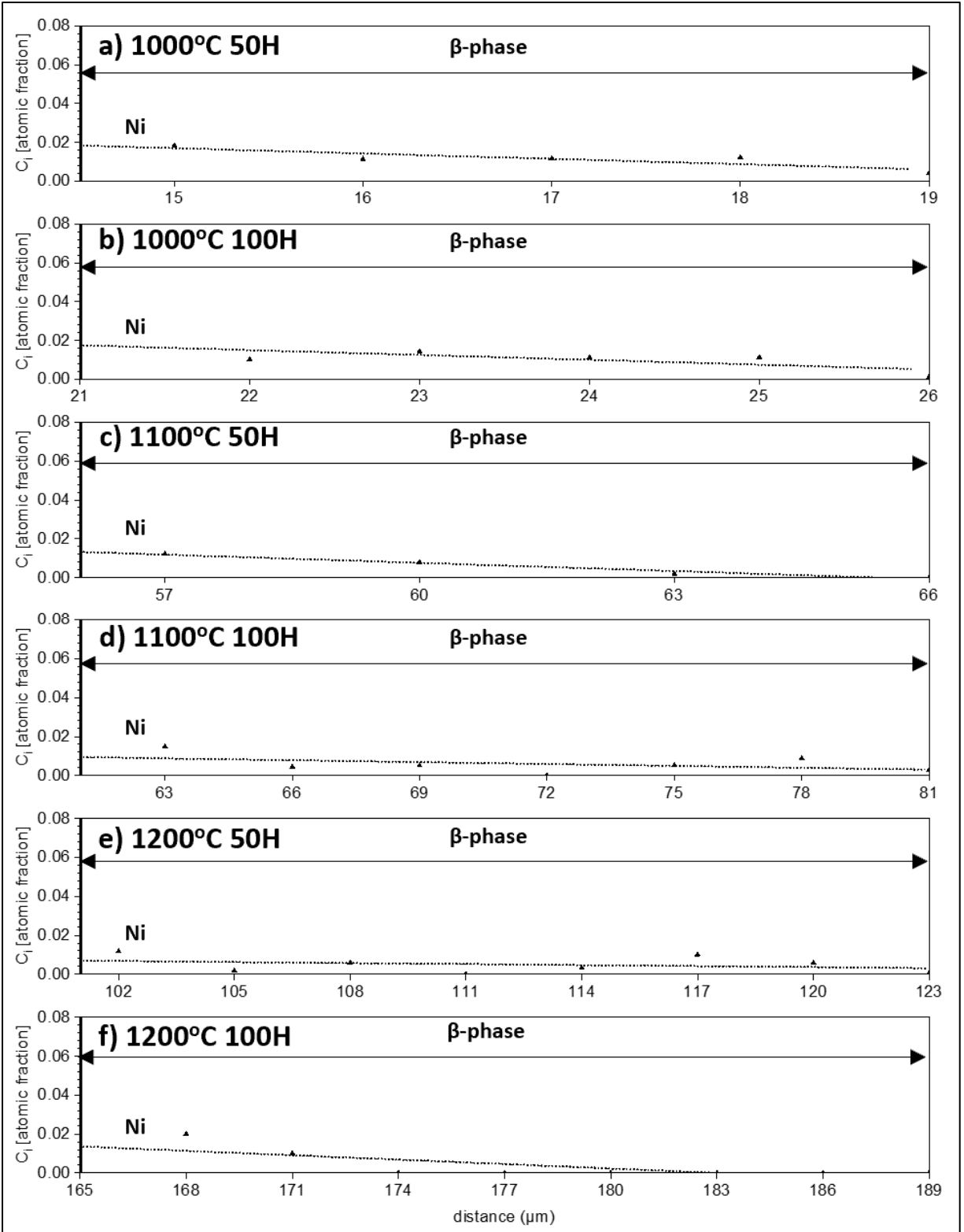


Figure 1.16. Magnified view of plots in Figure 1.14 showing Ni concentration profiles in the β -phase

1.5.2 Calculation of interdiffusion coefficients

For this study, there were three components (W, Cr, and Ni) in the system; therefore, three Matano plane locations were calculated (one for each component) on the basis of eq. 1.3. If there is negligible variation in molar volume across the diffusion zone, the Matano plane calculated from each component should be the same [1]. Locations of Matano plane calculated from concentration profiles of various couples are listed in Table 1.1

Table 1.1. Location of Matano plane as calculated from concentration profiles

Diffusion Temperature and Time	Matano Plane Location [μm]		
	$x_{o,W}$	$x_{o,Cr}$	$x_{o,Ni}$
1000 °C, 50 Hours	13	12	14
1000 °C, 100 Hours	19	18	20
1100 °C, 50 Hours	52	49	52
1100 °C, 100 Hours	55	53	56
1200 °C, 50 Hours	93	87	94
1200 °C, 100 Hours	152	144	153

As shown in Table 1.1, Matano plane locations as calculated for different components differ slightly. For all couples, the Matano plane location calculated from the concentration profiles of W, $x_{o,W}$, lies between those calculated from Ni and Cr profiles. Therefore, all analyses for interdiffusion calculations in this study were made by choosing $x_{o,W}$ as the common Matano plane. The Matano planes shown in Figure 1.14 also represent the locations of $x_{o,W}$.

The calculation of interdiffusion flux, \tilde{J}_i , using eq.1.5 bypasses the determination of x_o and was adopted in our calculations of interdiffusion fluxes. Figure 1.17 presents example plots of C_i , Y_i , and J_i (from eq.1.5) as calculated from the diffusion couple annealed at 1200°C for 100 hours.

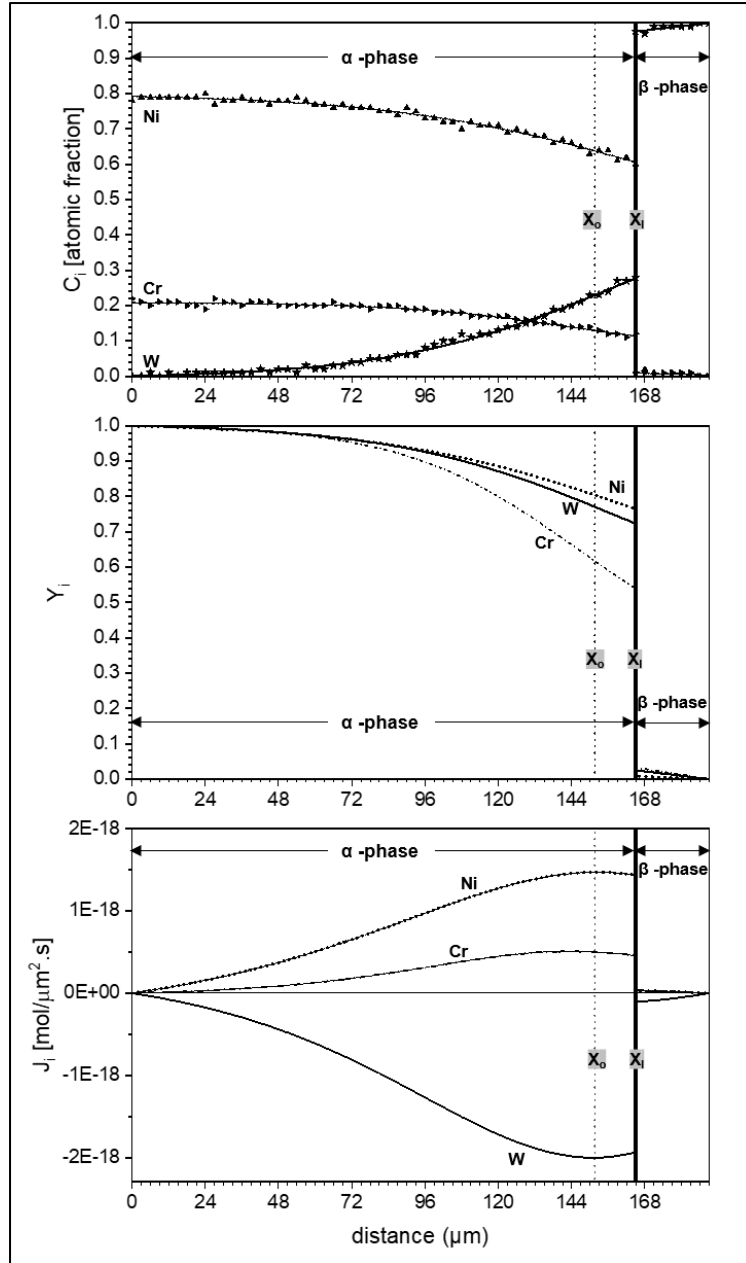


Figure 1.17. C_i , Y_i , and J_i (calculated from eq. 1.5) plots from the 80Ni20Cr/W diffusion couple annealed at 1200°C for 100 hours

To calculate the average interdiffusion coefficient, \bar{D}_{ij}^3 , each concentration profile was divided into 2 regions, one on the LHS of the α/β interface (Ni-rich phase) and one on the RHS of the α/β interface (W-rich phase). Table 1.2 shows compositions in atomic fraction at the interfaces (x_l), as determined from the concentration profiles extrapolated to the locations of the interfaces.

Table 1.2. Composition at the α/β interface (x_I)

Experimental condition	Location of interface [μm]	Composition at α/β interface [atomic fraction]					
		(C _{W,a}) _I	(C _{Cr,a}) _I	(C _{Ni,a}) _I	(C _{W,β)_I}	(C _{Cr,β)_I}	(C _{Ni,β)_I}
1000°C 50 Hour	15	0.26	0.12	0.62	0.97	0.01	0.02
1000°C 100 Hour	21	0.28	0.11	0.61	0.97	0.01	0.02
1100°C 50 Hour	56	0.26	0.12	0.62	0.98	0.01	0.01
1100°C 100 Hour	61	0.26	0.12	0.62	0.98	0.01	0.01
1200°C 50 Hour	101	0.28	0.12	0.60	0.98	0.01	0.01
1200°C 100 Hour	165	0.28	0.12	0.60	0.98	0.01	0.01

As can be seen in Table 1.2, the compositions at the interface for both α -phase or β -phase are similar for all diffusion couples. Therefore, a reasonable comparison between the calculated average effective interdiffusion coefficients determined from the various couples diffusion annealed at different conditions can be made.

The average effective interdiffusion coefficient, $\tilde{D}_{i,\Delta C}^{eff}$ together with the corresponding characteristic interdiffusion depth, $d_{i,\Delta C}$ were calculated from the interpolated flux profiles obtained from eq. 1.5. The calculated values are listed in Table 1.3. These values can be used to predict the diffusion profile at any given annealing time following eq. 1.17 and 1.18. These equations correspond to the boundary conditions of a solid-solid infinite diffusion couple and were derived similar to the procedures employed for vapor-solid couples by Hurley and Dayananda [43] To use these equations, the concentration of element i , C_i , was expressed as a function of the Boltzmann parameter λ , where $\lambda(x) = \frac{(x-x_o)}{\sqrt{t}}$.

For the region in the α -phase ($-\infty < \lambda < \lambda_I$)

$$C_{i,\alpha}(\lambda) = \left[\frac{\operatorname{erf}\left(\frac{\lambda}{2\sqrt{\tilde{D}_{i,\alpha}^{eff}}}\right) + 1}{\operatorname{erf}\left(\frac{\lambda_I}{2\sqrt{\tilde{D}_{i,\alpha}^{eff}}}\right) + 1} \right] (C_{i,I,\alpha} - C_{i,int,\alpha}) + C_{i,int,\alpha} \quad (1.17)$$

For the region in the β -phase ($\lambda_I < \lambda < \infty$)

$$C_{i,\beta}(\lambda) = \left[\frac{\operatorname{erf}\left(\frac{\lambda}{2\sqrt{\tilde{D}_{i,\beta}^{eff}}}\right) - \operatorname{erf}\left(\frac{\lambda_I}{2\sqrt{\tilde{D}_{i,\beta}^{eff}}}\right)}{1 - \operatorname{erf}\left(\frac{\lambda_I}{2\sqrt{\tilde{D}_{i,\beta}^{eff}}}\right)} \right] (C_{i,int,\beta} - C_{i,I,\beta}) + C_{i,I,\beta} \quad (1.18)$$

All the C_i values in eq. 1.17 and 1.18 have unit in [atomic fraction]. $C_{i,\alpha}(\lambda)$, or $C_{i,\beta}(\lambda)$ represents concentration of element i at a given λ position. $C_{i,int,\alpha}$, or $C_{i,int,\beta}$ is initial concentration of element i in the α , or β terminal alloy. $C_{i,I,\alpha}$, or $C_{i,I,\beta}$ is concentration of element i in α -phase or β -phase at the interface.

Figure 1.18 shows that the calculated profiles (lines) for all the diffusion couples fit well with the experimental profiles (dots).

Table 1.3. Average effective interdiffusion coefficients and characteristic interdiffusion depths for the regions on the α -phase (Ni-rich) and the β -phase (W-rich)

Experimental condition		Average effective interdiffusion coefficient [$\mu\text{m}^2/\text{s}$]			$d_{i,\alpha}$ or $d_{i,\beta}$ [μm] for		
		\tilde{D}_W^{eff}	\tilde{D}_{Cr}^{eff}	\tilde{D}_{Ni}^{eff}	W	Cr	Ni
1000 °C, 50 Hours	α -phase	6.7E-05	5.0E-05	4.1E-05	7.3	9.3	6.5
	β -phase	3.8E-05	3.6E-05	2.5E-05	2.7	2.6	2.8
1000 °C, 100 Hours	α -phase	7.8E-05	4.3E-05	6.7E-05	11.8	13.0	12.4
	β -phase	2.7E-05	2.4E-05	1.8E-05	2.9	2.8	3.0
1100 °C, 50 Hours	α -phase	1.0E-03	5.8E-04	8.2E-04	28.1	30.8	28.6
	β -phase	2.4E-04	2.1E-04	1.6E-04	5.8	5.6	5.8
1100 °C, 100 Hours	α -phase	8.3E-04	4.0E-04	7.0E-04	35.6	33.3	37.7
	β -phase	3.1E-04	3.4E-04	2.8E-04	11.9	11.6	12.0
1200 °C, 50 Hours	α -phase	3.8E-03	2.6E-03	2.9E-03	56.1	63.3	56.2
	β -phase	1.7E-03	1.0E-03	7.5E-04	12.8	12.4	12.9
1200 °C, 100 Hours	α -phase	4.6E-03	2.7E-03	3.6E-03	88.6	91.6	90.7
	β -phase	7.9E-04	7.2E-04	5.3E-04	13.6	13.2	13.7

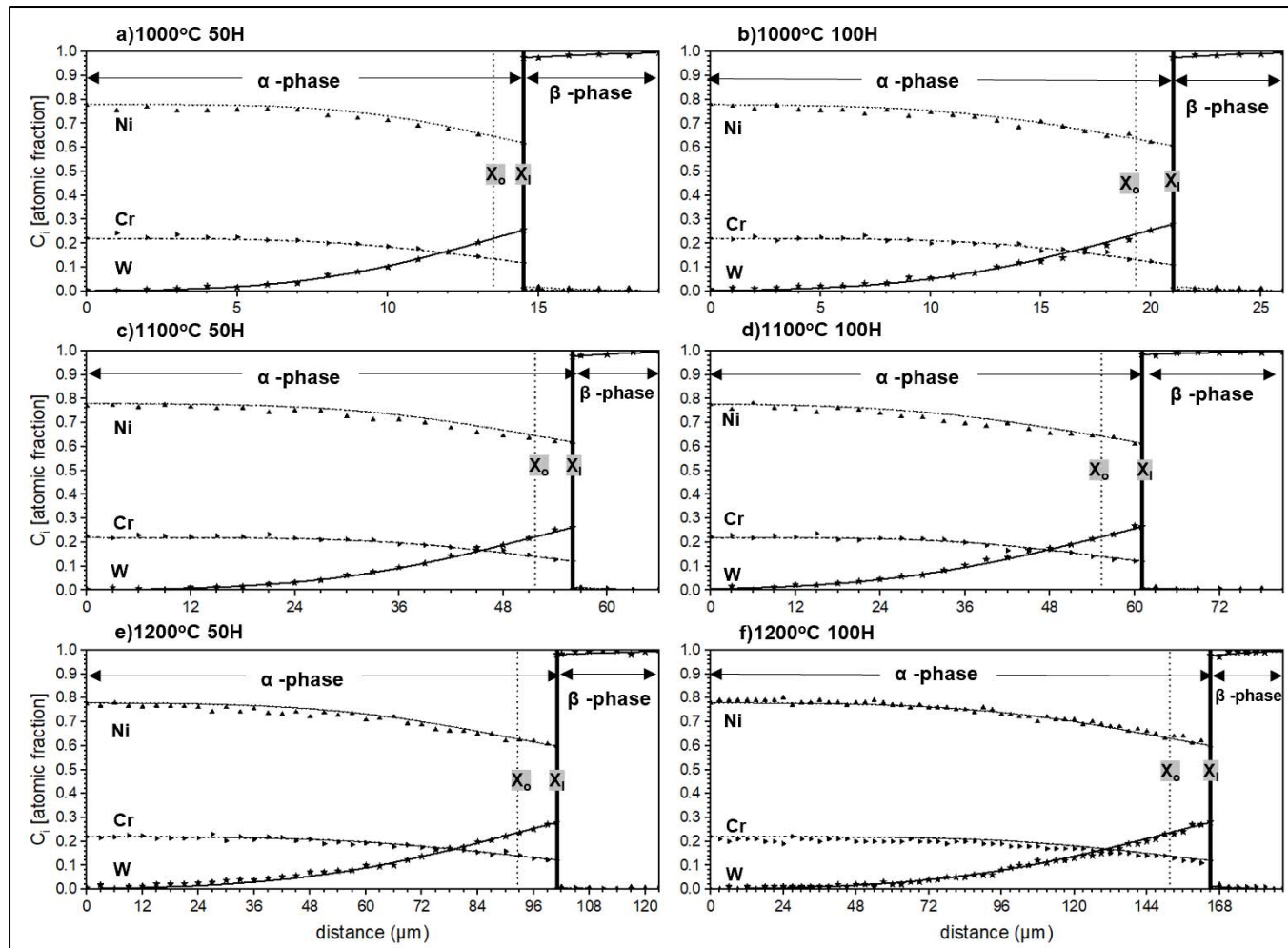


Figure 1.18. Diffusion profiles from all diffusion couples as calculated by eq. 1.17 and 1.18 (lines) comparing with the experimental data (dots): a) 1000 °C for 50 hours, b) 1000 °C for 100 hours, c) 1100 °C for 50 hours, d) 1100 °C for 100 hours, e) 1200 °C for 50 hours, and f) 1200 °C for 100 hours. The vertical dash lines represent the locations of Matano planes, and the vertical solid line represent the locations of the α/β interface.

1.5.3 Activation Energy for diffusion

The activation energy for diffusion, Q_d , was calculated from the $\tilde{D}_{i,\Delta C}^{eff}$ from each side of α/β interface. To be able to compare the average effective interdiffusion coefficients across different annealing temperatures, the diffusion profile was divided into 2 regions (α -phase and β -phase), and $\tilde{D}_{i,\Delta C}^{eff}$ values for each region were calculated. The $\ln(\tilde{D}_{i,\Delta C}^{eff})$ for W, Cr, and Ni determined from the 2 regions were plotted as a function of $1/T$ as shown in Figure 1.19. Error bars on the plots are the standard deviation of $\tilde{D}_{i,\Delta C}^{eff}$ values from the diffusion couples annealed at different times. The Q_d values that were extracted from the linear fitted line are listed in Table 1.4. The reported error values in Table 1.4 are standard errors of slope values from the least squares regression fitted lines in Figure 1.19 multiplied by $8.31 \times 10^{-3} \text{ J/mol.K (R/1000)}$

Table 1.4. Activation energies determined from average effective interdiffusion coefficients

Region	Activation Energy [kJ/mol]		
	$Q_{d,W}$	$Q_{d,Cr}$	$Q_{d,Ni}$
α -phase	318 \pm 33	315 \pm 17	321 \pm 40
β -phase	283 \pm 17	264 \pm 37	266 \pm 45

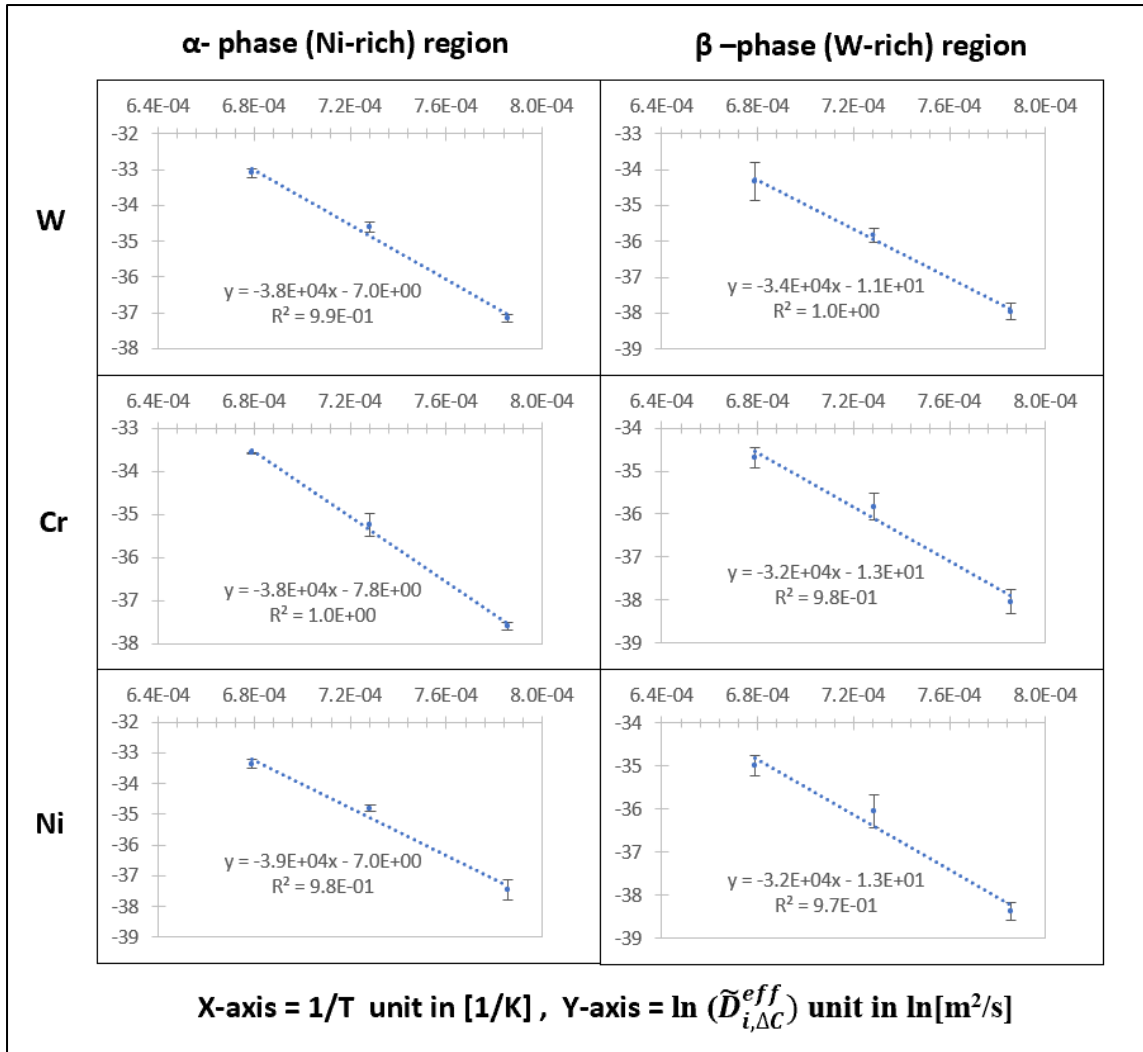


Figure 1.19. Arrhenius plot of $\ln(\tilde{D}_{i,\Delta C}^{eff})$ as a function of $1/T$

1.6 Discussion

For all experimental conditions in this study, no intermetallic compound formation was detected within the diffusion zone. Unlike what was reported in the study by Karpinos, et al. [30], only Ni-rich, and W-rich solid solution phases were found in this work, which was consistent with the Cr-W-Ni ternary phase diagram at temperatures between 1000-1200°C [10]. The major factor that can lead to the formation of the intermetallic phase is slower quenching rates during cooling in the furnace. In this study, the diffusion couples were pulled from the furnace and immediately quenched by a stream of Ar gas passed over them on a Cu slab. Since the diffusion couples in this study were relatively small (10 mm x 12 mm x 2 mm), the air quenching was relatively fast.

Kapinos, et al.[30] reported that they quenched their specimens of W-fibers in Ni-Cr matrix at 10°C/minute and 40°C/minute. Therefore, the quenching rate in this study was significantly faster. For this study, the quenched diffusion couple was cooled to touch just after a few seconds of Ar gas blowing. According to the isothermal section of phase diagram of Ni-Cr-W at 1000 °C, and 1200 °C [10] , an intermetallic phase is not expected to develop in the diffusion zones for the couples investigated in this study. But, an interface, planar or nonplanar, is expected to form between the Ni-rich (α) and W-rich (β) ternary phases.

From Figure 1.14, the location of the α/β interface, x_I , is on the RHS of the location of the Matano plane, x_o , for all couples. Consider eq. 1.19, which is an equation for the velocity of motion of the α/β interface, ϕ_I [44], [45].

$$\phi_I = \frac{(x_I - x_o)}{2t} = \frac{(\tilde{J}_i^\beta)_I - (\tilde{J}_i^\alpha)_I}{(C_i^\beta)_I - (C_i^\alpha)_I} \quad (i = \text{element in the system}) \quad (1.19)$$

Knowing that $x_I > x_o$ for all experimental couples in Figure 1.14, ϕ_I for this study is positive. Consider the case where $i=W$, from the concentration profile plot as shown in Figure 1.14, $(C_W^\beta)_I > (C_W^\alpha)_I$. Hence, the denominator term in eq. 1.19 is positive. Therefore, the numerator term, $(\tilde{J}_W^\beta)_I - (\tilde{J}_W^\alpha)_I$, also has to be positive. From the flux plot as shown in Figure 1.17, $(\tilde{J}_W^\beta)_I$, and $(\tilde{J}_W^\alpha)_I$ are both negative. To satisfy eq. 1.19, magnitude of $(\tilde{J}_W^\alpha)_I$ needs to be higher than the magnitude of $(\tilde{J}_W^\beta)_I$ which is consistent with the plot of \tilde{J}_W as a function of x , shown in Figure 1.17. This means that interdiffusion flux of W moving into the α -phase (from RHS to LHS) from the interface has to be larger in magnitude than what arrives to the interface from the β -side.

This same logic can be applied for the case of Ni and Cr. $(C_{Ni\ or\ Cr}^\beta)_I < (C_{Ni\ or\ Cr}^\alpha)_I$. Hence the denominator term is negative. Therefore, the numerator term, $(\tilde{J}_{Ni\ or\ Cr}^\beta)_I - (\tilde{J}_{Ni\ or\ Cr}^\alpha)_I$, also needs to be negative. From the flux plot as shown in Figure 1.17, $(\tilde{J}_{Ni\ or\ Cr}^\beta)_I$, and $(\tilde{J}_{Ni\ or\ Cr}^\alpha)_I$ are both positive. To satisfy eq. 1.19, magnitude of $(\tilde{J}_{Ni\ or\ Cr}^\alpha)_I$ needs to be higher than the magnitude of $(\tilde{J}_{Ni\ or\ Cr}^\beta)_I$ which is consistent with the plot of $\tilde{J}_{Ni\ or\ Cr}$ as shown in Figure 1.17. This means

the positive interdiffusion flux of Ni or Cr at the interface on the α side of the interface is larger in magnitude than what leaves the interface toward the β -side.

Motion of marker plane can also be described by Darken's expression [46] (eq. 1.20). This equation expresses the relationship between the marker motion and the sum of intrinsic flux, J_i .

$$(x_m - x_o) = \frac{-\sum_{i=1}^n J_i dt}{\rho} \text{ for ternary system } n = 3 \quad (1.20)$$

In this equation J_i , represents intrinsic flux of component I, and ρ is molar density. The alumina marker as shown in Figure 1.10 is to the left of x_o on the α -phase side. Hence, $(x_m - x_o)$ is a negative value. This observation implies that the sum of the positive intrinsic fluxes of Ni and Cr (from left to right) has to be larger than the intrinsic flux of W in the opposite direction within the α phase.

As shown in Table 1.3, the average effective interdiffusion coefficients obtained from the β -phase are smaller than the those obtained from the α -phase for all elements. This suggests that the interdiffusion of each individual component on the Ni-rich side occurs faster than the corresponding interdiffusion of the component on the W- rich side. However, the activation energy for diffusion on the Ni-rich side was slightly larger than on the W- rich side which indicated that the pre-exponential terms should be higher on the Ni-rich side.

For the binary Ni-W system , the calculated tracer diffusion coefficient of W in Ni using the reported values of preexponential terms , $D_{w,0} = 1.9 \times 10^{-4} \text{ m}^2/\text{s}$ and activation energy, $Q_{d,w} = 299 \text{ kJ/mol}$ [47] were $1.0 \times 10^{-16} \text{ m}^2/\text{s}$, $8.0 \times 10^{-16} \text{ m}^2/\text{s}$, and $4.5 \times 10^{-15} \text{ m}^2/\text{s}$ at $1000 \text{ }^\circ\text{C}$, $1100 \text{ }^\circ\text{C}$, and $1200 \text{ }^\circ\text{C}$ respectively. The reported activation energy, $Q_{d,w}$, was similar to the values that were obtained from this study ($318 \pm 33 \text{ kJ/mol}$). The calculated tracer diffusion coefficients for Ni-Cr binary system is of the same order of magnitude as the average effective interdiffusion coefficient of W, $\tilde{D}_{W,\Delta C}^{eff}$ determined in this study. However, the tracer diffusion coefficient is different from the interdiffusion coefficient. For a more direct comparison, Chen, et al. [48] reported an interdiffusion coefficient of W in a Ni-W alloy with 6 wt% W of $3.2 \times 10^{-15} \text{ m}^2/\text{s}$ at $1200 \text{ }^\circ\text{C}$. From our study, the $\tilde{D}_{W,\alpha}^{eff}$ at $1200 \text{ }^\circ\text{C}$ in the Ni-rich region was $4.2 \times 10^{-15} \text{ m}^2/\text{s}$. The value from their study was slightly smaller but of the same order of magnitude as the $\tilde{D}_{W,\alpha}^{eff}$ obtained in this study. Chen, et al.[48] also reported the activation energy of W in the Ni-W system, $Q_{d,w}$, to be 261.4 kJ/mol . This value was slightly lower than our value of $318 \pm 33 \text{ kJ/mol}$.

1.7 Conclusion

This study was an initial investigation of the diffusion behavior between 80Ni20Cr alloys and commercial grade W at selected temperatures over the range from 1000 – 1200 °C. Diffusion couples annealed at the various temperatures were analyzed employing the methods developed by Dayananda and coworkers [26]–[29], for the determination of average effective interdiffusion coefficients and characteristic interdiffusion depths for W, Cr, and Ni in both α and β regions developed in the diffusion zone. The main conclusions from this study are as follows.

- By limiting the size of the diffusion couples and avoiding the use of bulky fixturing during the annealing process, the quenching rate was sufficiently high as to prevent the formation of intermetallic phases by air quenching.
- From the cross-section of the annealed couples, the marker particles appeared on the α -phase (Ni-rich), which suggested that as the α -phase grows into the β -phase (W-rich) at the expense of the β -phase, the sum of intrinsic fluxes of Ni and Cr is larger in magnitude than that of W intrinsic flux in the opposite direction.
- The average effective interdiffusion coefficients were used to predict the experimental concentration profiles. The calculated profiles exhibited a good match with the corresponding measured profiles at the same annealing conditions.
- The average effective interdiffusion coefficients determined at different annealing temperatures were used to calculate the activation energies for diffusion of each element in the α and β regions on the LHS, and the RHS of the α/β interface. These calculated values were consistent with the values reported in other studies. The activation energy values for W, Cr, and Ni in each of the phases were found to be similar but greater for the α phase than for the β phase.

2. EFFECT OF GRAIN SIZE OF TUNGSTEN ON THE INTERDIFFUSION OF NICKEL CHROMIUM ALLOY/ TUNGSTEN DIFFUSION COUPLES

2.1 Abstract

Diffusion couples between 80Ni20Cr alloys and W plates with two different grain sizes were used to study the effect of W grain size on the diffusion of Ni and Cr. The large grain tungsten (LGW) in this study possessed an average grain size of $29.3 \pm 3.2 \mu\text{m}$, while the fine grain tungsten (FGW) possessed an average size of only $2.3 \pm 0.1 \mu\text{m}$. At 1000°C , there was no appreciable difference in the overall concentration profiles as measured by SEM-EDX analyses of the FGW/80Ni20Cr couples and LGW/80Ni20Cr couples. Even though the STEM-EDX results suggested that Ni and Cr exhibited slight preference to diffuse through the grain boundaries of W for the studied temperature range, the temperatures were sufficiently high that the volume diffusion rates of Ni and Cr were appreciable relative to the diffusion of Ni and Cr along the grain boundaries of W. Therefore, at grain boundaries of W grains adjacent to the 80Ni20Cr/FGW interface, only small composition deviations were observed, while the overall concentration profiles were similar to those for LGW diffusion couples.

2.2 Introduction

From a diffusion study in the Ni-Cr-W system at 1000°C - 1200°C using 80Ni20Cr/LGW diffusion couples, it was known that the interface between the α -phase (Ni-rich) and β -phase (W-rich) moved toward W which suggested that α -phase grows into the β -phase at the expense of the β -phase. Recently, several studies have reported methods for producing tungsten with a fine grain size, so as to yield improved mechanical properties at high temperatures for applications such as radiator shields, rocket engine nozzles, and plasma penetrators [49]–[51]. Knowing that applications of W at high temperature tend to shift toward utilizing of finer grain tungsten material, a better understanding of roles of W grain boundaries on solid state diffusion of other elements in contact with parts made of fine grain tungsten would be useful.

Inomata and Kajihara [31] studied solid-state diffusion in the binary Ni-W system in the temperature range of $750 - 900^\circ\text{C}$. They reported the formation of Ni_4W growing toward Ni. The

formation of the Ni₄W layer was governed by a combination of grain boundary diffusion and volume diffusion, while a reduced contribution of grain boundary diffusion was observed at 900 °C.

The purpose of this study is to investigate the influence of W grain boundaries toward interdiffusion behavior of Ni, Cr, and W. The investigation was focusing on the case where intermetallic compounds were not presented. The study was conducted at 1000 °C using a single diffusion couple comprised of a fine-grained tungsten and a Ni-20wt%Cr alloy (80Ni20Cr). Average effective interdiffusion coefficients of Ni, Cr, and W in fine grain tungsten were calculated by an analysis method developed by Dayananda and coworkers [26]–[29].

Understanding the interaction between the Ni-Cr alloys, and W can also support the fundamental knowledge behind the production of ultrafine grained tungsten heavy alloys (WHAs), which is under development in China via plasma sintering at 1050 °C recently [49]. Ni and Cr are among several elements that were used to promote densification in the production of fine grained tungsten [49], [52].

2.3 Experimental procedure

2.3.1 Production of fine grain tungsten plate

Tungsten with a small grain size is referred to herein as FGW (fine grain tungsten), and commercially-available, coarse-grain tungsten is referred to herein as LGW (large grain tungsten). The LGW was obtained from a 1-mm-thick tungsten sheet (Midwest Tungsten Service, Willowbrook, IL USA, 99.95% purity, 0.002%Fe, 0.001%Al, 0.001%Ni, 0.001%Si, 0.001%C, 0.002%Ni₂, 0.005%O₂). To produce FGW from the as-received “80-nm” W powders (Hongwu commercial, Guangdong, China, 99.9% purity, Mo ≤ 28ppm, K ≤ 60 ppm, Fe ≤ 18 ppm, Al ≤ 11 ppm, Mg, Ni, Ca, Si, As, Na, Mn, Pb ≤ 10 ppm), two approaches were examined; pressureless sintering and hot pressing. The as-received powder was stored in a nitrogen atmosphere to inhibit oxidation.

i) Compaction and pressureless sintering

As-received W powders were formed into green a body using a uniaxial compaction process. A 1.3-cm-diameter low carbon steel cylindrical die was used to form a FGW green body. After

filling the die with 3 grams of the W powder, a peak pressure of 500 MPa was applied to the die uniaxially at room temperature. The uniaxial loading was held for 5 minutes. The compacted FGW green body was then carefully removed from the die, weighed, and the diameter and thickness were measured.

Sintering process was adapted from the method developed by Ren, et al.[51], [53]. The green body was sintered in a tube furnace with flowing 4% H₂- Ar gas (4% Hydrogen balance Argon Certified Standard Mixture, Airgas, USA). The temperature profile are shown in Figure 2.1. For the first step, the specimen was held at 750°C for 3 hours in a 4% H₂-Ar atmosphere (Airgas) to reduce thin tungsten oxide layers formed during the processing of nano-W powder. The specimen was then heated to 1050 °C and held for 2 hours, followed by heating to 1250 °C and holding for another 50 hours. The heating and cooling rates were 3 °C/minute. The specimen was placed on an alumina plate during sintering, and no reaction between the specimen and the alumina plate was observed. The FGW disk produced via this method will be referred to as FGW_CS1250C.

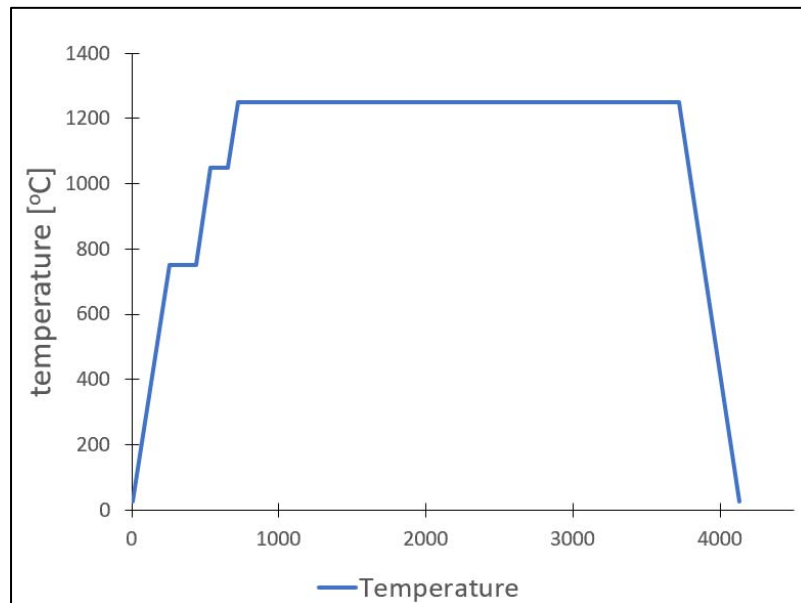


Figure 2.1. Temperature and profiles for producing FGW specimen via a pre-compaction and pressureless sintering method.

After sintering, the specimen density was determined by measuring the bulk dimension and weight. The sintered specimen was sectioned by a low-speed diamond saw (Techcut 4TM Precision

Low Speed Saw, Allied High Tech Products, Inc., Rancho Dominguez, CA, USA) and the SEM (FEI Nova Nano SEM) was used for observing the microstructure of the sintered W plate.

ii) Hot pressing

The as-received W powder was hot pressed in a 1.3-cm cylindrical graphite die (AR-14, Ohio Carbon Blank, Willoughby, OH, USA). Before an experiment, the cylindrical die parts were coated with Boron Nitride Aerosol Lubriccoat (ZYP Coatings, Inc., Oak Ridge, TN, USA). Organic binders in the spray were removed by heating the coated parts on a hot plate for 30 minutes at 200 °C in air.

The die was filled with 3 grams of the W powder. The assembly was loaded into a hot press (front loading graphite furnace, Oxy-Gon Industries Inc., Epsom, NH, USA), and then a uniaxial pressure of 80 MPa was applied to the die at room temperature. The chamber was evacuated and purged with a 4% H₂-Ar gas (Airgas) three times and lastly the chamber was maintained in a 4% H₂-Ar atmosphere. The temperature and pressure profiles throughout the experiment are shown in Figure 2.2. After preparing the atmosphere, the chamber was heated to 750 °C and held for 3 hours to reduce the thin tungsten oxide layer formed during the processing of nano W powder. The assembly was then heated to 1050 °C and held for 2 hours followed by heating to 1250 °C and holding for another 3 hours. The heating and cooling rates were kept at 10 °C/minute, and the 80 MPa compression was maintained throughout the experiment. Another attempt was also made with the same peak pressure but with a peak temperature of 1500 °C for 1.5 hours. The FGW disk produced via the described hot pressing method are referred to as FGW_HP1250C, and FGW_HP1500C.

After hot pressing, the specimen densities were determined by measuring the bulk dimensions and weights. The hotpressed specimens were sectioned by a low-speed diamond saw (Techcut 4TM Precision Low Speed Saw, Allied High Tech Products, Inc., Rancho Dominguez, CA, USA) and the SEM (FEI Nova Nano SEM) and EBSD were used for observing the microstructure of the hot pressed W plate.

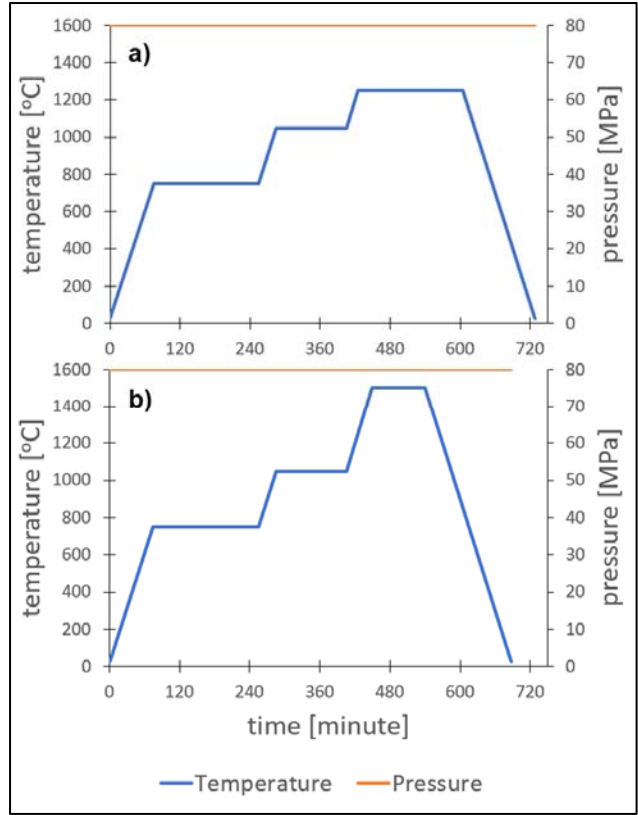


Figure 2.2. Temperature and pressure profiles for producing FGW discs via the hot pressing using two different conditions; a) 3 hours at a peak temperature of 1250 °C (HP1250C), and b) 1.5 hours at a peak temperature of 1500 °C (HP1500C)

2.3.2 Diffusion bonding and annealing of FGW diffusion couples

The diffusion couples were prepared from the hotpressed FGW disk. The Ni-Cr alloy was prepared by arc melting nickel (Ni, Alfa Aesar, Tewksbury, MA, USA, 99.5% purity) and chromium (Zr Industrial Ltd, Shanghai, China, 99.9% purity, C 0.007%, Cu 0.002%, Fe 0.006%, P 0.002%, Si 0.006%, Al 0.005%, Cr balance) in an Ar atmosphere (Airgas, UHP Ar 99.999% purity). The arc melter used in this study consisted of a single arc electrode in a glass cylinder chamber and a chilled Cu hearth. The weighed pure components were piled together on the chilled Cu hearth. A Ti getter was also placed on the hearth beside a pile of pure components. Prior to melting, the chamber was evacuated (80 mbar) and backfilled three times with an Ar (Airgas, UHP Ar 99.999% purity). Before melting the pure components, the arc was pointed to the Ti first to melt the materials and initiate the oxygen gettinger process. To ensure homogenization of the melt, the melted button was flipped over and re-melted, and this process was repeated five times. After

melting, the button was annealed in an Ar atmosphere at 1250 °C for 50 hours to homogenize the alloy [36], [37].

The metal specimens (FGW and 80Ni20Cr) were cut by electrical discharge machining (EDM, Mitsubishi FX20K) into rectangular plates with lateral dimensions of 10 mm x 5 mm. The surface to be bonded was mechanically polished with SiC paper (grit sizes 320-1200) and diamond paste down to a 1 µm finish. A final polishing was conducted with 0.05 µm colloidal silica. After polishing, the specimens were cleaned by sonication in acetone for 10 minutes.

FGW plate and 80Ni20Cr plate were then diffusion bonded in a graphite-element furnace (Top loading graphite furnace, Oxy-Gon Industries Inc., Epsom, NH, USA) under an Ar atmosphere using a compression jig made of Molybdenum as shown in Figure 2.3. The couple assembled in the molybdenum jig was heated at 20 °C/minute to the target temperature of 1000 °C. After reaching the target temperature, the metal couple was held under isothermal conditions for 2 hours. The sample was then cooled at 20 °C/minute to 400 °C, which was the temperature at which the controller of the furnace could no longer control the cooling rate and the sample was then left to cool to room temperature in the furnace.

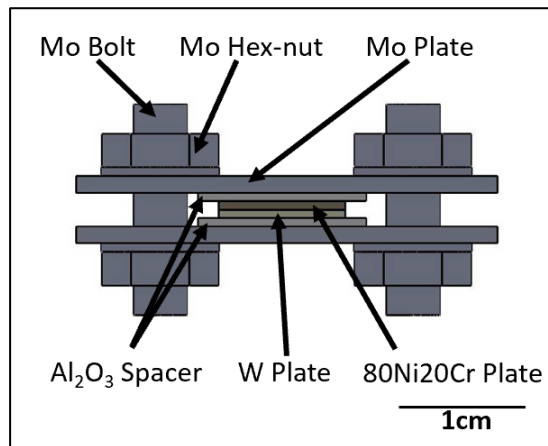


Figure 2.3. Schematic drawing of the Mo-based fixture for bonding the 80Ni20Cr/FGW diffusion couple

The diffusion-bonded couples (FGW/80Ni20Cr) were further annealed under Ar atmosphere (Airgas) at 1000 °C for an additional 48 hours. In total, the annealing time for a diffusion couple was 50 hours including the holding time of 2 hours during the bonding of the couples. At the end of the annealing treatment, a given diffusion couple was quenched by pulling it from the furnace,

placing it on a Cu plate, and blowing with UHP Ar through a ¼ inch diameter tube connected to a regulator with 10 psi flow setting. Figure 2.4 shows the schematic of the quenching set up.

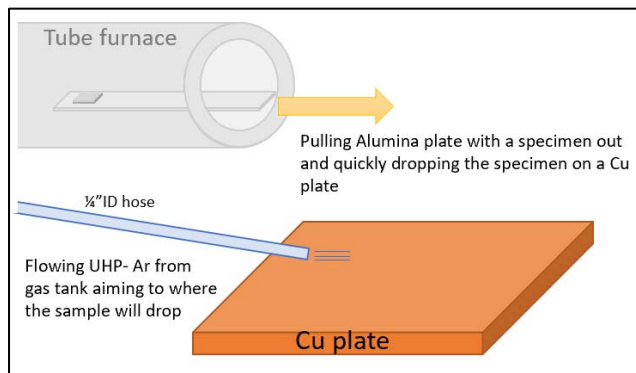


Figure 2.4. Schematic drawing of a set up for quenching diffusion couples

The diffusion couple was then mounted in epoxy resin (EpoxyMount, Allied High Tech Products, Inc., Rancho Dominguez, CA, USA) and cross-sectioned using a low-speed saw (Techcut 4TM Precision Low Speed Saw, Allied High Tech Products, Inc., Rancho Dominguez, CA, USA). The mounted, cross-sectioned couple was mechanically polished up to 1 µm diamond paste finish, followed by a final polish using 0.05-µm colloidal silica. After polishing, the cross-section was etched in a nitric acid (15.8 M) for 1 minutes followed by rinsing in DI water. Then the specimen was then lightly polished again by hand using 0.05-µm colloidal silica, followed by rinsing in DI water and drying in air for 30 minute at room temperature.

SEM-EDX (FEI Nova Nano SEM with Oxford INCA Energy 250 EDX system) with 15 kV acceleration voltage, 0.7 nA current was used to measure chemical compositions across the diffusion zone. To quantify the chemical composition derived from the EDX spectra of the samples, the spectra from a known Ni-W-Cr standard (71.2 wt%Ni, 6.0 wt%Cr, 23.5 wt%W), was collected using the same measurement parameters. Aztec software was used in this process. EDX spectra were collected from the standard and then the known composition, as determined by ICP-MS (Laboratory for Environmental Analysis, Center for Applied Isotope Studies, University of Georgia, Athen, GA, USA), was introduced to the software. The software stored the input composition with respect to the collected EDX spectra of the standard. Later, the stored standardized spectra was used to quantify the EDS spectra collected from specimens. The standard used here was prepared by arc-melting Ni (Alfa Aesar, Tewksbury, MA, USA, 99.95% purity), Cr

(Zr Industrial Ltd, Shanghai, China, 99.9% purity), and W (Midwest Tungsten Service, Willowbrook, IL USA, 99.95% purity.) The average effective interdiffusion coefficients for the diffusion between FGW and 80Ni20Cr were calculated by applying the method developed by Dayananda and coworkers [26]–[29].

2.3.3 Investigation of diffusion of Ni and Cr into FGW using TEM

In addition to microscopic investigation of the diffusion couples using SEM-EDX analyses, TEM (Talos 200X TEM, Thermo Fisher Scientific, Waltham, MA, USA) with STEM-EDX, and SAED techniques were also utilized to investigate a thin cross-section from the 80Ni20Cr/FGW couple annealed at 1000°C for 50 hours. The TEM was operated at 200 kV. The TEM analyses was conducted by SungHwan Hwang. Focused ion beam (FIB) milling was used to prepare a TEM cross-section using “lift-out” method (Omniprobe 200 lift-out system, (Oxford Instruments, Abingdon, UK), equipped with Quanta 3D FEG SEM). The chosen TEM cross-section possessed dimensions of ~ 12µm x 5 µm with ~ 100 nm thickness. The cross-section was chosen to contain a clear interface between a Ni-rich phase, and a W-rich phase with at least one region on the W-rich side containing a boundary between two W grains being perpendicular to the Ni-rich/W-rich interface.

2.3.4 Method used to obtain grain size measurement

Micrographs from specimen was used to determine \bar{L}_3 (mean intercept length of three-dimensional bodies) which represents average grain size of the specimen [34]. The \bar{L}_3 measurement was conducted, following standardize method suggested in ASTM E1382-97 [35], by placing random circles on the micrograph and counting number of grains intercepted by perimeter of the circles (N_i).

$$\bar{L}_3 = \frac{1}{N_L} = \frac{L_i}{N_i}$$

Micrographs was obtained from both the fracture surface of the FGW disk, and the polished and thermal etched cross-section of FGW disk. After the cross-section of the FGW specimen was polished to 0.5 µm finish, the specimen was thermal etched in Ar atmosphere (Airgas, UHP Ar 99.999% purity) at 1200 °C for 50 hours to reveal grain boundaries.

The LGW (commercially available) (99.95% purity, Midwest Tungsten Inc., USA). To reveal grain boundaries of this specimen, the polished cross-section was etched by immersion in a mixture of 3 parts of hydrochloric acid (12.1 M) and 1 part of nitric acid (15.8 M) at 80 °C for 2 minutes. Detail of \bar{L}_3 measurement from micrographs in this study are provided in Appendix B2.

2.4 Results

2.4.1 Characterization of as-received nano W powder

X-ray diffraction patterns, a TEM image, and the corresponding SAED patterns of the as-received powders, are presented in Figure 2.5 a), b), and c). Note that pure Ni was added to the specimen during the XRD analysis as a reference. The X-ray pattern suggested that the as-received nano W powders consisted of cubic tungsten (space group: Im-3m(229)) and β -W (space group: Pm-3n(223)). This observation was consistent with the result from the SAED analyses shown in Figure 2.5 c). The X-ray diffraction pattern was also used to estimate the crystalline size of the as-received nano W powder via the Williamson-Hall method [54]. The W-H plot from the XRD characteristic peaks of W (space group: Im-3m(229)) suggested crystalline size of 70 nm. On the other hand, the W-H plot from the characteristic peaks of β -W (space group: Pm-3n(223)) suggested crystalline size of 29 nm. However, the values are consistent with an observation from the micrograph shown in Figure 2.5 b). Details of the crystalline size calculation on the basis of Williamson-Hall method are presented in Appendix B1

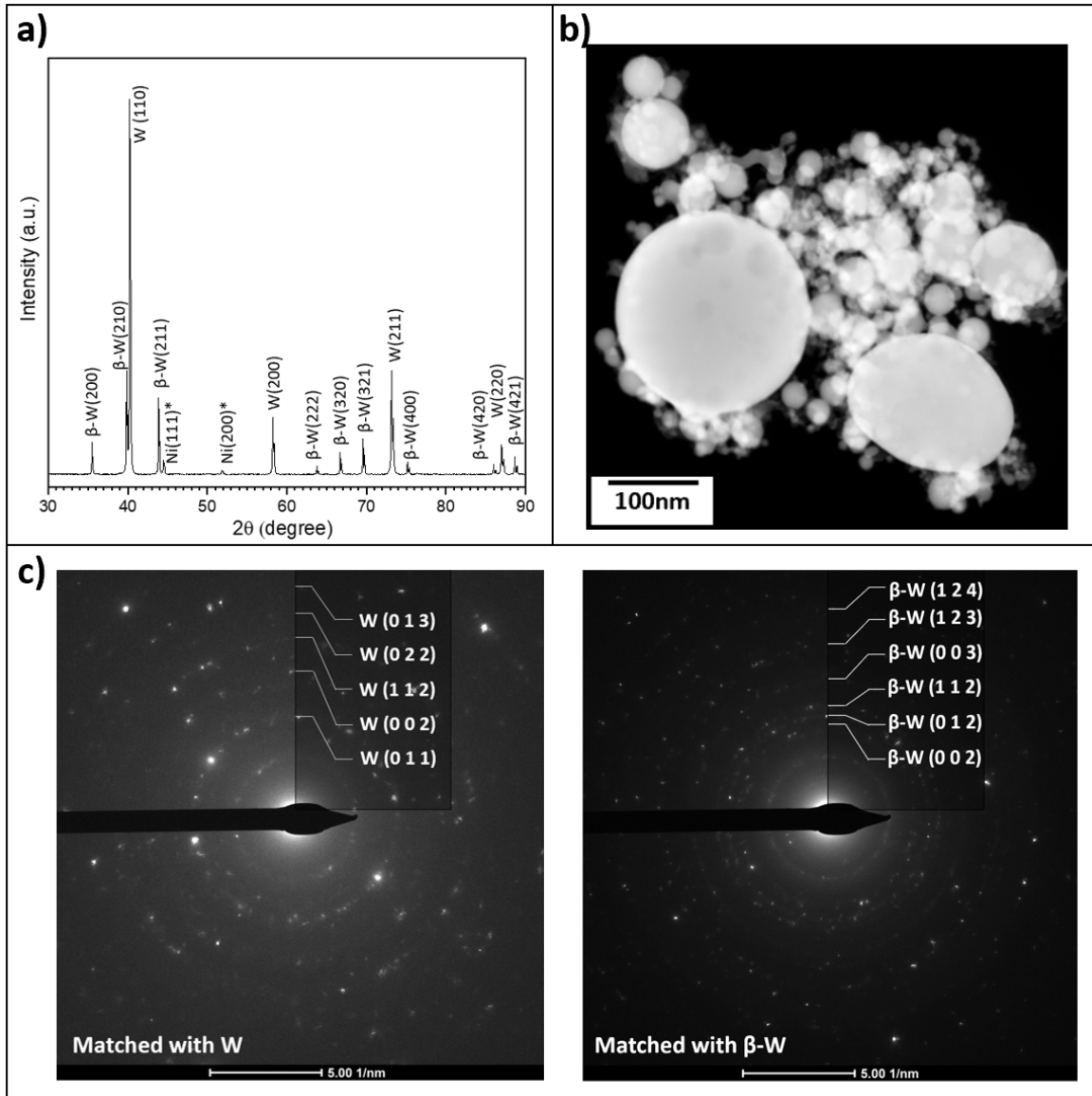


Figure 2.5. a) X-ray diffraction patterns of the as-received "80-nm" W powder, and b) TEM image of the powder together with the SAED analysis in c)

STEM-EDX analysis was also conducted on the as-received nano W powder. The high resolution EDX elemental maps shown in Figure 2.6 indicated the presence of a thin oxide layer covering the nano W powder.

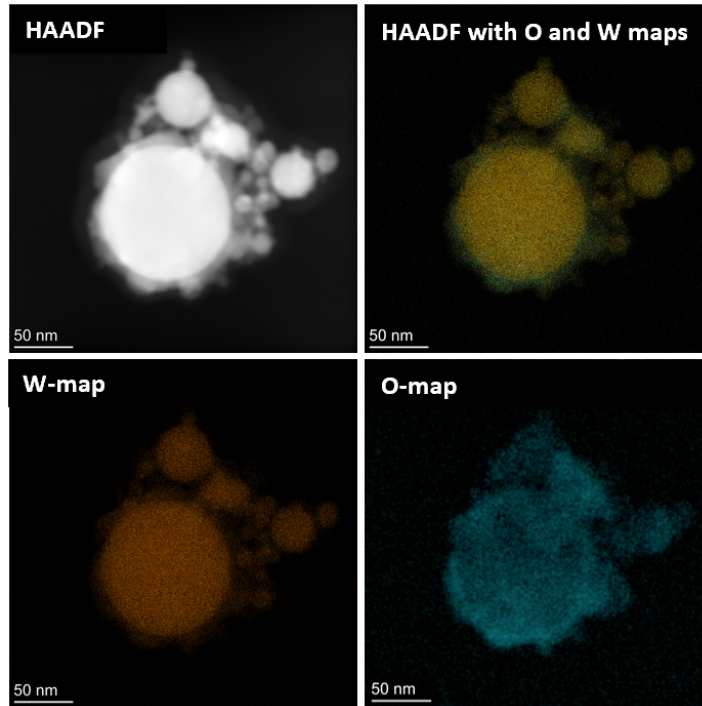


Figure 2.6. STEM-EDX elemental maps of the as-received “80-nm” W powders

2.4.2 Microstructure of the produced FGW

A SE image of a fracture cross-section of a FGW_CS1250C disk is shown Figure 2.7 a). The density of the green body after the compaction with 500 MPa pressure was $14.1 \pm 0.1 \text{ g/cm}^3$, which corresponded to a relative density of $73.2 \pm 0.6\%$, and the density of the disk after sintering was only $15.8 \pm 0.1 \text{ g/cm}^3$, which corresponded to a relative density of $81.9 \pm 0.7\%$.

SE images of fracture cross-sections of hot-pressed specimens; FGW_HP1250C, and FGW_HP1500C are shown in Figure 2.7 b) and c). The density of the two specimens after hot pressing were $16.7 \pm 0.2 \text{ g/cm}^3$ ($86.6 \pm 0.8\%$ dense) and $17.5 \pm 0.2 \text{ g/cm}^3$ ($91.0 \pm 0.9\%$ dense) respectively. The FGW_HP1500C disk possessed the highest density and was used as the FGW for diffusion couples.

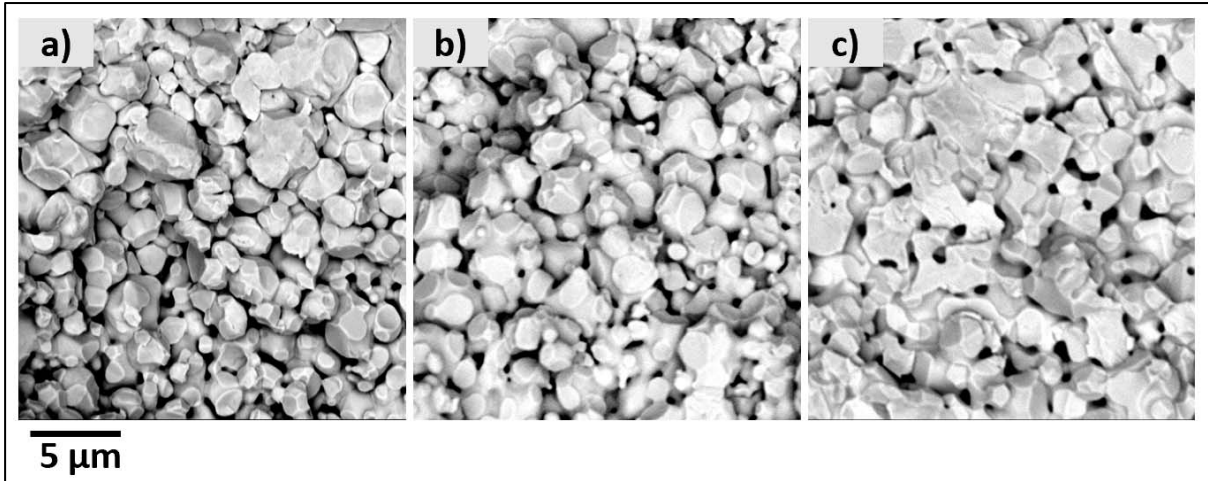


Figure 2.7. SE images of fracture surfaces from FGW disks produced via: a) compaction followed by pressureless sintering for 50 hours at 1250 °C, b) hot pressing at peak temperature of 1250 °C for 3 hours, and c) hot pressing at peak temperature of 1500 °C for 1.5 hours.

To evaluate how the microstructure of the FGW would change during the diffusion study, a small section from the FGW_HP1500C disk was annealed at 1200 °C for 50 hours in an Ar atmosphere. Figure 2.8 a) shows a fracture surface of the section after 50 hours at 1200 °C. Comparison of Figure 2.8 b) to Figure 2.7 c), indicate that there was no appreciable change in microstructure of the FGW after this thermal treatment.

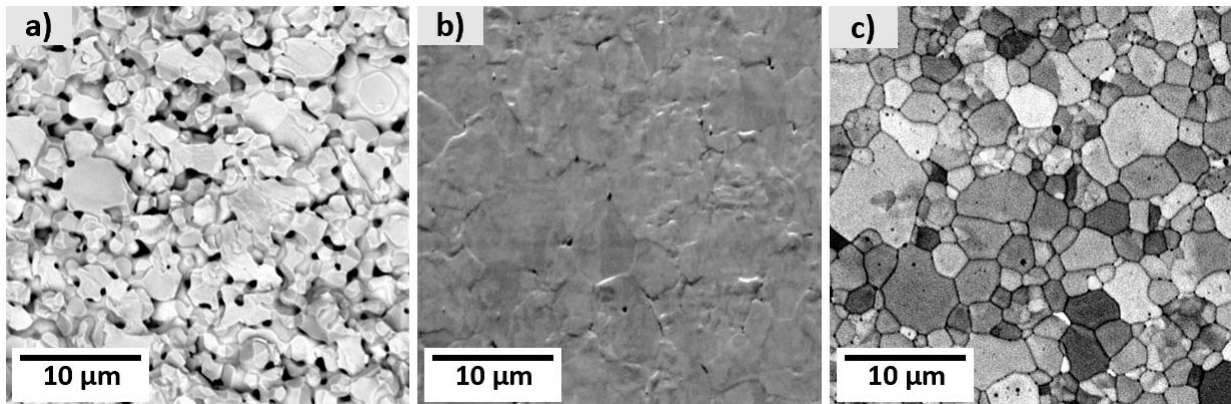


Figure 2.8. SEM images from the FGW_HP1500C disk after annealing at 1200°C for 50 hours: a) a fracture surface, b) a polished cross-section, and c) the thermal etched polished cross-section.

Figure 2.8 c) is a SEM image of the polished cross-section of the annealed section of the FGW_HP1500C disk. The polished surface of the cross-section was thermal etched during the long annealing; therefore, a clear distinction between each W grain can be observed. By qualitatively comparing the microstructures as shown in the thermal etched surface and the fracture surface, one can see that both are consistent to each other in terms of grain size distribution. Both images suggest that the FGW_HP1500C disk consists of W grains with different size, ranging from a few microns to sub-microns. However, unlike the microstructure of the fracture surface, the microstructure of the polished cross-section did not contain any porous features. Therefore, it can be misleading if a comment about porosity of the sintered disk is made based on the microstructure from the polished cross-section.

Since the microstructure from the thermal etched polished cross-section has a clear distinction between each W grains, the micrograph was used to determine \bar{L}_3 . The \bar{L}_3 as determined from the micrograph of as shown in Figure 2.8 c), was $2.3 \pm 0.1 \mu\text{m}$. Detail of \bar{L}_3 measurement from micrographs in this study are provided in Appendix B2.

EBSD analysis of the polished cross-section of the specimen was also used to obtain the average grain size. An inverse pole figure (IPF) map, a map with highlighted grain boundaries, and a map with unique grain coloring (generated by OIM Analysis software) obtained from the polished cross-section of the FGW_HP1500C specimen are shown in Figure 2.9. The average grain size as estimated from the software was $3.2 \pm 2.8 \mu\text{m}$, which was consistent with the determined \bar{L}_3 value. However, the digitally generated micrographs, as shown in Figure 2.9, present slight vertical elongation when they were compared to the micrographs from SEM as shown in Figure 2.8. This is because the tilt correction from the OIM software was not accurate. Therefore, the \bar{L}_3 value as measured from the thermal etched micrograph was selected as a representative value for average grain size of the produced FGW.

The \bar{L}_3 value was also determined from the micrograph of the LGW. The LGW plate was obtained from Midwest Tungsten Inc. The LGW was produced by sintering and rolling. A BSE image of chemically etched polish cross-section of the LGW is shown in Figure 2.10. The \bar{L}_3 obtained from this micrograph was $29.3 \pm 3.2 \mu\text{m}$, which was more than an order of magnitude larger than the average grain size of the produced FGW.

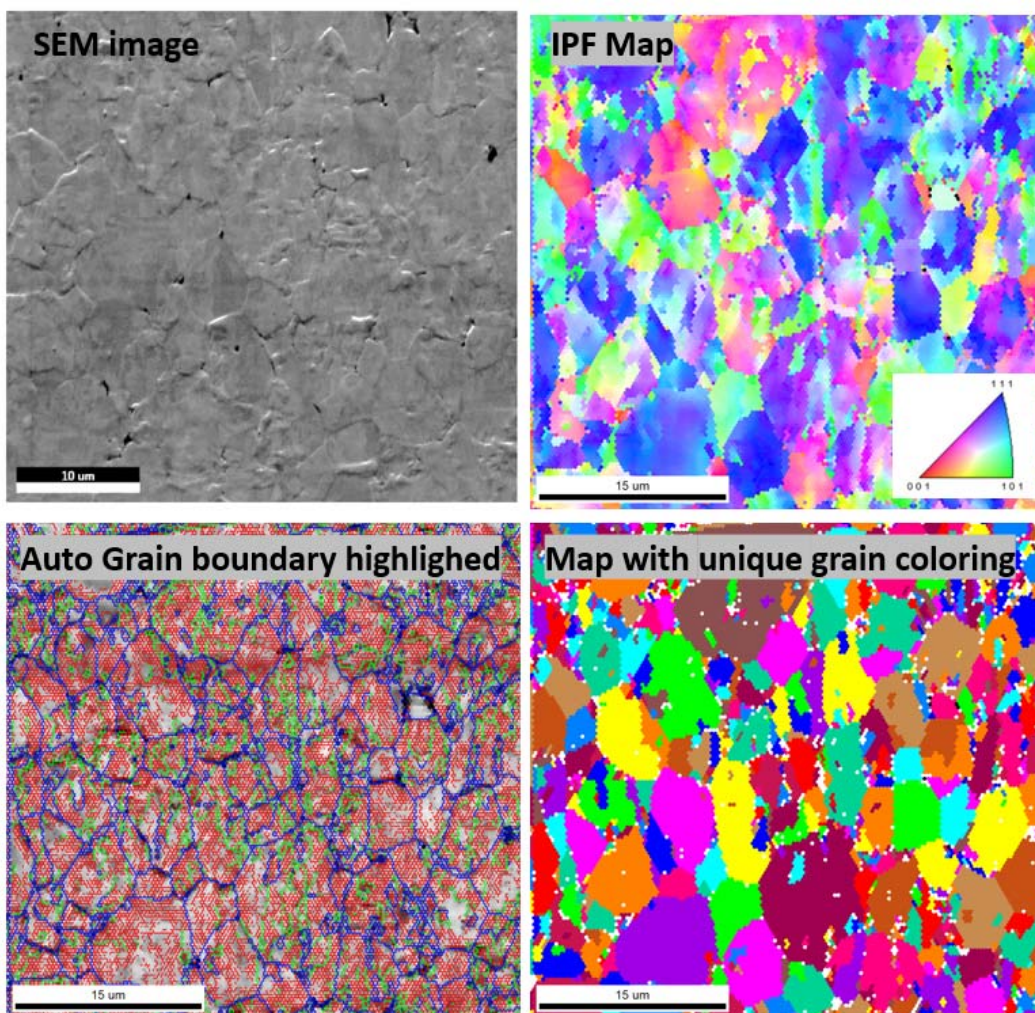


Figure 2.9. Different graphical displays generated from EBSPs collected from the polished cross-section of the FGW_HP1500C disk

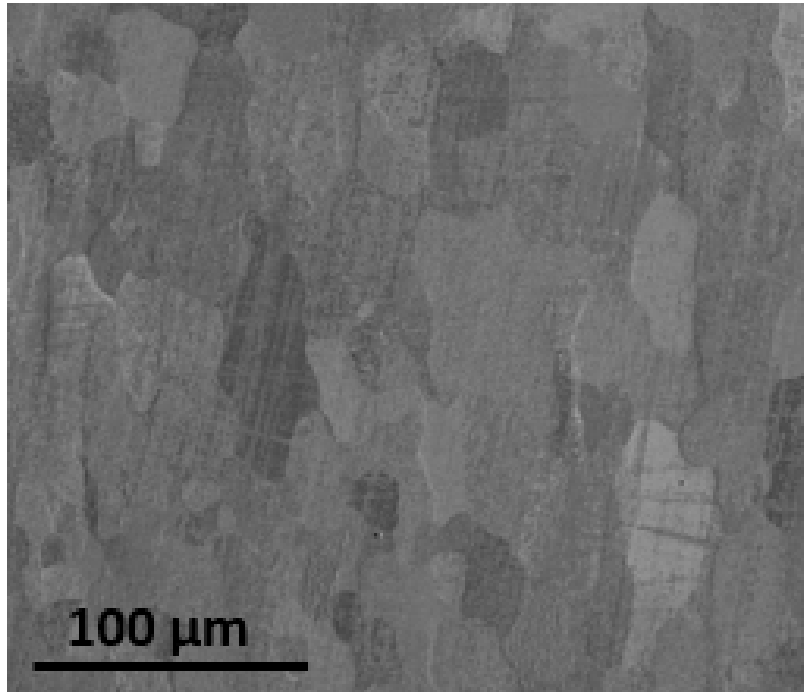


Figure 2.10. BSE images of an etched polished cross-section of the LGW (99.95% purity, Midwest Tungsten Inc., USA) used in this study

2.4.3 Diffusion of Ni and Cr into W with different grain size

The concentration profiles obtained from FGW/80Ni20Cr and LGW/80Ni20Cr samples after annealing for 50 hours at 1000 °C as measured by SEM-EDX analyses (dots) and the interpolated profiles (lines) are shown in Figure 2.11. The profiles from the couple comprised of FGW are shown in black, and the profiles from the couple comprised of LGW are shown in red. For the region in the α -phase, the difference in compositions between the two couples at each location are ≤ 5 at% for W, ≤ 3 at% for Cr, and ≤ 5 at% for Ni. The region with the largest compositional difference for Ni and W is between $x=9 \mu\text{m}$ and $x=12\mu\text{m}$, which is the region with the highest composition gradient on the α -phase. For the region in the β - phase, the difference in compositions between the two couples at each location are ≤ 3 at% for W, ≤ 1 at% for Cr, and ≤ 3 at% for Ni. However, there is no appreciable differences were apparent in the overall feature of the concentration profiles between the diffusion couples with FGW and with LGW.

The calculated values of the average effective interdiffusion coefficients, $\tilde{D}_{i,\Delta C}^{eff}$, together with the corresponding characteristic interdiffusion depths, $d_{i,\Delta C}$, are listed in Table 2.1. In the same

manner as explained in the previous chapter, the calculation was made by dividing the diffusion profiles into 2 regions, the LHS region of the α/β interface (α -phase region), and the RHS region of the α/β interface (β -phase region).

As can be seen in Table 2.1, the average effective interdiffusion coefficients, and the characteristic interdiffusion depths were similar for the diffusion couples with FGW and with LGW. Figure 2.12 provided side-by-side comparison of elemental maps from SEM-EDX measurements of the diffusion couples with FGW and LGW. The maps as shown here, covered more area on the W-side, since the study was focused on investigating the diffusion of Ni and Cr into W with different microstructures. Qualitative comparison of the distribution of elements from the maps indicated that there was no appreciable difference between the couples with FGW and LGW that were annealed at 1000 °C.

Table 2.1. Average effective interdiffusion coefficients and characteristic depth of penetration for the regions on the LHS, and on the RHS of the α/β interface for the FGW/80Ni20Cr couple, and the LGW/80Ni20Cr couple

Experimental Condition		Average effective interdiffusion coefficient [$\mu\text{m}^2/\text{s}$]			$d_{i,\alpha}$ or $d_{i,\beta}$ [μm] for		
		\tilde{D}_W^{eff}	\tilde{D}_{Cr}^{eff}	\tilde{D}_{Ni}^{eff}	W	Cr	Ni
FGW 1000 °C, 50 Hours	α -phase	4.3E-05	3.4E-05	2.4E-05	6.4	7.1	5.9
	β -phase	3.5E-05	3.2E-05	2.3E-05	2.8	2.6	2.8
LGW 1000 °C, 50 Hours	α -phase	6.7E-05	5.0E-05	4.1E-05	7.3	9.3	6.5
	β -phase	3.8E-05	3.6E-05	2.5E-05	2.7	2.6	2.8

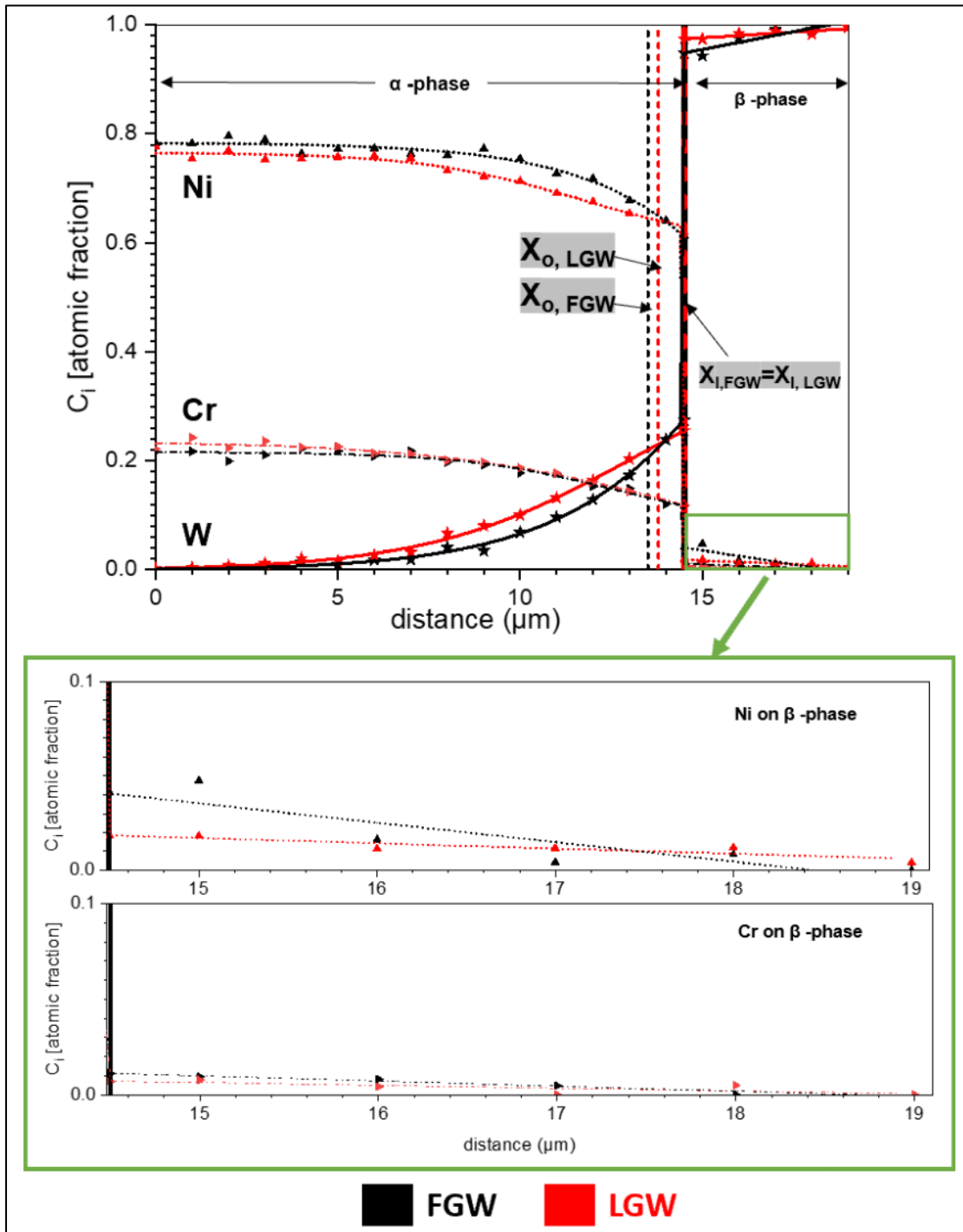


Figure 2.11. Concentration profiles from FGW/80Ni20Cr couple annealed at 1000 °C for 50 hours (in black color), and LGW/80Ni20Cr couple annealed at 1000 °C for 50 hours (in red color)

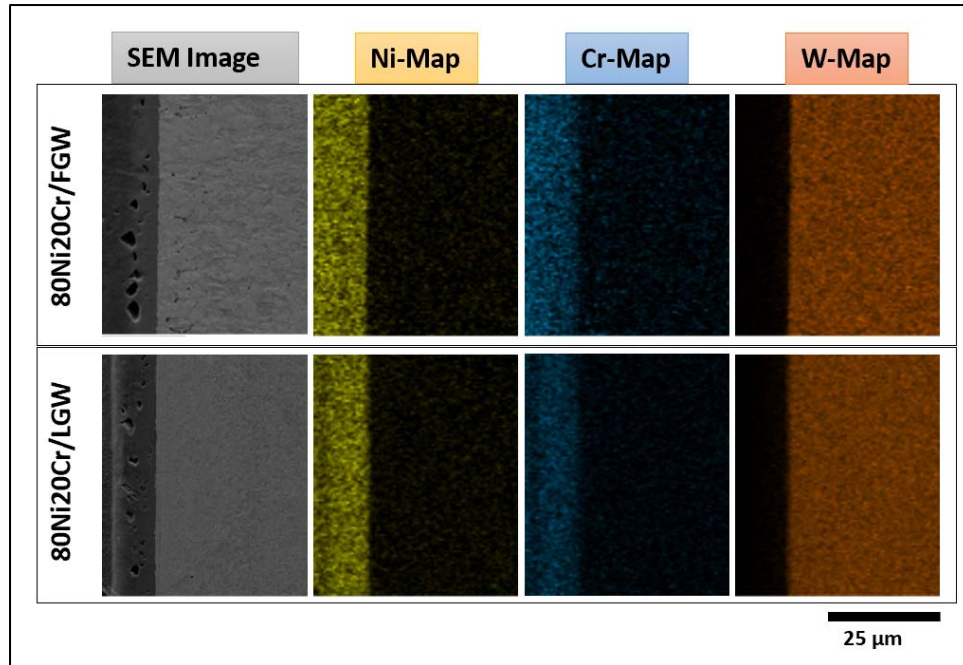


Figure 2.12. Elemental maps obtained from SEM-EDX analyses of polished cross-sections of the FGW/80Ni20Cr and LGW/80Ni20Cr diffusion couples annealed at 1000 °C for 50 hours

In addition to the SEM-EDX analyses, STEM-EDX analyses were also used to investigate the diffusion of Ni and Cr into FGW at higher magnifications at the interface between the Ni-rich phase and the W- rich phase. The TEM cross-section was obtained from the FGW/80Ni20Cr couple annealed at 1000 °C for 50 hours. Elemental maps showing distribution of elements in the two phases are presented in Figure 2.13 a). From the Ni-map, the area as shown in the circle has slightly brighter color indicating that more Ni atoms are detected at that region. The circled location reveals a junction where two tungsten grains met.

STEM-EDX line scans were also conducted across grain boundaries between tungsten grains adjacent to the Ni-rich/W-rich interface (Lines 1 and 2). The locations of the scans are shown as dotted-lines in the STEM-image in Figure 2.13 a). The concentration profiles across the W grain boundaries are shown in Figure 2.13 b). The profile from Line 1 shows a small deviation in concentration of Ni, Cr and W at the grain boundary location. The deviation was less obvious in profile from Line 2. This deviation suggested that grain boundaries of W adjacent to the Ni-Cr rich phase acted as slightly enhanced diffusion paths for Ni and Cr.

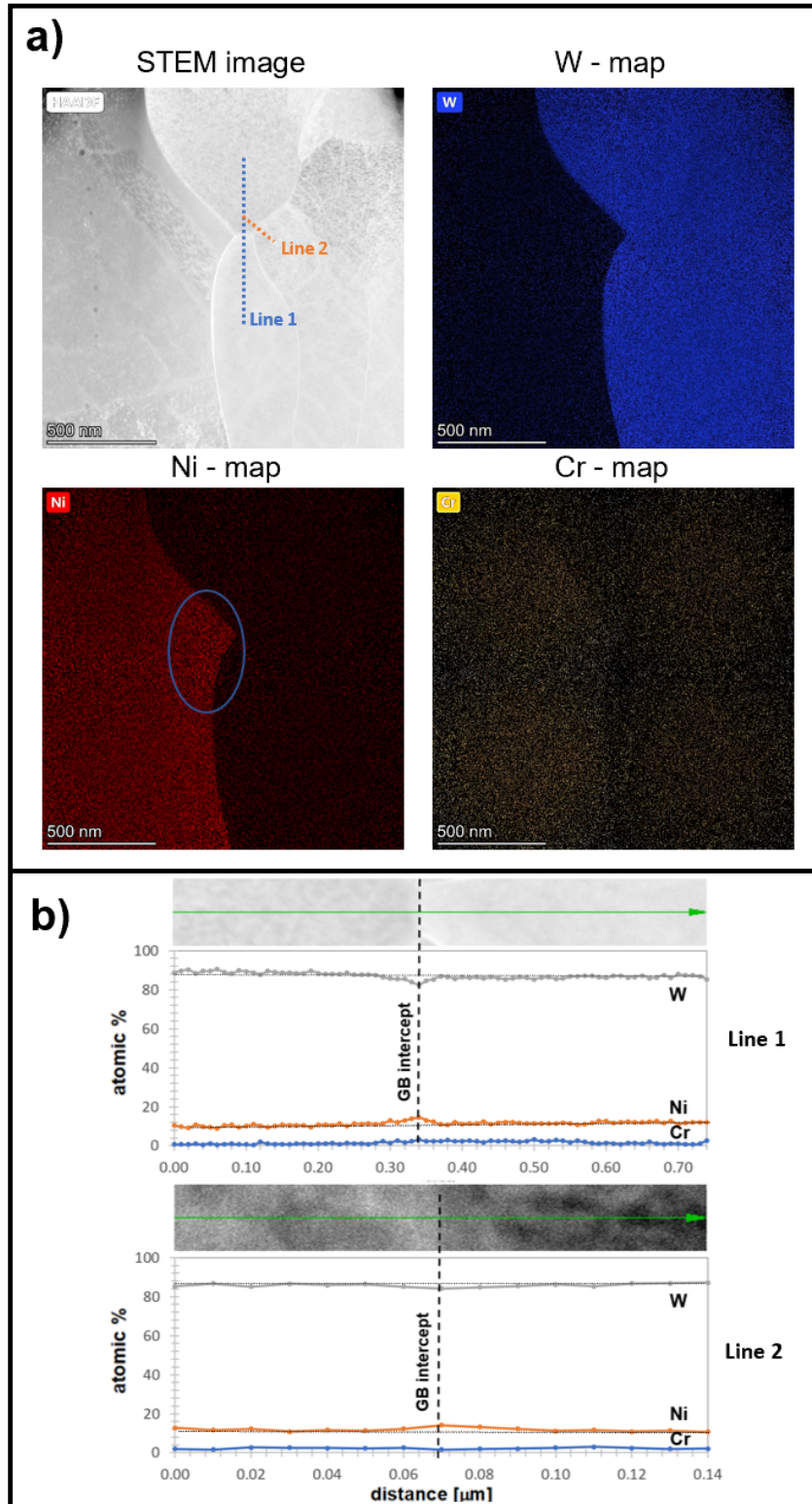


Figure 2.13. High-resolution STEM-EDX analyses of an ion-milled cross-section of a FGW/80Ni20Cr diffusion couple annealed at 1000°C for 50 hours; a) elemental maps, b) line scans showing composition deviation across the W grains as indicated by the dotted lines in a)

During TEM investigation of cross-section from the FGW/80Ni20Cr diffusion couple annealed at 1000 °C for 50 hours, SAED analyses were also performed at regions close to the Ni-rich/W-rich interface, as shown in Figure 2.14, to determine whether a thin intermetallic phase had formed close to the interface. The formation of intermetallic layer was reported by Karpinos, et al. [30] in their diffusion study in the Ni-Cr-W system at 1000°C -1200°C. However, the SAED analyses in this present study did not reveal the formation of intermetallic phases. The SAED pattern that was collected from area “A” in the Ni-rich phase close to the interface, as shown in Figure 2.14, matched with the theoretical pattern from Ni-rich phase. Similarly, the SAED pattern that was collected from area “B” in the W-rich phase matched with the theoretical pattern for W-rich phase.

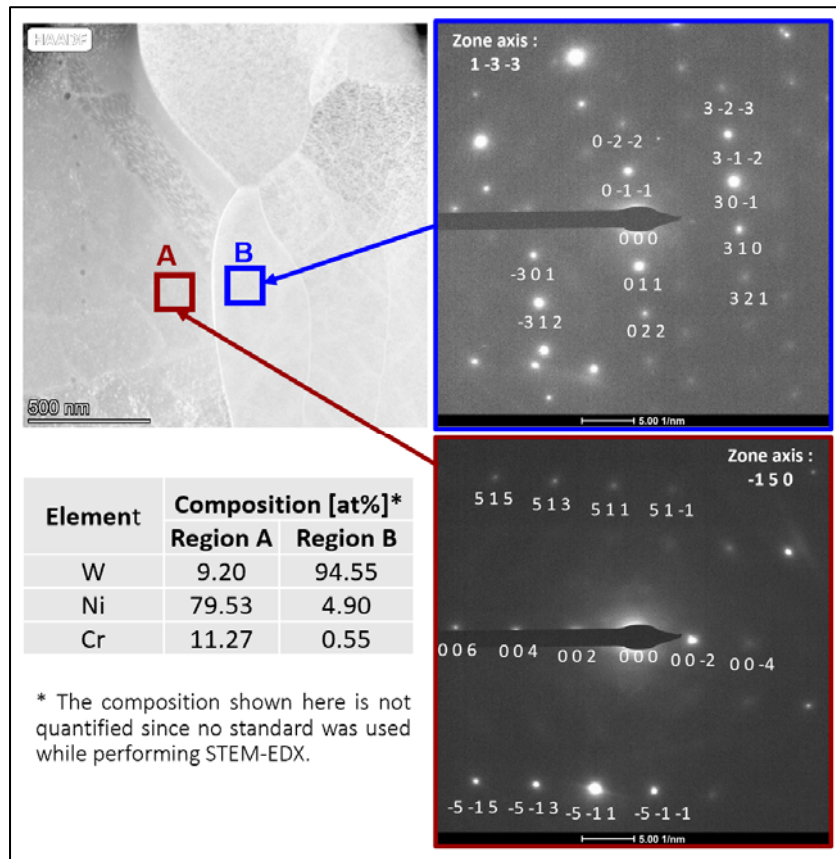


Figure 2.14. SAED patterns from two regions; the Ni-rich phase (box A), and the W-rich phase (box B) together with the measure composition of each regio

2.5 Discussion

A $90.9\pm 0.9\%$ dense FGW disk that was used for the diffusion studies in this work was produced via hot pressing method. There are two common approaches to increase the sinterability of tungsten powder; i) addition of an alloying element, and ii) refinement of particle size [49], [55], [56]. Several studies had been done to produce FGW; however, without an addition of other alloying elements fully dense sintered product cannot be achieved without the use of spark plasma sintering method which requires excessively high pressure, ~ 200 MPa to assist the densification [50], [57], [58].

Ren, et al. [51] indicated that 98.3% dense pure tungsten could be produced via compaction and pressureless sintering. However, a similar attempt that was conducted in this study, yielded a sintered disk that was only $81.9\pm 0.7\%$ dense. The reason that the higher density was not obtained in the present work could be a difference in the initial grain size of the tungsten powder.

The reduction step proposed by Ren, et al. was necessary to remove a thin oxide layer formed around the nano W powder during processing. High resolution TEM-EDX elemental maps of the as-received nano W powder revealed the presence of thin oxide layer covering W powder as shown in Figure 2.6.

In terms of the diffusion behavior of Ni and Cr, as indicated by the overall concentration profiles as measured by the SEM-EDX analyses, the diffusion distances of Ni and Cr into LGW and FGW were not appreciably different at the studied temperature. A difference in the overall diffusion profile might be present at temperatures lower than 1000 °C, and a study at such lower temperatures may confirm such significantly enhanced grain boundary diffusion. For the scope of this study, a temperature lower than 1000 °C was not chosen because the W/80Ni20Cr couples that were diffusion bonded at lower temperatures tended to debond even with careful handling. Keeping a bulky fixture to hold the couples during annealing was not also applicable for this study, since the couples could not be quenched fast enough to avoid intermetallic formation. As discussed in the previous chapter, a high quenching rate was crucial for avoiding the formation of intermetallic phases.

Knowing that the concentration profiles of Ni and Cr into the W-rich region were not sensitive to the W grain size, one can apply this finding to applications that require only surfacial modification of tungsten such as wear resistant coating or corrosion resistant coating. This type of approach can be cost efficient since there is no need to use a large quantity of expensive alloying

elements to alloy the entire part. In addition, from the average effective interdiffusion coefficients as derived in this study, the diffusion rate can be predicted, which can be useful for controlling the surface alloying process.

2.6 Conclusion

A FGW disk with an average grain size of $2.3 \pm 0.1 \mu\text{m}$ was produced by hot pressing. A FGW/80Ni20Cr couples were diffusion bonded and annealed at the temperature of interest in this which is 1000°C and 1200°C . The key findings from this study are as follows.

- In the α -phase and β - phase, the differences in compositions between the diffusion couples made with FGW and LGW at each location are $\leq 5 \text{ at}\%$ for all elements. However, there was no appreciable differences in the overall feature of the concentration profiles as measured by SEM-EDX analyses.
- The average effective interdiffusion coefficients and the characteristic interdiffusion depths on the α -phase, and β -phase were similar for FGW-bearing, and LGW-bearing diffusion couples at 1000°C .
- Even though the STEM-EDX analyses suggested that it was slightly preferable for Ni atoms to diffuse into W via grain boundaries; volume diffusion still governed the process at 1000°C for $2.3 \mu\text{m}$ grain size W.
- The SAED patterns collected from the area on the Ni-rich side and W-rich side of the interface support the finding in the previous chapter that there was no formation of an intermetallic layer in the diffusion zone at 1000°C .

3. LIQUID PHASE BONDING OF ZrC/W TO ZrC/W WITH NICKEL-INTERLAYER

3.1 Abstract

In this study, ZrC/W composites produced by the Displacive Compensation of Porosity (DCP) method were joined together by a liquid phase bonding technique using Ni as an interlayer. Effects of the bonding temperatures, ranging from 1300-1500 °C, on the bonding strength at room temperature and on the microstructure of the bonded area were investigated. While the highest shear strengths of 145.0 ± 52.1 MPa was achieved with the specimens bonded at 1500 °C. The average shear strengths at room temperature for each bonding temperature were not significantly different at a 95% confidence level. Two types of failure, i) failure at the seam area, and ii) failure within the ZrC/W substrate, were observed. From the specimen bonded at 1500 °C, the highest amount of solidified ZrC crystals were observed at the seam area together with small pores between the crystals. Residual Cu, present in the ZrC/W-based composite produced via the DCP process, migrated to the bonded interface, and acted to lower the melting point while interacting with the Ni- interlayer. This interaction allowed a liquid phase to form at 1300 °C.

3.2 Introduction

ZrC/W is a ceramic metal composite with superior thermal conductivity and failure strength at high temperature and pressure relative to nickel-based alloys [8], [19], [60]. Such composites are attractive for use in high temperature applications, such as in a heat exchanger that can operate at 750 °C and 20 MPa internal pressure [8]. Several approaches have been developed to produce ZrC/W composites [59] such as the Displacive Compensation of Porosity (DCP) process [8], [19], [60], powder processing and sintering (Hot Pressing) [61], [62], Spark Plasma Sintering (SPS) [63], and In Situ Reactive Sintering (SRS) [64].

Several bonding techniques, such as diffusion bonding, transient liquid phase bonding, and brazing have been conducted to bond ceramic-metal composites (cermets) to metals [65]–[69]. However, there is no report on a method to bond the ZrC/W to ZrC/W in order to produce a more complex-shape components. ZrC/W is prone to oxidation at high temperatures [8]; therefore, a practical bonding process for this material requires a feasible execution in a controlled atmosphere.

Diffusion bonding is one method that can be conducted in a controlled atmosphere. In several applications, such as in nuclear reactor components, a Ni interlayer has been used in diffusion bonding [70]. However, Ni and W tend to react to form intermetallic compounds at high temperatures [11], [31]. Several studies have suggested that the intermetallic layer can affect the strength of the bond [69]–[71]. Solid-state diffusion bonding using Ni as an interlayer may also be used to bond ZrC/W to ZrC/W. However, residual Ni between the bonded materials may be the weakest section, since the strength of Ni drops significantly at high temperatures. The shear strength of Nickel 200 was reported to decrease from 283 MPa to 183 MPa after heating to 540 °C [72]. Hence, a liquid phase diffusion bonding using Ni as a transient insert metal is considered here. A study by Han, et al. [68] has shown that a Ti-61Ni filler can be used to join TZM to ZrC-particle-reinforced tungsten. Therefore, it should be feasible to use a similar method employing Ni to aid in joining ZrC/W to ZrC/W.

Note that the ZrC/W composite used in the study by Han, et al. [68] was different from the composite being used in this study. While the method to produce ZrC_p-W composite in the study was not reported by Han, et al., ZrC particles resided in a W matrix. On the other hand, the ZrC/W being used in this study was produced by the DCP process. The first step for this process is to fabricate a WC preform, such as by compacting and sintering WC powders. Next, the preform with an appropriate porosity is infiltrated by a Zr₂Cu liquid. Zr in the melt can then react with the WC preform to yield ZrC and W. A majority of Cu in the melt is pushed out to the surface (due to filling of prior pores by the more voluminous ZrC and W products) and is removed by subsequent chemical etching. Therefore, ZrC/W-based composites produced by the DCP method consist of W particles within a ZrC matrix, along with a small amount of residual Cu and residual WC.

For this study, Ni foil was chosen as an interlayer for bonding ZrC/W to ZrC/W since the melting point of Ni is lower than the ZrC/W substrate. In addition, from phase diagrams of Ni-W (Figure 3.1) [32], and Ni-ZrC (Figure 3.2) [77], interactions of Ni with W and Ni with ZrC also reduce the melting point. Ni foil is also commercially available in various thicknesses.

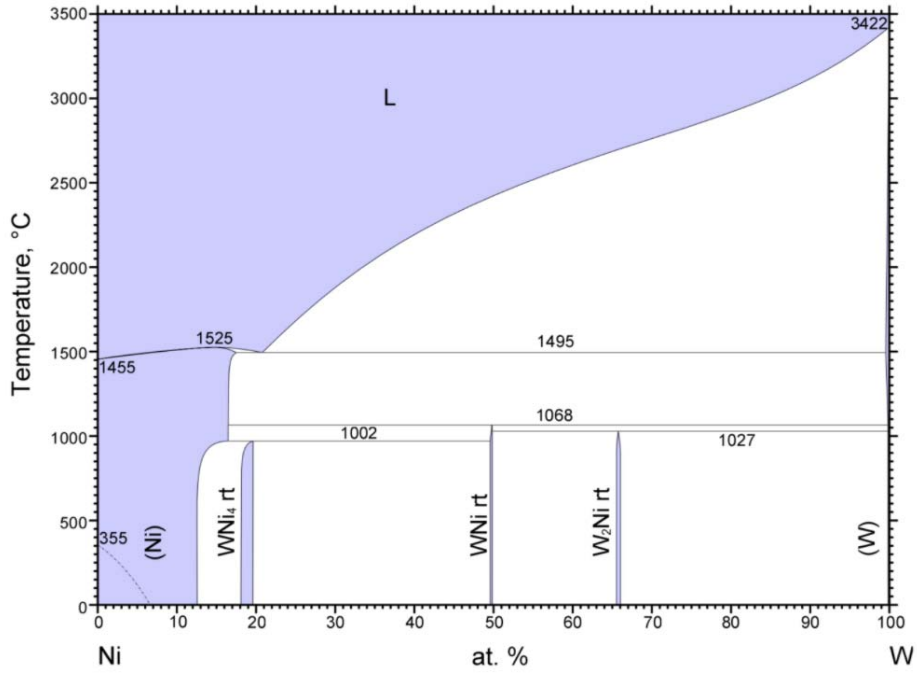


Figure 3.1. Ni-W phase diagram [32]

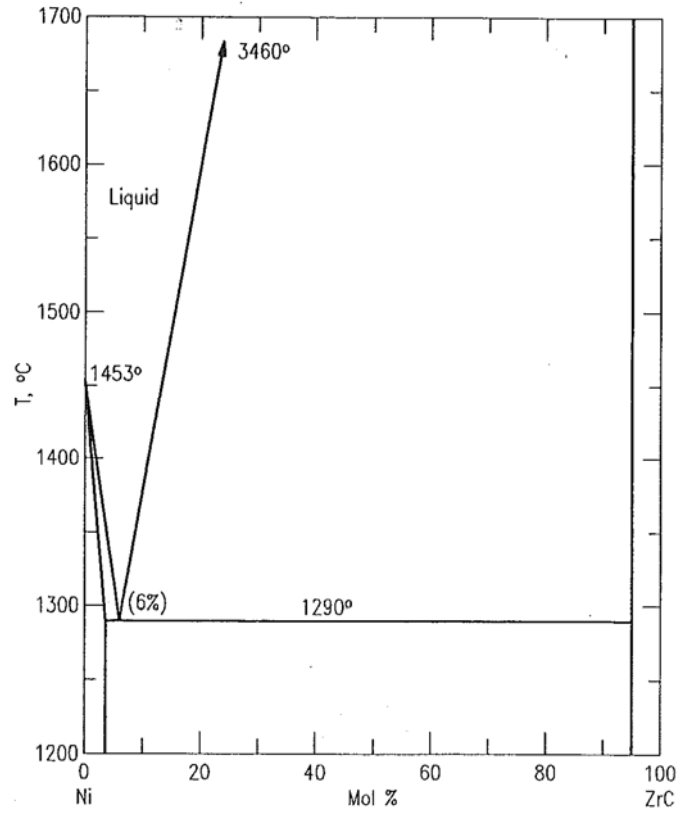


Figure 3.2. Ni-ZrC phase diagram[77]

The purpose of this study is to evaluate a liquid bonding technique using a Ni interlayer to bond a ZrC/W-based composite plates together. Effects of bonding temperatures on the microstructure and strength of the bond will be discussed. In addition, a wetting experiment of Ni on a ZrC/W plate was also conducted to investigate the interaction of the molten Ni with ZrC /W.

3.3 Experimental Procedure

3.3.1 Production of ZrC/W-based composite via DCP process

A plate of ZrC/W-based composite that was used in this study was produced by researchers (Dr. Tumurugoti Priyatham, and Wang Yujie) in the Sandhage Lab (Purdue University). Porous W plates (9 cm x 15 cm x 6mm) were fabricated by uniaxial compaction of WC powder (SC55S, Global Tungsten & Powders, Corp, Towanda, PA, USA) that was mixed with isobutyl methacrylate (IBMA) (Elvacite 2045, Lucite International, USA). After compaction, the IBMA binder was removed by evaporation, and the preform was lightly sintered in a single heating process in an Ar atmosphere (UHP Argon 99.999% Purity, Airgas, USA) by heating at 10 °C/minutes followed by a 2 hour sintering treatment at 1400°C.

Zr₂Cu liquid was introduced into the preform by “an *in-situ* alloying, single-step, static melt infiltration” method developed by the Sandhage research group (Dr. Caccia Mario Raul, Dr. Tumurugoti Priyatham, and Wang Yujie, Strayer Alexander R., Jorge Hugo Ramirez Velasco). The melt infiltration process was conducted by placing a sintered WC preform within a graphite tray (AR-8, Ohio Carbon Blank, Willoughby, OH, USA). A Zr plate (Zr-alloy 702, Eagle Alloys Global Materials Supplier, Talbott, TN, USA), and a Cu plate (Cu-alloy 110, McMaster-Carr, USA) were cut to the lateral dimension of the sintered WC preform. The thicknesses of Zr and Cu plate were determined for an overall composition of Zr₂Cu liquid, with sufficient Zr₂Cu liquid for completion of infiltration and reaction for a given sintered porous WC preform. A schematic illustration of the assembly for the static reactive melt infiltration is shown in Figure 3.3. The assembly was loaded into a vacuum furnace, evacuated (to 10⁻² Torr) and back-filled with UHP Ar, and this evacuation/backfilling process was repeated three times. Before heating at 15 °C/minute to 1150°C, the furnace was evacuated again to 10⁻² Torr. The furnace was held at 1150°C for 2 hours to allow for in-situ melt alloying. Next, oxygen-scrubbed Ar (pO₂≤10⁻¹⁴ atm) was introduced to raise an overall pressure of the furnace chamber to 760 Torr. Next the furnace

was heated at 15 °C/ minute to 1350 °C and held for 2 hours to allow for reactive conversion of WC into ZrC/W. The assembly was cooled at 15 °C/minute to room temperature.

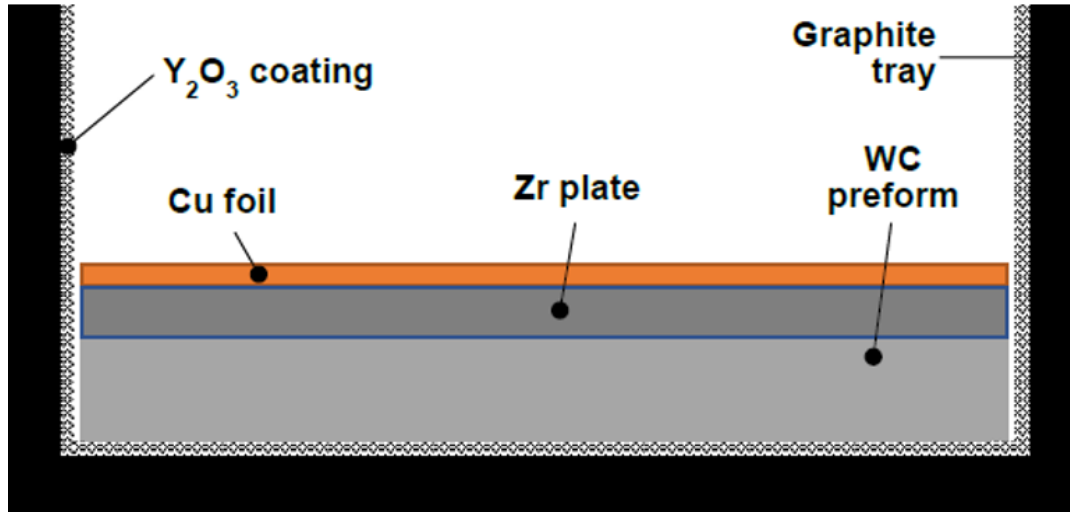


Figure 3.3. Schematic illustration of the assembly for static reactive melt infiltration

After the infiltration process, the reacted ZrC/W-based composite plate was covered with excess solidified Zr-Cu liquid, which was removed by etching in aqua regia (3M HCL: 1M HNO₃) for 2 hours at room temperature. An XRD pattern obtained from a plate generated by this static infiltration method is shown in Figure 3.4. The composite consisted of 51.9 vol% ZrC, 32.3 vol% W, 2.0 vol% residual WC, and 13.8 vol% residual Cu. The quantitative phase analysis of the ZrC/W-based composited is described in Appendix C1. Since the developed method is a DCP-based process, the ZrC/W-based composites produced via this method are referred to herein as DCP-derived ZrC/W-based composites.

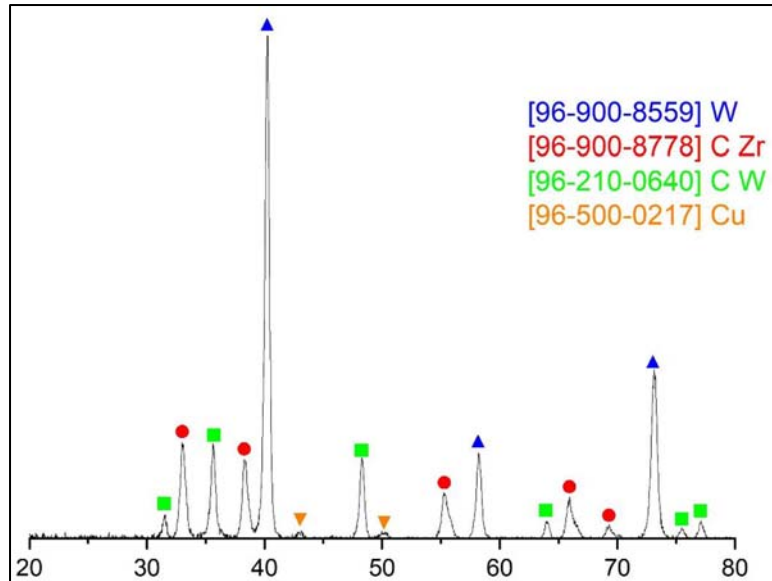


Figure 3.4. XRD pattern obtained from a plate generated by the static reactive infiltration DCP method

3.3.2 Removal of residual Cu from the DCP-derived ZrC/W-based composite

A procedure was conducted to remove residual Cu in the ZrC/W-based composite produced via the DCP process. A larger plate of DCP-derived ZrC/W was machined by EDM into 5 mm x 5 mm x 4 mm plates. The 5 mm x 5 mm faces of the specimens were mechanically polished with diamond impregnated pads to a final finish of 9 μm . The polished specimens were then annealed in a graphite furnace (Top loading graphite furnace, Oxy-Gon Industries Inc., Epsom, NH, USA) at 1100 $^{\circ}\text{C}$ for different times ranging from 4 hours to 40 hours. After annealing, excess Cu that migrated to the external surfaces of the specimens was dissolved in nitric acid (15.8M) for 1 hours, followed by rinsing in water, and sonication in acetone for 10 minutes. The cleaned specimens were dried in air at room temperature for 3 hours before measuring the weight change associated with Cu removal.

3.3.3 Liquid phase bonding of ZrC/W to ZrC/W

ZrC/W-based composites produced via the DCP process were machined into two different plate sizes by EDM; one with dimensions of 10 mm x 15 mm x 3 mm and the other with dimensions of 5 mm x 5 mm x 5 mm. The machined ZrC/W plates were mechanically polished using diamond impregnated pads to a final finish of 9 μm .

The external residual Cu from the ZrC/W-based composite was removed by etching the polished specimen in nitric acid (15.8 M) for 30 minutes. Figure 3.5 shows W, Zr, Cu and C elemental maps from polished ZrC/W surface after such nitric acid etching. Only a small amount of Cu presented in the etched surface; therefore, the Cu-map appear to be dark.

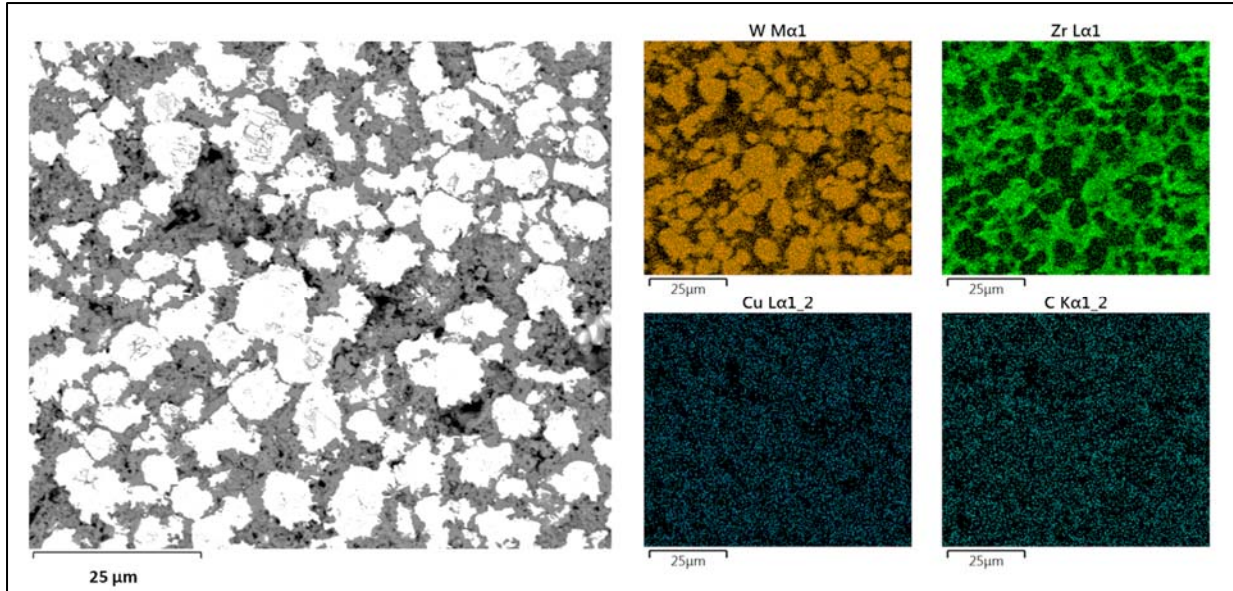


Figure 3.5. Elemental mapping of ZrC/W substrate after etching in nitric acid (15.8 M) for 30 minutes.

The 25- μm -thick Ni foil (Alfa Aesar, Tewksbury, MA, USA, 99.7% Ni, 170 ppm C, 200 ppm Cu, 100 ppm Mg, 10 ppm S, 30 ppm Ti, 40 ppm Co, 200 ppm Fe, 1800 ppm Mn, 400 ppm Si) of 6 mm x 24 mm dimensions was folded to produce a single 6 mm x 6 mm Ni interlayer of 100 μm thickness. All components were assembled as shown in Figure 3.6 just before the bonding experiment to minimize the oxygen exposure time of the polished surfaces. Before each assembly, the polished ZrC/W plates and the cut Ni strip were ultrasonically cleaned in acetone for 10 minutes.

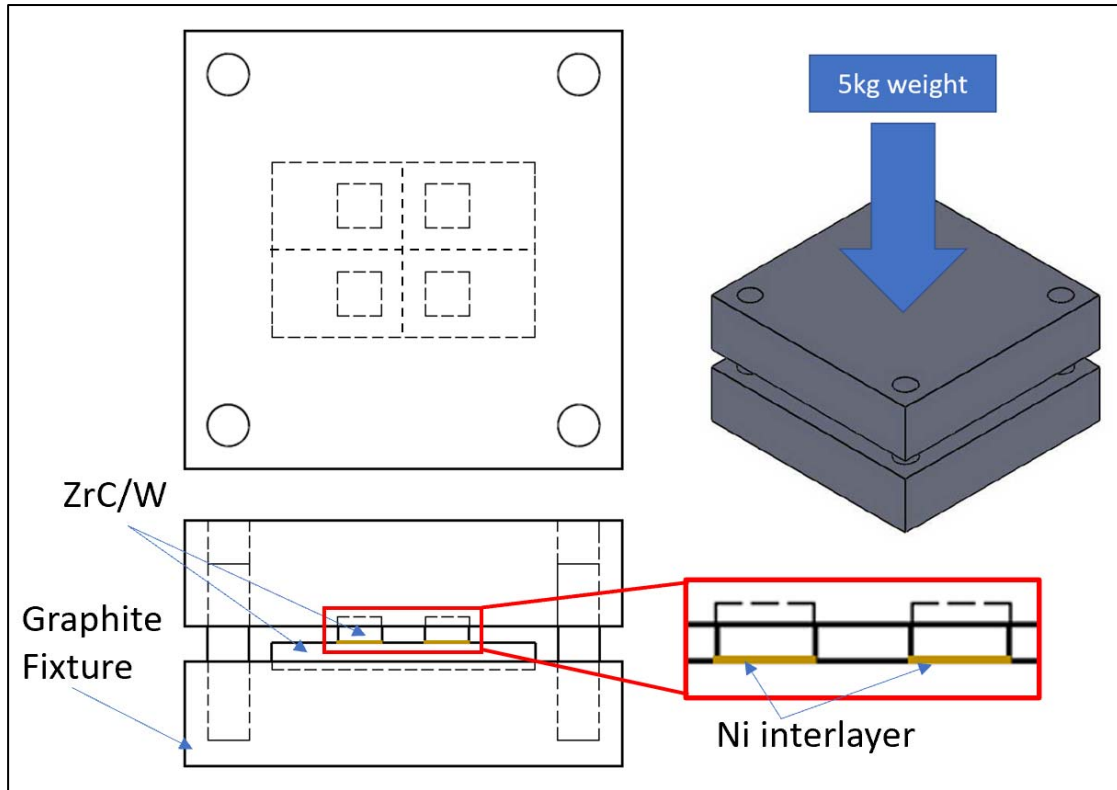


Figure 3.6. Assembly for bonding ZrC/W shear test specimen

The assembly as shown in Figure 3.6 was used for bonding ZrC/W to ZrC/W. The fixture was comprised of graphite (AR-14, Ohio Carbon Blank, Willoughby, OH, USA). Before an experiment, the fixture was coated with Boron Nitride Aerosol Lubriccoat (ZYP Coatings, Inc., Oak Ridge, TN, USA). Organic binders in the BN spray were removed by heating the coated fixture on a hot plate for 30 minutes at 200 °C. A 5-kg weight comprised of a sintered WC preform was placed on top of the fixture as shown in Figure 3.6. This weight provided a pressure of 0.5 MPa on the specimens. This low pressure was applied to the assembly in order to retain close contact between the bonding surfaces. The assembly was placed in a graphite furnace in an Ar atmosphere (UHP Argon 99.999% Purity, Airgas, USA). The assembly was heated to the bonding temperature at 15 °C/minute and held for 2 hours before cooling down at 15 °C/minute to about 400 °C, below which the furnace controller could not maintain the cooling rate. Three different bonding temperatures of 1300 °C, 1400 °C, and 1500 °C were used.

The bonded ZrC/W couple was cross-sectioned by a low-speed diamond saw (Techcut 4™ Precision Low Speed Saw, Allied High Tech Products, Inc., Rancho Dominguez, CA, USA) and

mechanically polished using diamond impregnated pads and diamond paste to a final finish of 1 μm . SEM-EDX (Quanta 3D FEG SEM, with X-ray analysis EDX Oxford Aztec Xstream-2 silicon drift detector) analyses were used to evaluate the distributions of elements from the bonded interface into the ZrC/W specimens.

The bonded specimens were used in compression shear tests, adapted from the work by Wang, et al., and Lei, et al. [67], [78], [79]. For these tests, the specimens were pre-loaded at 5 N, with a crosshead velocity of 0.5 mm/minute. The schematic drawing of the shear test assembly is shown in Figure 3.7. After the shear test, the fracture surfaces were investigated using SEM, and EDX analyses.

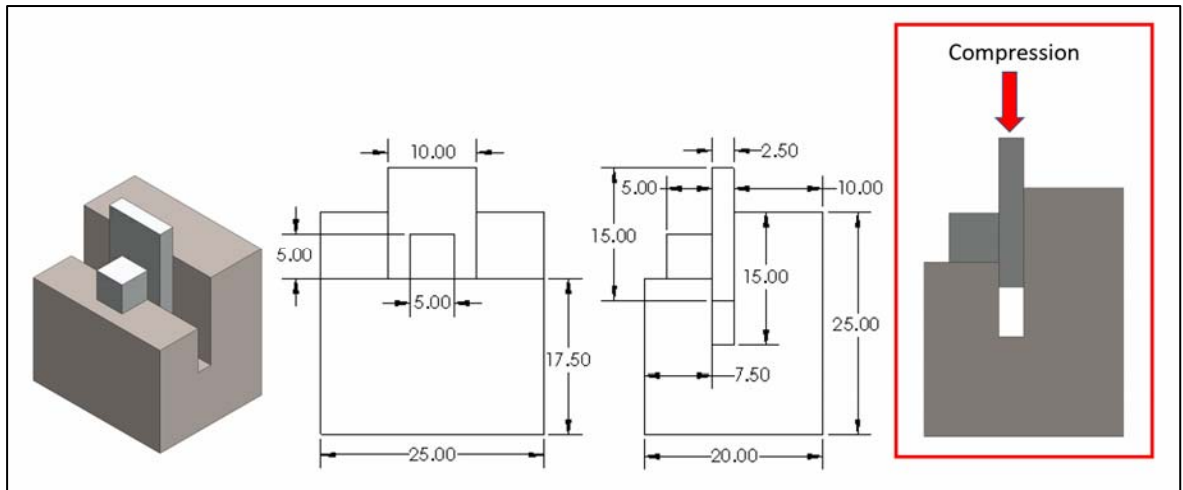


Figure 3.7. Schematic illustration of the shear test assembly used in this study

3.3.4 Wetting experiment

A DCP-derived ZrC/W-based composite was cut by EDM into plates with dimension of 5 mm x 5 mm x 1 mm. The plates were mechanically polished using diamond impregnated pads to a final finish of 9 μm . After polishing, the ZrC/W plates were etched in nitric acid (15.8 M) for 30 minutes. 25- μm -thick Ni foil (Alfa Aesar, Tewksbury, MA, USA, 99.7% Ni, 170 ppm C, 200 ppm Cu, 100 ppm Mg, 10 ppm S, 30 ppm Ti, 40 ppm Co, 200 ppm Fe, 1800 ppm Mn, 400 ppm Si) was cut into 4 mm x 4 mm pieces. The Ni foil and the polished ZrC/W specimens were ultrasonically cleaned in acetone for 10 minutes.

A ZrC/W plate with Ni foil on top was placed on an alumina plate and heated in a graphite furnace (Top loading graphite furnace, Oxy-Gon Industries Inc., Epsom, NH, USA) in an Argon atmosphere (UHP Argon 99.999% Purity, Airgas). The assembly was heated to 1400 °C at 15 °C/minute and held for 30 minutes before cooling at the same rate to about 400 °C, below which the furnace controller could not maintain this cooling rate. After the wetting experiments, the plates were investigated using SEM, and EDX analyses.

3.4 Results

3.4.1 Removal of residual Cu from the ZrC/W-based composite

Figure 3.8 provided top-view images of the same polished ZrC/W specimen before annealing, after annealing in Ar atmosphere at 1100 °C for 4 hours, and after etching in nitric acid (15.8 M) for 1 hour. As can be seen in Figure 3.8 b), several small Cu droplets (~0.5 – 1 mm diameter) were presented on surfaces of the annealed ZrC/W specimen. These Cu droplets were generated from residual Cu within the ZrC/W specimen.

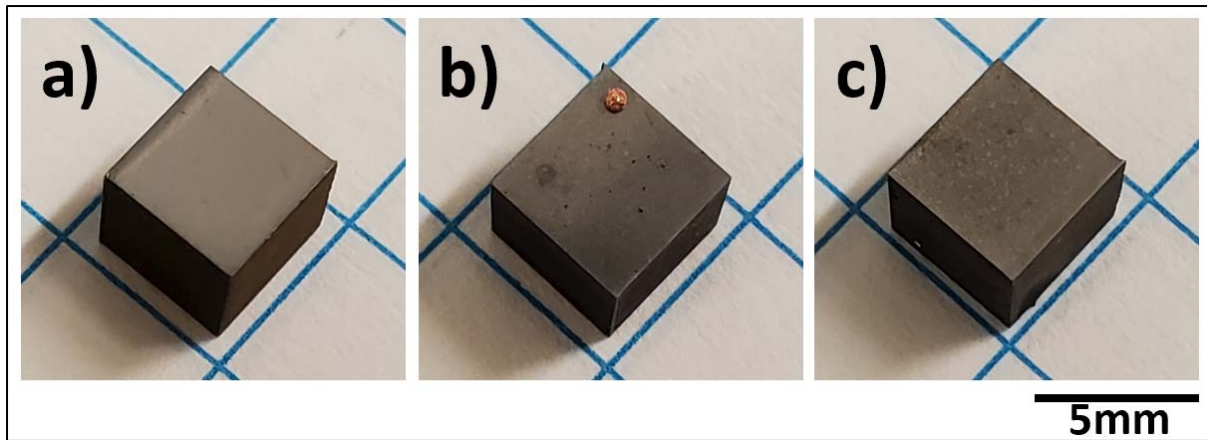


Figure 3.8. Photographs of a DCP-derived ZrC/W-based specimen: a) after polishing, b) after annealing in Ar atmosphere at 1100 °C for 4 hours, and c) after etching in nitric acid for 1 hour

Figure 3.9 shows a plot of the weight loss after specimen annealing and etching, as a function of annealing time at 1100 °C. The weight loss after etching resulted from the loss of residual Cu that migrated out to the external surfaces after annealing. By increasing annealing time, more residual Cu migrated out to the external surface, resulting in greater weight loss after etching.

After 16 hours at 1100 °C, no appreciable further increase in weight loss, due to Cu removal, was detected. The weight loss measurement for each annealing time was conducted on 2-4 specimens. Each point on the plot represents an average value of the weight loss for each annealing time. Error bars represent standard deviation of the measured average values. Appendix C2 provided weight loss values from all specimens.

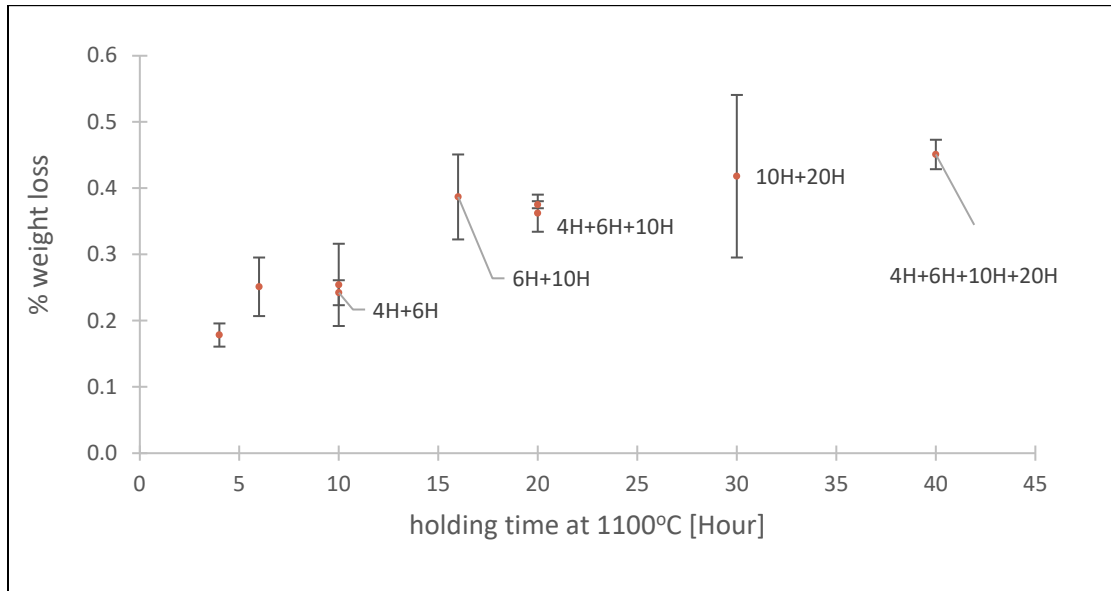


Figure 3.9. Weight loss of DCP-derived ZrC/W composite specimens as a function of annealing time at 1100 °C in Ar atmosphere.

To verify if the residual Cu still remained in the interior of the ZrC/W after annealing, the specimen annealed for 40 hours was cross-sectioned and SEM-EDX analyses were conducted in the middle portion of the cross-section. The SEM-EDX mapping, as shown Figure 3.10 a), indicated that residual Cu was not completely removed from the interior of the specimen. From such EDX mapping, one can see that a noticeable amount still remained inside the specimen.

Another SEM-EDX analysis was conducted at the edge of the cross-section, as shown in Figure 3.10 b). The elemental maps suggested that the Cu depletion zone of the annealed and etched ZrC/W was only about 50 μm from the external specimen surface.

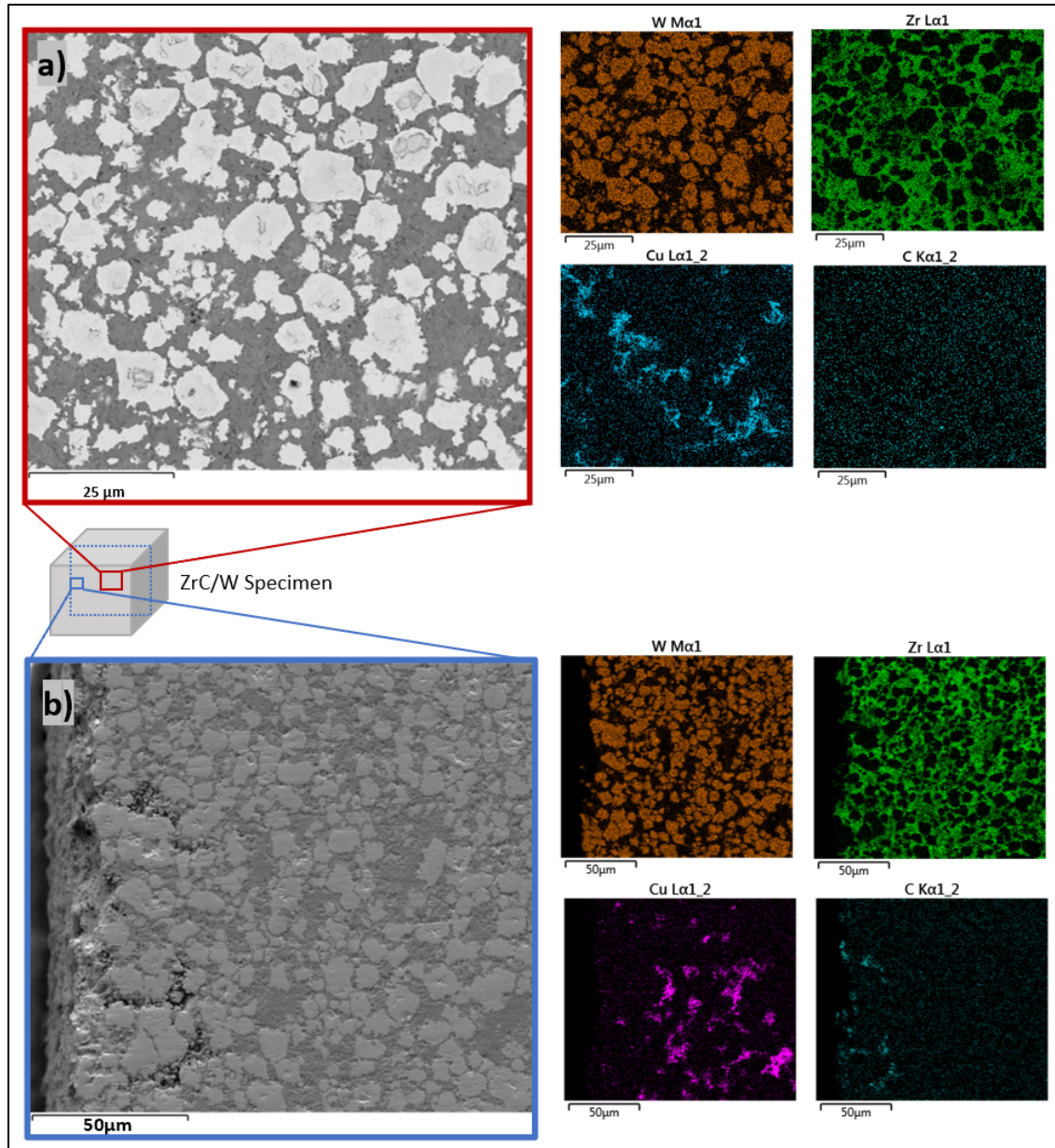


Figure 3.10. Elemental mapping of cross-section of a ZrC/W specimen annealed at 1100 °C for 40 hours after etching in nitric acid for 1 hour a) at the middle of the cross-section, b) at the edge of the cross-section

3.4.2 Microstructure of the bonded materials

Figure 3.11 a), b) and c) provide collages of BSE images of the polished cross-sections of entire interfaces of specimens bonded at 1300 °C, 1400 °C, and 1500 °C, respectively. The cross-section from a specimen bonded at 1300 °C exhibited several 25 – 90 μm voids, located at the red circles, while the cross-sections from the specimens bonded at higher temperature did not exhibit

such features. There was no appreciable difference in the microstructures at the bonded interfaces of the specimens joined at 1400 °C and 1500 °C.

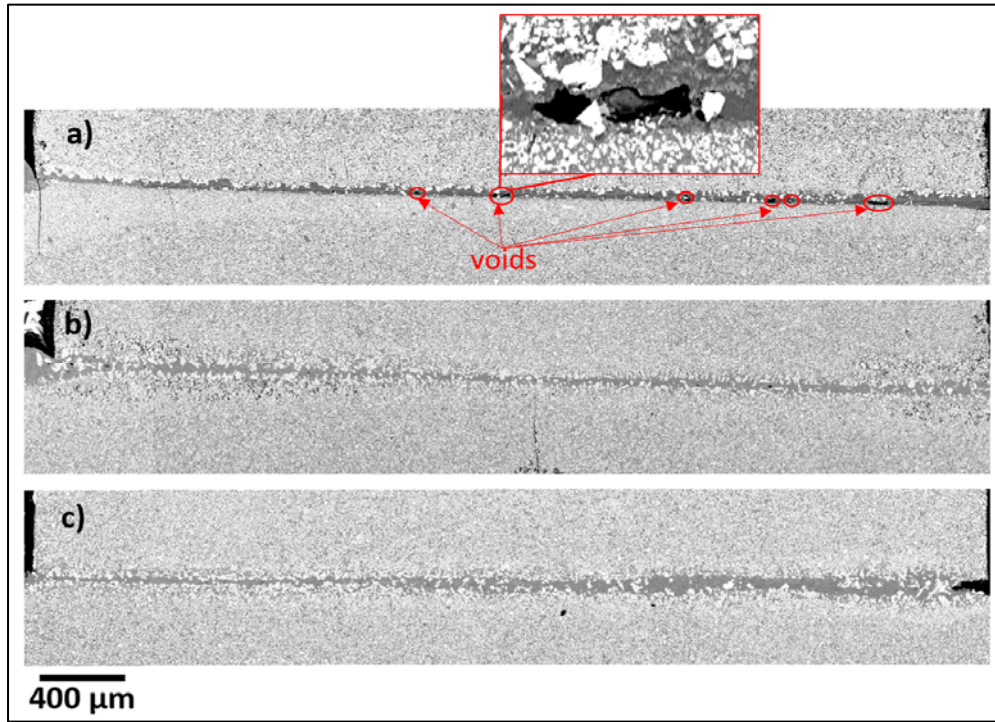


Figure 3.11. Collages of BSE images from ZrC/W specimen bonded at a) 1300 °C, b) 1400 °C, and c) 1500 °C

Figure 3.12 provides elemental distributions near the bonded interfaces of DCP-derived ZrC/W-based specimens. For all bonding conditions, residual Cu within the ZrC/W specimens migrated to the faying surfaces, while the Ni filler diffused into the ZrC/W specimens. From EDX mapping, there was no appreciable difference in the distributions of C, Cu, Ni, and W from the materials bonded at the three different temperatures. However, the mapping of Zr suggested a noticeable difference for the three bonding conditions. A noticeable Zr depletion zone remained at bonded interface for the specimen joined at 1300 °C. A Zr-free zone became less noticeable as the bonding temperature increased. At 1500 °C, the Zr map revealed significant migration of Zr into the interfacial zone.

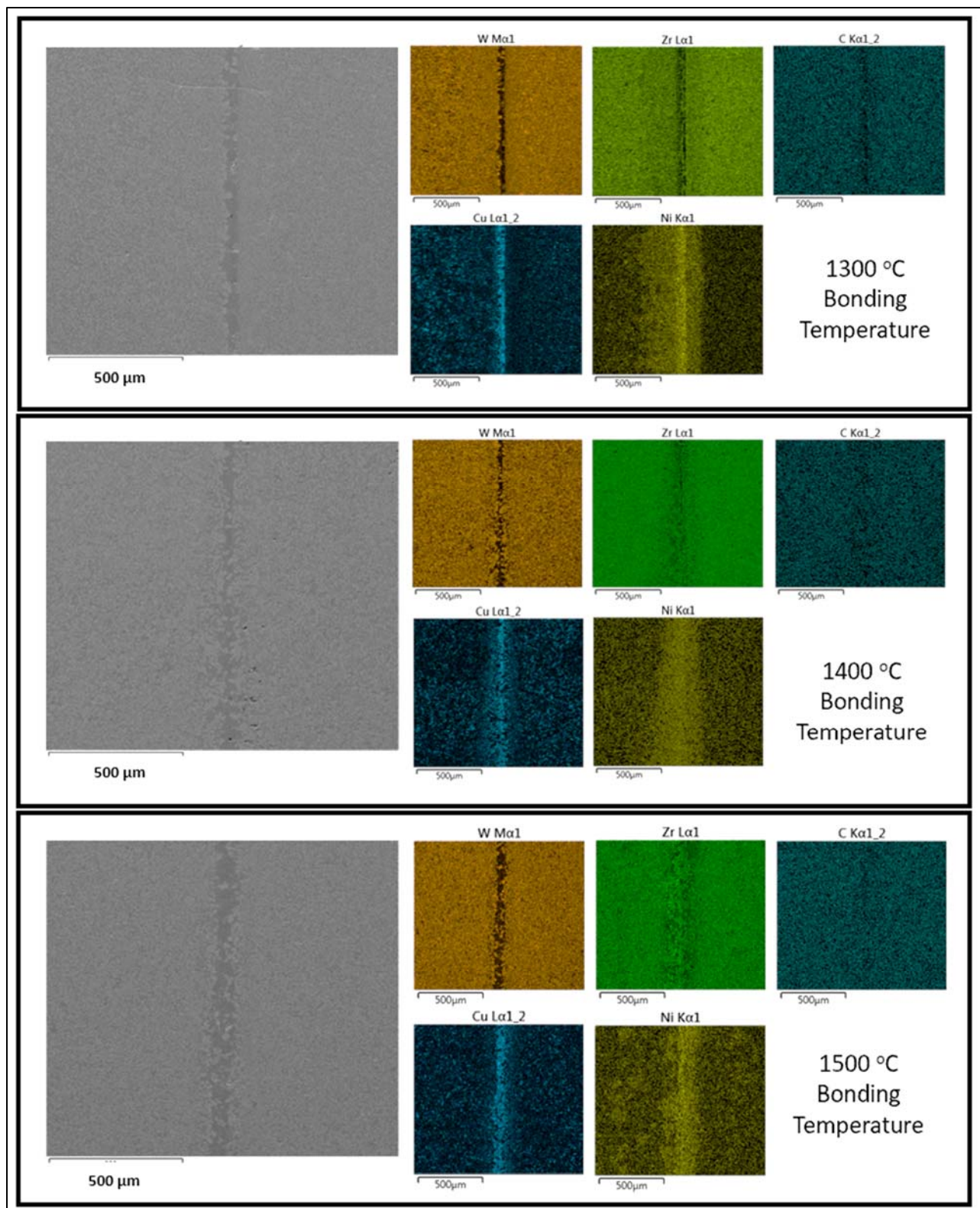


Figure 3.12. EDX elemental maps of polished cross-sections at the bonded interfaces from specimens joined at 1300 °C, 1400 °C, and 1500 °C

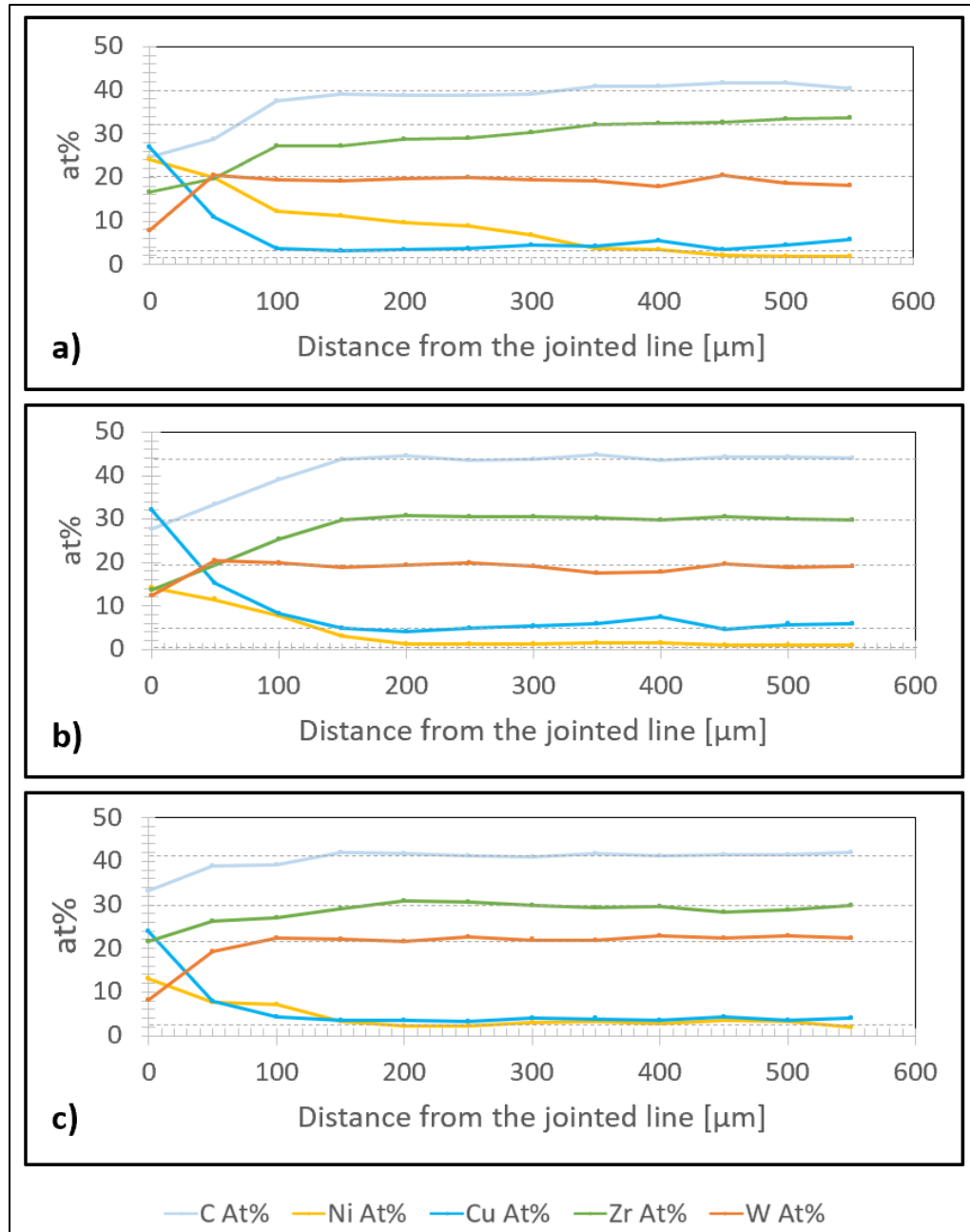


Figure 3.13. Distribution of elements away from the bonding interface from the specimen bonded at a) 1300°C for 2 hours, b) 1400°C for 2 hours, and c) 1500°C for 2 hours

Figure 3.13 provides the concentration profiles of elements away from the bonded interface for all bonding temperatures. Each composition data point on the y-axis was obtained from a semi-quantitative EDX analyses of spectra collected from an area of 50 μm x 575 μm . The designated

x = 0 coordinates on these plots are located the middle of the region containing the bonded interface. An illustration showing how the measurement was made is shown in Appendix C3.

The distribution of elements at bonded interfaces were slightly different for different bonding temperatures, as shown in Figure 3.12. Figure 3.14 provided a plot of chemical composition at the bonded interface from cross-sections of specimens bonded at different temperatures. Each atomic percent value on the y-axis was obtained from a semi-quantitative EDX analysis of spectra collected from an area of 50 μm x 575 μm containing the bonded interface. The measurement was conducted at 5 locations at the interface for each bonding condition and the average values were plotted with error bars representing standard deviation of the measured average values.

From the plot shown in Figure 3.14, the Zr, and C at bonded interface regions increased as the bonding temperature increased from 1400 °C to 1500 °C. This observation, and the observation from the wetting experiment suggested that as, the bonding temperature increased, more ZrC from the ZrC/W substrate migrated into liquid region at the seam area, so that upon cooling, ZrC crystals precipitated from the melt and resided at the seam area.

On the other hand, Ni at the bonded interface area decreased as the bonding temperature increased. Presumably the diffusion of liquid Ni into the ZrC/W specimen should be faster at the higher bonding temperature.

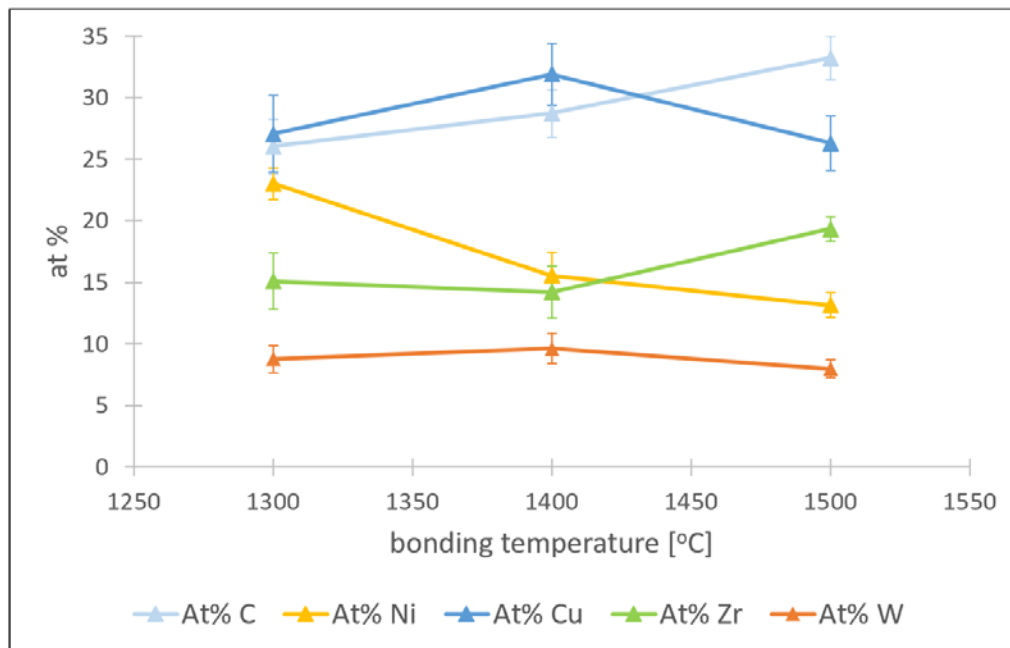


Figure 3.14. Compositions at the bonded interface regions for different bonding temperatures

3.4.3 Effect of bonding temperature on the mechanical behavior of bonded ZrC/W specimens

Figure 3.15 provides a plot of the average shear strength as a function of bonding temperature. The error bars on the y-axis represents one standard deviation from 6 measurements at each bonding condition. As can be seen, an average shear strength of the bonded ZrC/W was as high as 145.0 MPa at the bonding temperature of 1500 °C. This was about 40% of the reported average failure strength of DCP-derived ZrC/W-based composites measured by 4-point-bending from Caccia, et al. [8].

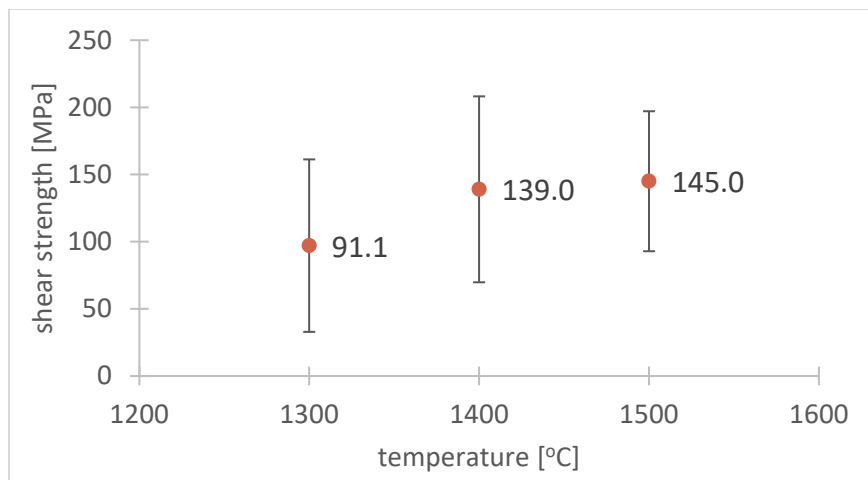


Figure 3.15. Effect of bonding temperature on the shear strength of the bonded ZrC/W specimens

SE images of fracture surfaces of the specimens after the shear test are shown in Figure 3.16. These images are collages of SE images collected from the debonded specimens that were bonded at 1400 °C for 2 hours. Two types of fracture surfaces were observed. The first type is shown in Figure 3.16 a). The relatively rough fracture surface was associated with fracture through the ZrC/W-based composite away from the bonded interface. The second type is shown in Figure 3.16 b). The fracture surface in this case was relatively smooth and was associated with fracture predominately along the bonded interface.

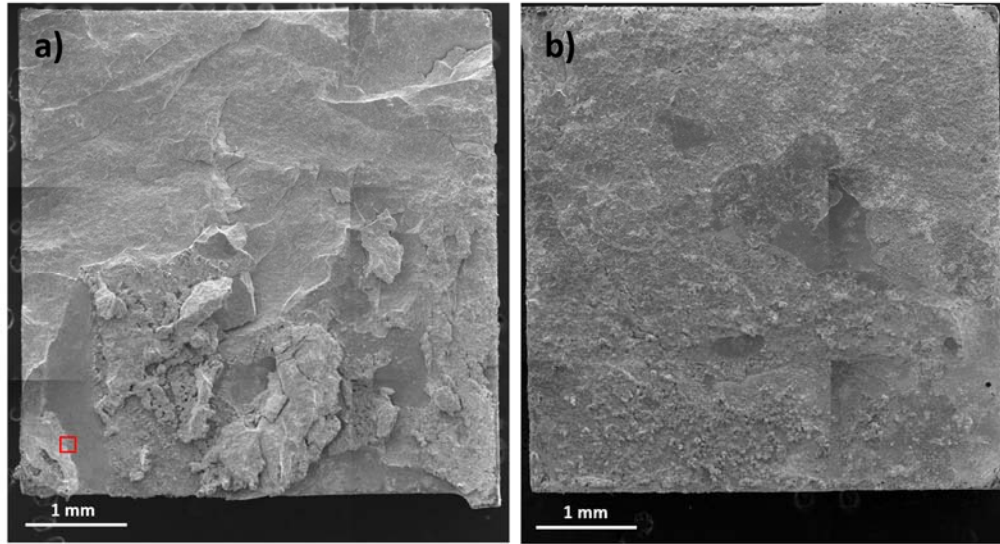


Figure 3.16. Collage of SE images from a fracture surface obtained from the specimens that were bonded at 1400 °C for 2 hours; a) a specimen that failed within ZrC/W-based composite, and b) a fracture surface from a specimen that fail at the bonded interface

Figure 3.17 provides a BSE image with EDX elemental maps from a fracture surface at a higher magnification located at the region indicated by a red square in Figure 3.16 a). Spot A was located at a darker (lower atomic number) region and was comprised largely of Cu with some Ni. From the Ni-Cu phase diagram [80] (Figure 3.18) at 1400 °C, Cu has a solubility of ~15 Ni at% in liquid Cu. Hence, this phase seems to be a solidified Cu-Ni phase. Spot B was located at a lighter (higher atomic number) region. EDX analysis of this spot was consistent with W. Spot C was also W-rich, along with some Ni. Spot D and E consisted of mostly Zr. The phase diagram of ZrC-Ni [77] indicated that ZrC-Ni compositions can melt at 1290 °C; therefore, spot D and E were consistent with the solidified molten ZrC with some Ni, Cu, and W solutes.

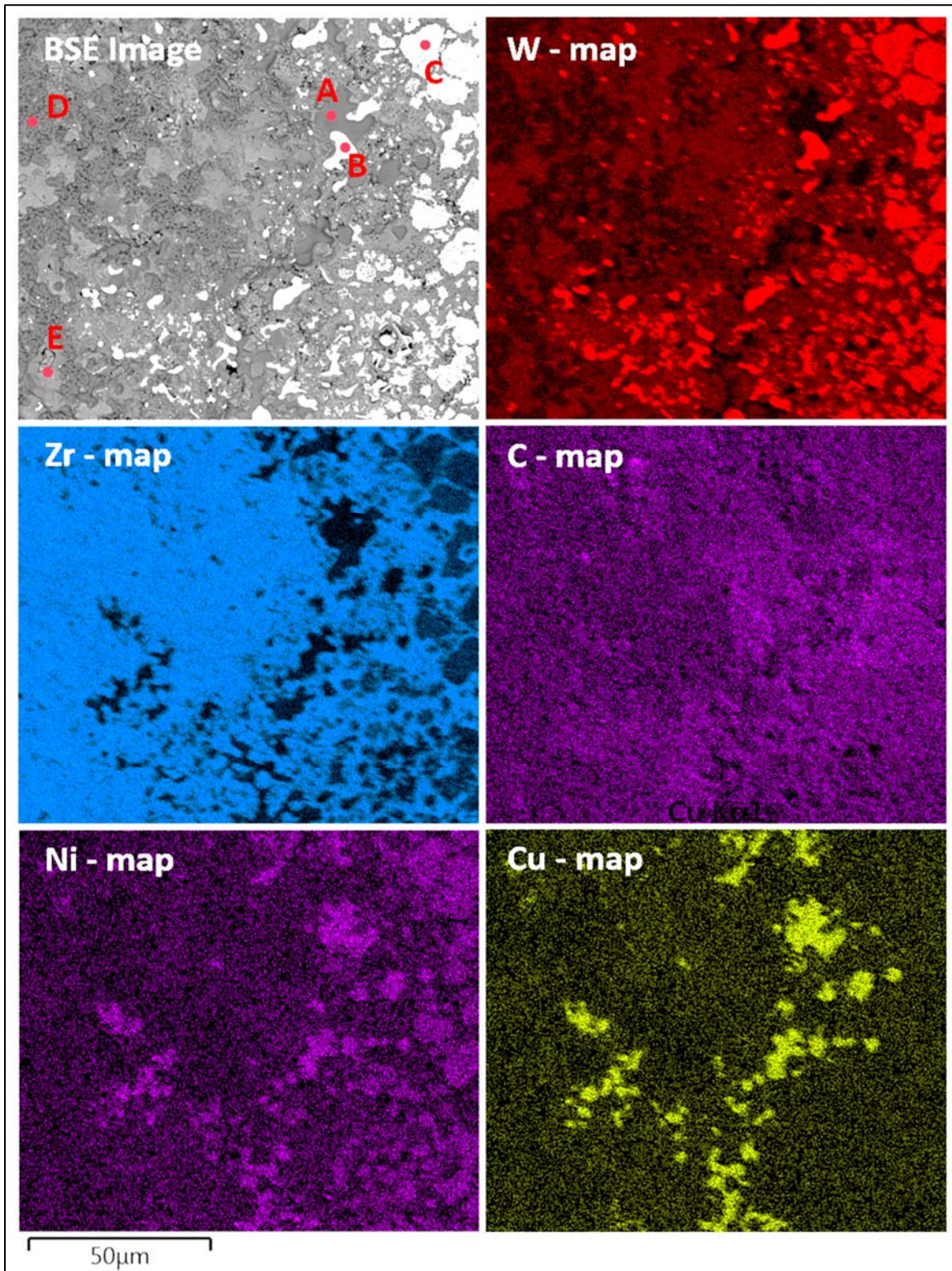


Figure 3.17. BSE image and EDX elemental maps of a fracture surface from the debonded ZrC/W at a high magnification

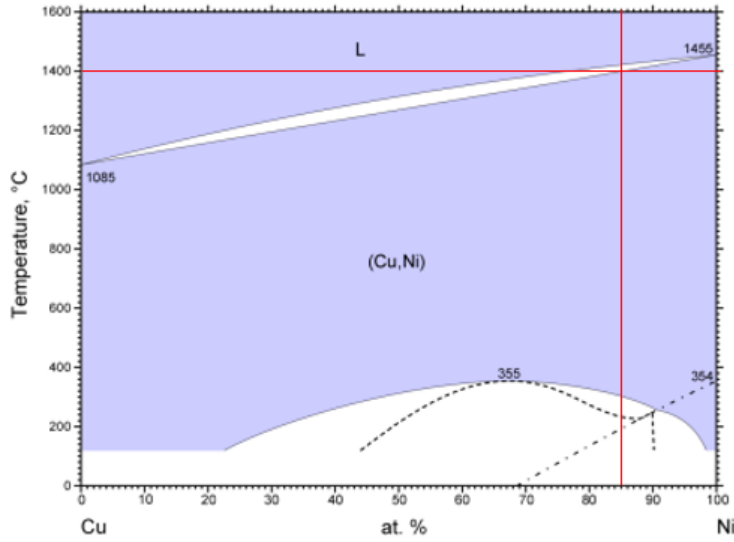


Figure 3.18. Ni-Cu phase diagram [80]

3.4.4 Wetting behavior of Ni on ZrC/W

Figure 3.19 provides a BSE image with EDX elemental maps showing how Ni foil interacted with a DCP-derived ZrC/W-based composite at 1400 °C for 30 minutes. The chemical composition of each indicated location, as measured by EDX analysis, is shown in Table 3.1. At spot C, EDX analysis detected mostly Zr and C and the morphology of this location appeared crystalline. At spot B, EDX analysis was consistent with a solidified Cu-Ni liquid. At spot A, EDX analysis yielded mostly W with small amount of Cu and consistent with W solid solution.

Table 3.1. Chemical composition (at%) and possible phase of each spot in Figure 3.19

spot	Ni	Cu	Zr	W	C	expected phase
A	3.5	2.0	-	94.5	-	W(s,s)
B	19.2	70.0	-	-	10.8	Cu (s,s)
C	-	0.1	24.1	2.9	72.9	ZrC

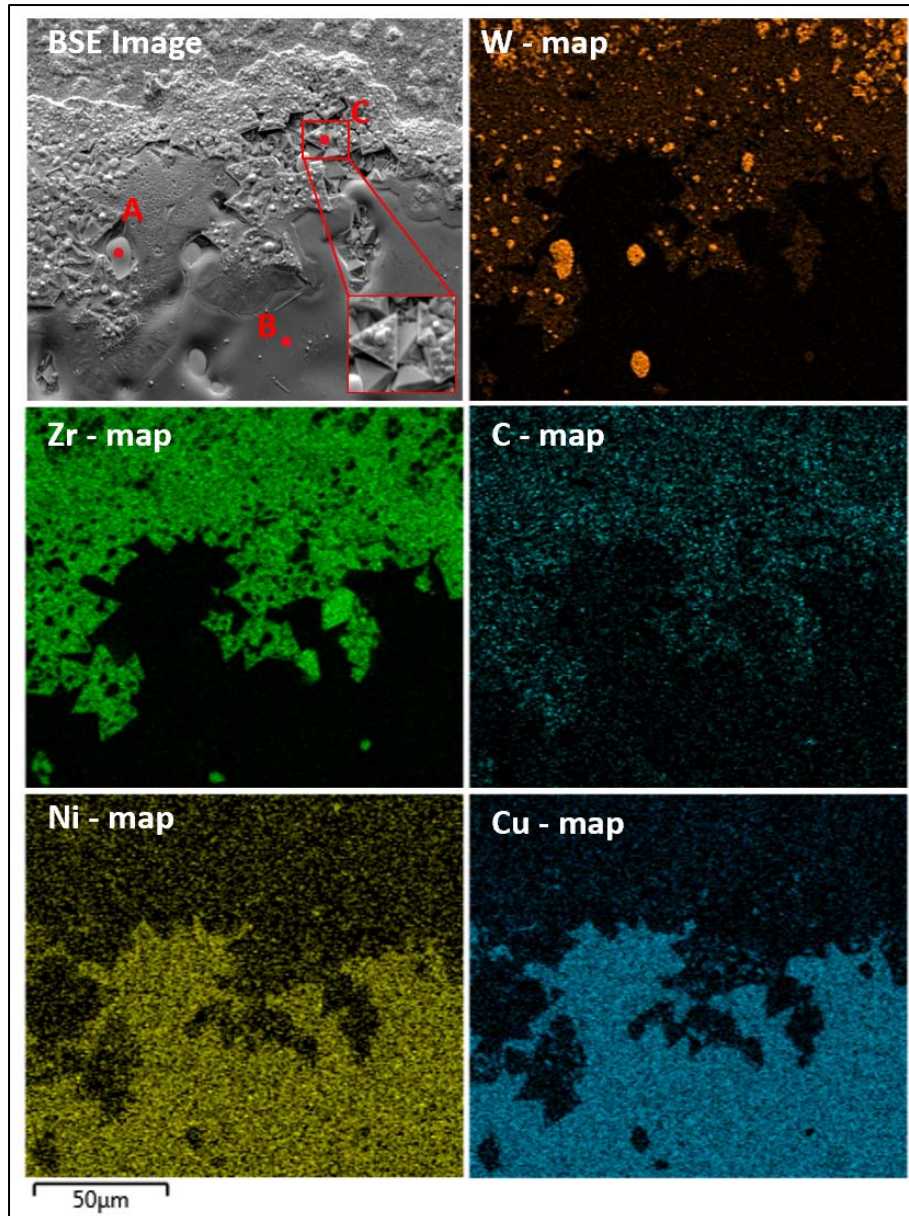


Figure 3.19. BSE image and EDX elemental maps of a top view of a ZrC/W specimen after exposure to Ni foil at 1400 °C for 30 minutes

The observations from the wetting experiment were consistent with the observations from the cross-sections of the bonded ZrC/W specimens. The higher magnification EDX map of bonded interface, as shown in Figure 3.20, shows the presence of Zr (green map) together with Ni and Cu. Particles of W in the bonded interface region were also detected.

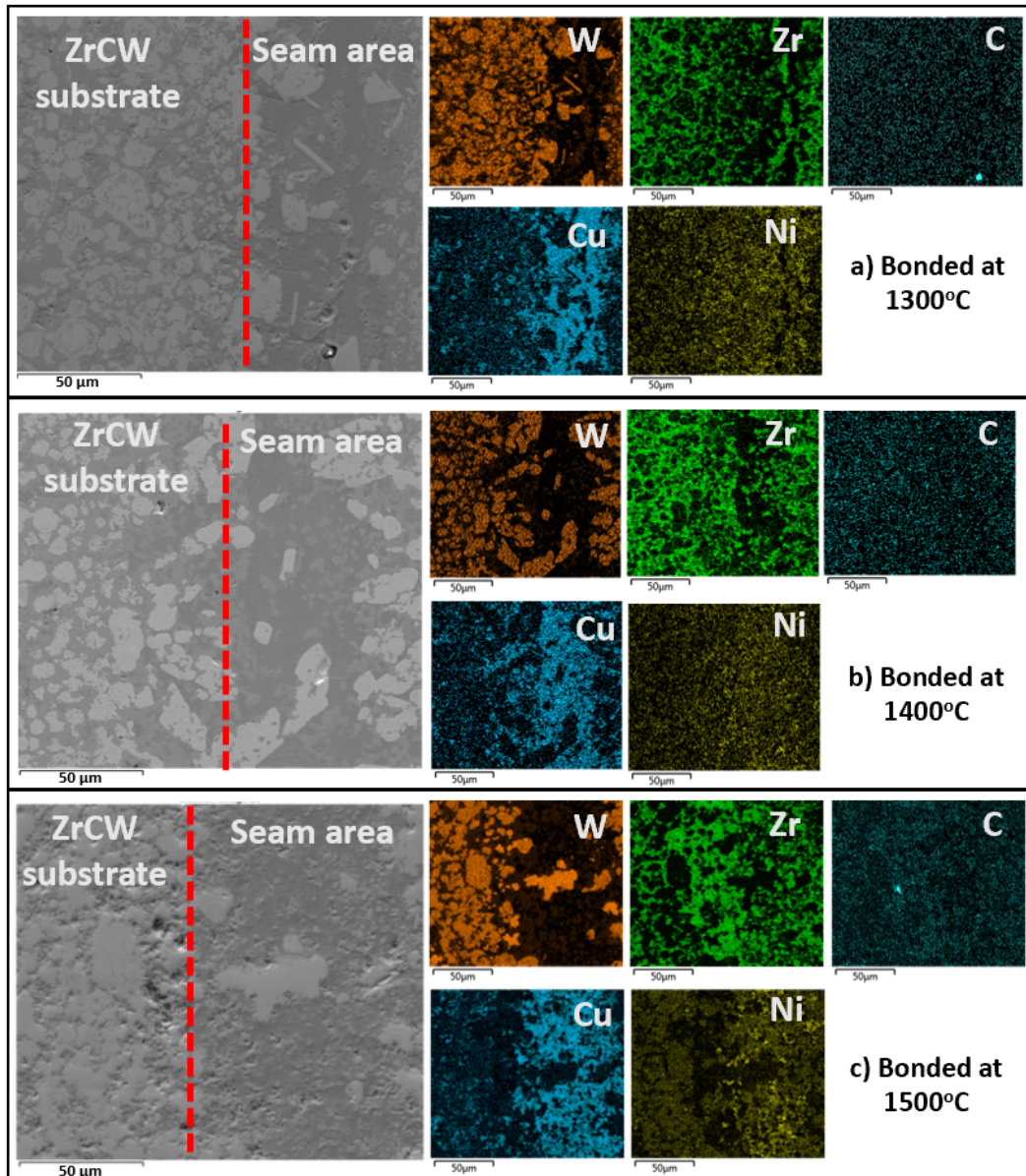


Figure 3.20. BSE image with EDX mapping of the bonded interface at higher magnification from a polished cross-section of a specimen bonded at a) 1300 °C for 2 hours, b) 1400 °C for 2 hours, and c) 1500 °C for 2 hours

3.5 Discussion

There are several parameters (including the bonding temperature, surface finish of the faying surfaces, interlayer materials, interlayer thickness, clamping force, holding time, heating rate, etc.) that can affect the bonding quality of the joint formed by liquid phase bonding [73], [74], [76]. For this initial study, only the effects of bonding temperature were investigated. Bonding temperatures

of 1300 °C, 1400 °C, and 1500 °C were chosen. The lower bound was chosen to be 1300 °C as the ZrC-Ni phase diagram indicates that liquid phase can start forming at 1290 °C [77]. From the Ni-W-Cu phase diagram [81], liquid phase formation starts at 1300°C, with the liquid region become larger as temperature further increases. The upper bound was chosen to be 1500 °C because the phase diagram of Ni-W [32], [82] indicates a liquid phase in the Ni-rich region.

In section 3.3.3, the average values of shear strength collected from 6 specimens for each bonding temperature exhibited large standard deviations. The difference between data for each bonding temperature was evaluated using the student’s t-test. As shown in Table 3.2 the differences in the shear strength for each bonding temperature were not significant at a 95% confidence level since the p-values for each comparison were greater than 0.05.

Table 3.2. Student’s t-test analyses of difference in the shear strength data for different bonding temperatures

Two Sample t-test	1300°C VS 1400°C		1300°C VS 1500°C		1400°C VS 1500°C	
	1300°C	1400°C	1300°C	1500°C	1400°C	1500°C
Average shear strength: M_i	97.05	138.98	97.05	145.03	138.98	145.03
Standard deviation of samples	64.2	69.23	64.21	52.13	69.23	52.13
Number of sample	6	6	6	6	6	6
SE of sampling distribution	38.55		33.76		35.38	
Degree of freedom	9.94		9.59		9.29	
Null Hypothesis : H_0	$M_{1300} - M_{1400} = 0$		$M_{1300} - M_{1500} = 0$		$M_{1400} - M_{1500} = 0$	
Alternate Hypothesis: H_a	$M_{1300} - M_{1400} \neq 0$		$M_{1300} - M_{1500} \neq 0$		$M_{1400} - M_{1500} \neq 0$	
t score	-1.09		-1.42		-0.17	
P-value (2-sided hypothesis test)	0.30	>0.05	0.19	>0.05	0.87	>0.05
	Cannot reject H_0		Cannot reject H_0		Cannot reject H_0	

Based on these analyses, the bonding evolution of the ZrC/W-Ni-ZrC/W specimens can be described in these following steps. First, upon heating to the bonding temperature, residual Cu from the ZrC/W substrate starts moving to the faying surfaces, and at the same time the Ni

interlayer starts melting. The residual Cu can help as a melting point depressant (MDP) for the joining process. In addition, W and ZrC from the faying surfaces of the substrates start dissolving into the molten interlayer. Next, during the holding period, some Ni in the molten interlayer starts to diffuse into the ZrC/W substrate. Upon cooling, the remaining Ni, Cu melt solidifies. The solubility of W in the melt also decreases as temperature decreases, so that several W islands are separately solidified at the bonded interface. At the same time, recrystallization of ZrC from the melt can also occur.

3.6 Conclusion

- ZrC/W-based composites can be joined by liquid phase bonding using a Ni interlayer. The residual Cu in the ZrC/W migrated to the faying surface to lower the melting point allowing liquid phase bonding to occur at ≥ 1300 °C.
- Different bonding temperatures in the range of 1300 °C to 1500 °C, did not result in a significant difference in the bonding strength at room temperature. The highest average shear strength of 145.0 MPa, was observed for the specimens bonded at the 1500 °C, although the measured values were not statistically different from the values of the other bonding temperatures.
- Two types of fracture surfaces were observed from the debonded specimens after the shear testing; i) relatively smooth fracture surfaces associated with failure at the interface, ii) rougher fracture surface associated with failure through the ZrC/W composite.

APPENDIX A. SUPPLEMENTARY MATERIALS FOR CHAPTER 1: INTERDIFFUSION STUDY BETWEEN NICKEL CHROMIUM ALLOY AND TUNGSTEN IN THE 1000 °C-1200°C TEMPERATURE RANGE

A1. \bar{L}_3 measurement from micrographs of the arc-melted 80Ni20Cr alloy, and the commercial W-plate

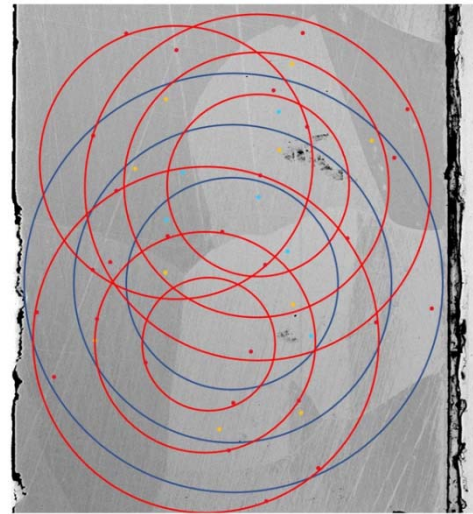
The micrograph was used to determine \bar{L}_3 (mean intercept length of three-dimensional bodies) which represents average grain size of the specimen [34]. The \bar{L}_3 measurement was conducted, following standardize method suggested in ASTM E1382-97 [35], by placing random circles on the micrograph and counting number of grains intercepted by perimeter of the circles

$$(N_i) \cdot \bar{L}_3 = \frac{1}{N_L} = \frac{L_i}{N_i}$$

- **Micrograph of the 80Ni20Cr alloy**

Conversion 1.08=200 μ m

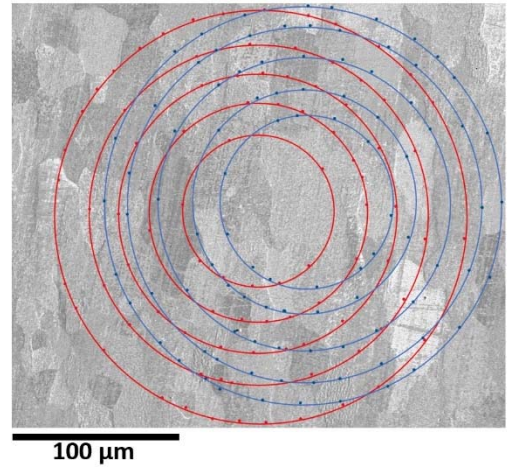
Circle#	Grid diameter	Perimeter L_i [μ m]	N_i	N_{Li}	\bar{L}_3 [μ m]
1	3.95	2298	6	2.61E-03	383.0
2	3.00	1745	5	2.86E-03	349.1
3	2.00	1164	4	3.44E-03	290.9
4	3.27	1902	5	2.63E-03	380.5
5	2.50	1454	5	3.44E-03	290.9
6	1.72	1001	3	3.00E-03	333.6
7	3.27	1902	6	3.15E-03	317.1
8	2.08	1210	5	4.13E-03	242.0
9	1.26	733	2	2.73E-03	366.5
10	2.58	1501	4	2.66E-03	375.2
Average from 10 circle grid placements					332.9
Standard deviation					47.1



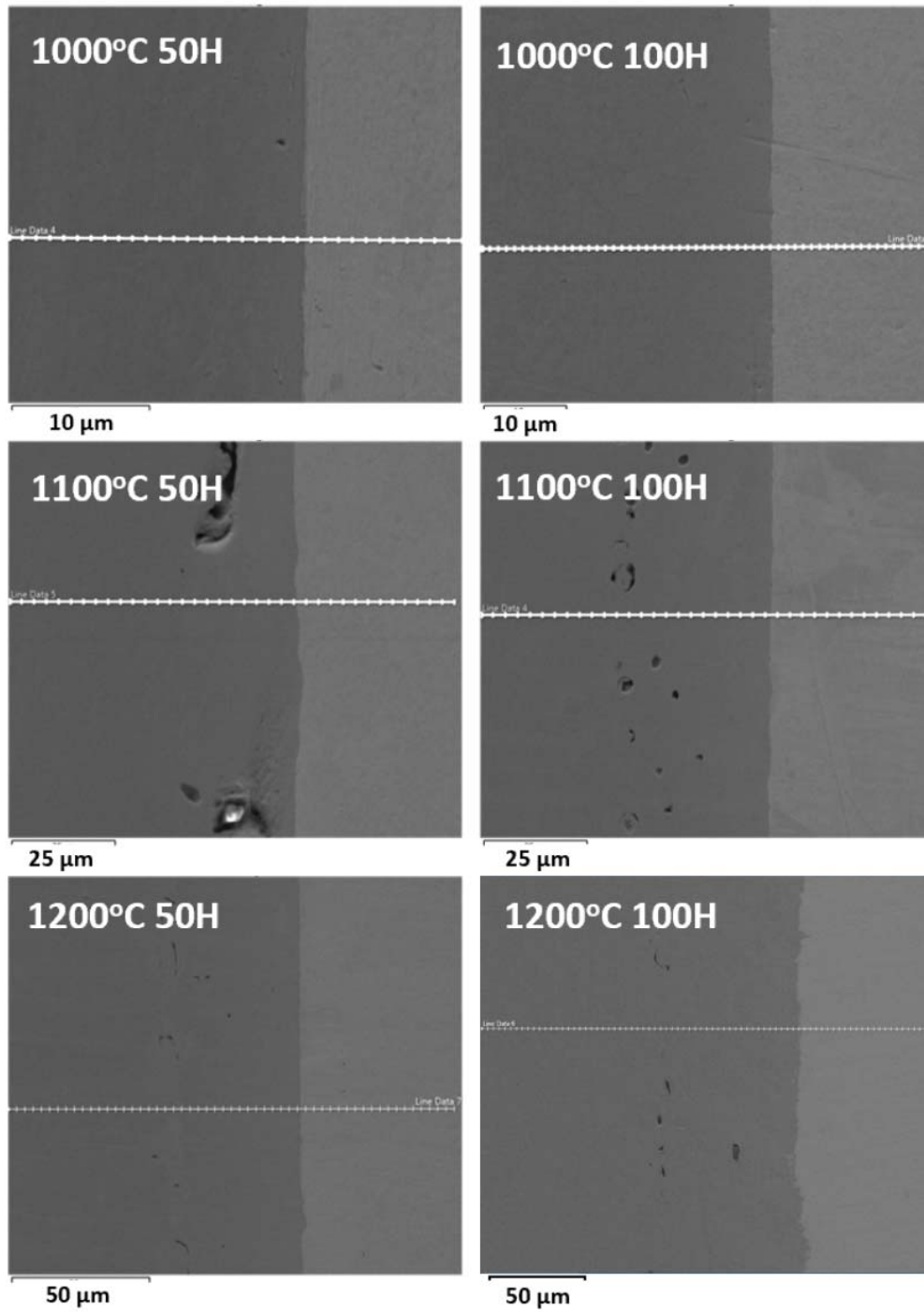
- **Micrograph of the commercial W-plate**

Conversion 2.14=100 μ m

Circle#	Grid diameter	Perimeter L_i [μ m]	N_i	N_{Li}	\bar{L}_3 [μ m]
1	5.33	782	28	3.58E-02	27.9
2	4.39	644	19	2.95E-02	33.9
3	3.60	528	19	3.60E-02	27.8
4	2.82	414	16	3.86E-02	25.9
5	1.96	288	8	2.78E-02	36.0
6	5.14	755	26	3.45E-02	29.0
7	4.58	672	23	3.42E-02	29.2
8	3.78	555	19	3.42E-02	29.2
9	2.89	424	16	3.77E-02	26.5
10	2.24	329	12	3.65E-02	27.4
Average from 10 circle grid placements					29.3
Standard deviation					3.2



A2. The SE images of the diffusion couples from all experimental condition



A3. Concentration profile data from all diffusion couples as measured by quantitative EDX analyses

Note that the locations with * are the locations of interfaces, and the compositions at the interface are interpolated values.

1000°C, 50 hours			
Distance [μm]	atomic fraction		
	W	Cr	Ni
0	0.00	0.22	0.78
1	0.00	0.24	0.75
2	0.01	0.22	0.77
3	0.01	0.24	0.75
4	0.02	0.23	0.75
5	0.02	0.23	0.76
6	0.03	0.21	0.76
7	0.03	0.21	0.76
8	0.07	0.20	0.73
9	0.08	0.20	0.72
10	0.10	0.19	0.71
11	0.13	0.18	0.69
12	0.16	0.16	0.68
13	0.20	0.14	0.65
14	0.24	0.13	0.63
14.5*	0.26	0.12	0.62
14.5*	0.97	0.01	0.02
15	0.97	0.01	0.02
16	0.98	0.00	0.01
17	0.99	0.00	0.01
18	0.98	0.00	0.01
19	1.00	0.00	0.00

1000°C, 100 hours			
Distance [μm]	atomic fraction		
	W	Cr	Ni
0	0.00	0.22	0.78
1	0.01	0.22	0.77
2	0.01	0.23	0.76
3	0.01	0.21	0.78
4	0.02	0.22	0.76
5	0.02	0.23	0.75
6	0.02	0.22	0.76
7	0.03	0.23	0.74
8	0.03	0.21	0.76
9	0.06	0.21	0.73
10	0.05	0.20	0.75
11	0.06	0.20	0.73
12	0.07	0.20	0.73
13	0.10	0.19	0.71
14	0.12	0.20	0.68
15	0.12	0.17	0.71
16	0.14	0.17	0.69
17	0.17	0.16	0.67
18	0.19	0.16	0.65
19	0.21	0.13	0.65
20	0.25	0.12	0.62
21*	0.28	0.11	0.61
21*	0.97	0.01	0.02
22	0.98	0.00	0.01
23	0.98	0.00	0.01
24	0.99	0.00	0.01
25	0.99	0.00	0.01
26	1.00	0.00	0.00

1100°C, 50 hours			
Distance [μm]	atomic fraction		
	W	Cr	Ni
0	0.00	0.23	0.77
3	0.01	0.22	0.77
6	0.01	0.23	0.76
9	0.00	0.23	0.77
12	0.01	0.22	0.77
15	0.01	0.23	0.76
18	0.02	0.22	0.76
21	0.02	0.23	0.74
24	0.03	0.22	0.75
27	0.04	0.21	0.75
30	0.06	0.21	0.73
33	0.08	0.21	0.71
36	0.10	0.19	0.71
39	0.11	0.19	0.70
42	0.14	0.18	0.68
45	0.18	0.17	0.66
48	0.19	0.17	0.64
51	0.22	0.15	0.64
54	0.25	0.13	0.62
56*	0.26	0.12	0.62
56*	0.98	0.01	0.01
57	0.98	0.01	0.01
60	0.98	0.01	0.01
63	0.99	0.00	0.00
66	1.00	0.00	0.00

1100°C, 100 hours			
Distance [μm]	atomic fraction		
	W	Cr	Ni
0	0.00	0.22	0.78
3	0.02	0.23	0.76
6	0.00	0.22	0.78
9	0.01	0.23	0.76
12	0.02	0.22	0.76
15	0.02	0.24	0.74
18	0.03	0.21	0.76
21	0.04	0.21	0.75
24	0.04	0.22	0.74
27	0.06	0.22	0.73
30	0.06	0.21	0.72
33	0.08	0.21	0.70
36	0.10	0.20	0.70
39	0.13	0.19	0.69
42	0.14	0.17	0.70
45	0.17	0.16	0.67
48	0.18	0.17	0.65
51	0.19	0.16	0.65
54	0.21	0.14	0.65
57	0.23	0.13	0.64
60	0.27	0.12	0.61
61*	0.26	0.12	0.62
61*	0.98	0.01	0.01
63	0.98	0.01	0.01
66	0.99	0.00	0.00
69	0.99	0.00	0.01
72	0.99	0.01	0.00
75	0.99	0.00	0.01
78	0.99	0.00	0.01
81	1.00	0.00	0.00

1200°C, 50 hours			
Distance [μm]	atomic fraction		
	W	Cr	Ni
0	0.00	0.22	0.78
3	0.02	0.22	0.77
6	0.00	0.22	0.78
9	0.01	0.22	0.77
12	0.01	0.22	0.76
15	0.02	0.21	0.77
18	0.02	0.21	0.76
21	0.02	0.21	0.76
24	0.03	0.21	0.76
27	0.03	0.23	0.74
30	0.04	0.20	0.76
33	0.04	0.22	0.74
36	0.04	0.21	0.75
39	0.05	0.22	0.74
42	0.05	0.22	0.73
45	0.06	0.20	0.74
48	0.07	0.21	0.72
51	0.07	0.19	0.74
54	0.08	0.20	0.73
57	0.08	0.19	0.73
60	0.10	0.19	0.71
63	0.10	0.19	0.71
66	0.10	0.18	0.72
69	0.12	0.19	0.69
72	0.14	0.17	0.69
75	0.17	0.17	0.67
78	0.17	0.17	0.66
81	0.18	0.16	0.66
84	0.20	0.15	0.65
87	0.21	0.15	0.65
90	0.22	0.16	0.62
93	0.24	0.14	0.62
96	0.25	0.13	0.62
99	0.27	0.12	0.61
101*	0.28	0.12	0.60
101*	0.98	0.01	0.01
102	0.98	0.01	0.01
105	0.99	0.01	0.00
108	0.99	0.00	0.01
111	1.00	0.00	0.00
114	0.99	0.00	0.00

1200°C, 100 hours			
Distance [μm]	atomic fraction		
	W	Cr	Ni
0	0.00	0.22	0.78
3	0.00	0.21	0.79
6	0.01	0.20	0.79
9	0.00	0.21	0.79
12	0.01	0.21	0.79
15	0.00	0.21	0.79
18	0.01	0.20	0.79
21	0.01	0.20	0.79
24	0.01	0.19	0.80
27	0.01	0.22	0.77
30	0.01	0.21	0.78
33	0.01	0.21	0.78
36	0.01	0.20	0.79
39	0.01	0.21	0.78
42	0.02	0.21	0.78
45	0.01	0.21	0.77
48	0.02	0.20	0.78
51	0.02	0.20	0.78
54	0.01	0.20	0.79
57	0.03	0.20	0.78
60	0.02	0.20	0.77
63	0.02	0.20	0.77
66	0.03	0.21	0.76
69	0.03	0.20	0.77
72	0.04	0.20	0.76
75	0.04	0.20	0.76
78	0.05	0.19	0.76
81	0.05	0.20	0.75
84	0.05	0.20	0.75
87	0.06	0.20	0.74
90	0.06	0.19	0.76
93	0.06	0.19	0.75
96	0.08	0.19	0.73
99	0.09	0.18	0.73
102	0.10	0.18	0.72
105	0.10	0.18	0.72
108	0.12	0.18	0.70
111	0.11	0.17	0.72
114	0.12	0.17	0.71
117	0.12	0.17	0.71
120	0.13	0.17	0.71

1200°C, 50 hours (continue)			
Distance [μm]	atomic fraction		
	W	Cr	Ni
117	0.98	0.01	0.01
120	0.99	0.00	0.01
123	1.00	0.00	0.00

1200°C, 50 hours (continue)			
Distance [μm]	atomic fraction		
	W	Cr	Ni
123	0.14	0.17	0.69
126	0.14	0.16	0.70
129	0.15	0.16	0.69
132	0.16	0.15	0.68
135	0.17	0.15	0.68
138	0.19	0.15	0.66
141	0.19	0.14	0.67
144	0.20	0.14	0.66
147	0.21	0.14	0.65
150	0.23	0.14	0.63
153	0.23	0.13	0.64
156	0.24	0.12	0.64
159	0.27	0.12	0.61
162	0.27	0.11	0.62
165*	0.28	0.12	0.60
165*	0.98	0.01	0.01
168	0.97	0.01	0.02
171	0.99	0.00	0.01
174	0.99	0.01	0.00
177	0.99	0.01	0.00
180	0.99	0.01	0.00
183	0.99	0.01	0.00
186	1.00	0.00	0.00
189	1.00	0.00	0.00

APPENDIX B. SUPPLEMENTARY MATERIALS FOR CHAPTER 2: EFFECT OF GRAIN SIZE OF TUNGSTEN ON THE INTERDIFFUSION OF NICKEL CHROMIUM ALLOY/ TUNGSTEN DIFFUSION COUPLES

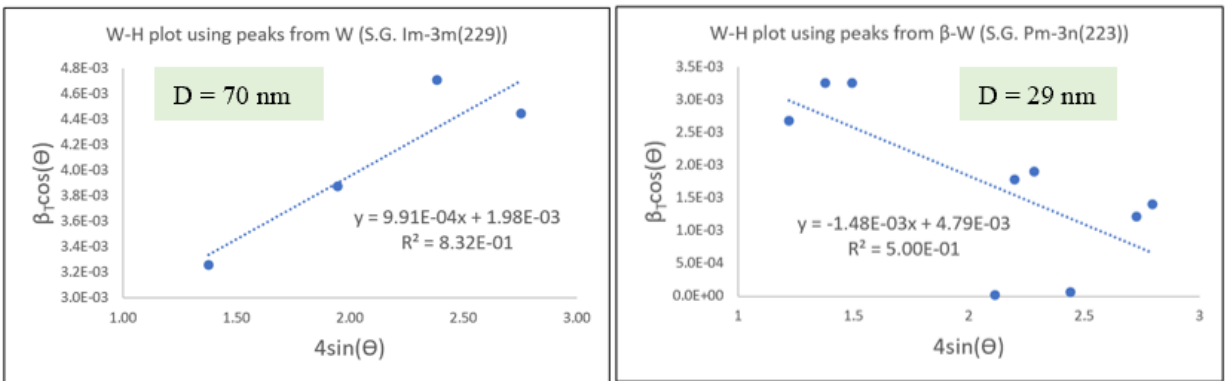
B1. Determination of crystalline size of as-received W powders on the basis of Williamson-Hall Method

Characteristic peaks from X-ray diffraction patterns can be broaden due to variation of crystalline size in the powder specimen, and inhomogeneous strain following this expression [54].

$$\beta_T \cos\theta = \varepsilon(4\sin\theta) + \frac{K\lambda}{D}$$

Where β_T represents total broadening due to effect of strain, ε , and effect of crystalline size D . θ represent location of the corresponding X-ray diffraction peak and has unit in radian. K is a constant = 0.9, and λ is wavelength of the X-ray used for the analyses, which is 0.15406 nm for this study. By plotting $\beta_T \cos\theta$ as a function of $4\sin\theta$ (W-H plot), crystalline size, D , can be determined by y-intercept of the linear fitted line.

Since the X-ray patterns obtained from the as-received nano W powder consisted of characteristic peaks from both W (space group Im-3m(229)), and β -W (space group Pm-3n(223)), two W-H plots for each space group were generated and the crystalline size were determine from each plot as shown below.



B2. \bar{L}_3 measurement from micrographs of the fine grain tungsten and large grain tungsten

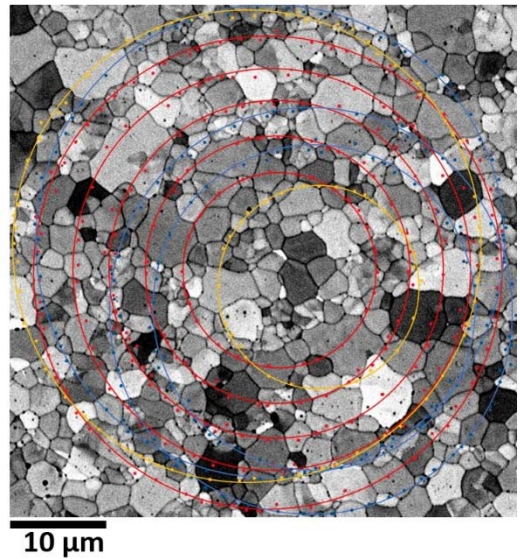
The micrograph was used to determine \bar{L}_3 (mean intercept length of three-dimensional bodies) which represents average grain size of the specimen [34]. The \bar{L}_3 measurement was conducted, following standardize method suggested in ASTM E1382-97 [35], by placing random circles on the micrograph and counting number of grains intercepted by perimeter of the circles (N_i).

$$\bar{L}_3 = \frac{1}{N_L} = \frac{L_i}{N_i}$$

- **Micrograph from a thermal etched polished cross-section from FGW_HP1500C**

Conversion 1.13=10 μ m

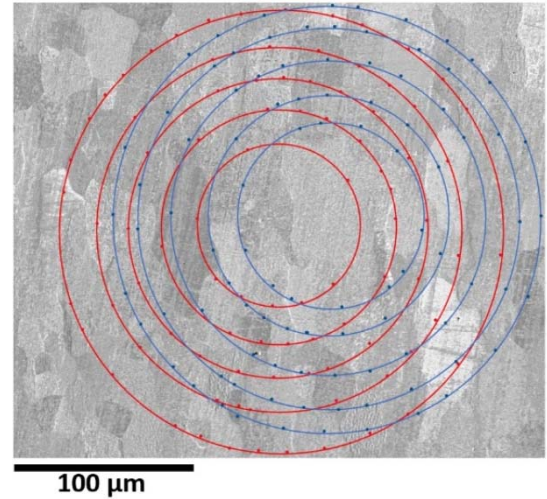
Circle#	Grid diameter	Perimeter L_i [μ m]	N_i	N_{Li}	\bar{L}_3 [μ m]
1	5.55	154	64	4.15E-01	2.4
2	4.71	131	52	3.97E-01	2.5
3	3.97	110	50	4.53E-01	2.2
4	3.14	87	40	4.58E-01	2.2
5	2.29	64	26	4.08E-01	2.4
6	5.55	154	68	4.41E-01	2.3
7	4.78	133	64	4.82E-01	2.1
8	3.82	106	50	4.71E-01	2.1
9	5.55	154	66	4.28E-01	2.3
10	2.39	66	29	4.36E-01	2.3
Average from 10 circle grid placements					2.3
Standard deviation					0.1



- **Micrograph from an etched polished cross-section of the LGW plate (99.95% purity, Midwest Tungsten Inc., USA)**

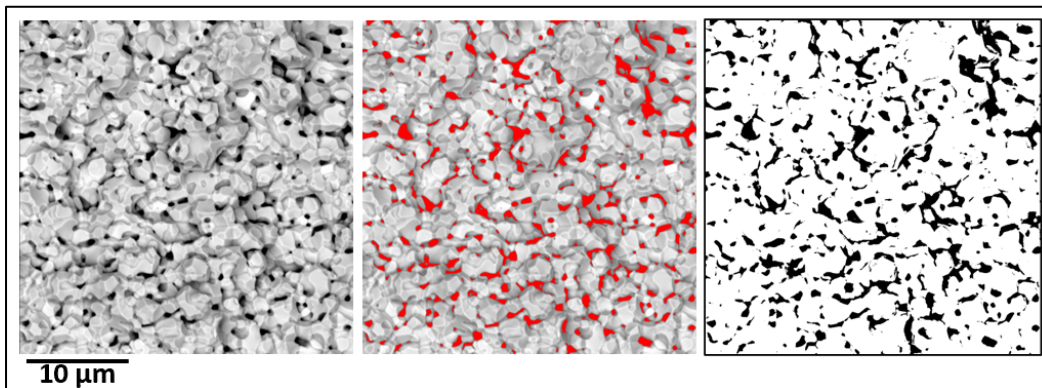
Conversion 2.14=100μm

Circle#	Grid diameter	Perimeter L_i [μm]	N_i	N_{Li}	\bar{L}_3 [μm]
1	5.33	782	28	3.58E-02	27.9
2	4.39	644	19	2.95E-02	33.9
3	3.60	528	19	3.60E-02	27.8
4	2.82	414	16	3.86E-02	25.9
5	1.96	288	8	2.78E-02	36.0
6	5.14	755	26	3.45E-02	29.0
7	4.58	672	23	3.42E-02	29.2
8	3.78	555	19	3.42E-02	29.2
9	2.89	424	16	3.77E-02	26.5
10	2.24	329	12	3.65E-02	27.4
Average from 10 circle grid placements					29.3
Standard deviation					3.2



- **Micrograph from a fracture surface of FGW_HP1500C**

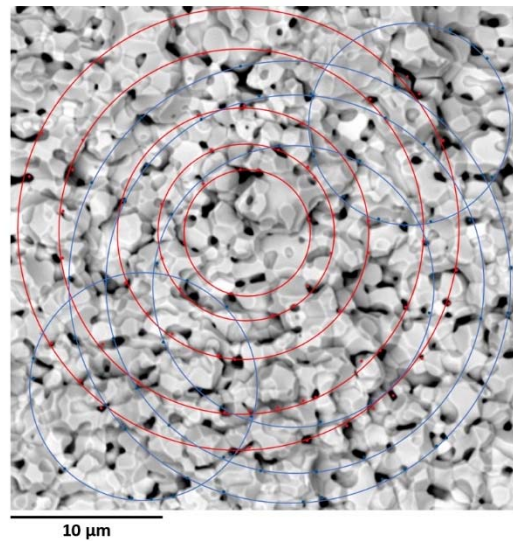
For the case of having present of pores in the micrograph, volume of pore per unit volume can be estimated by finding area of pore per unit area, $V_V = A_A$ [34]. ImageJ software was used to apply thresholding to the pore area as shown in the below image.



The percent area of the black region on the RHS image as determined by the software is 14.0%. Hence, $V_{V,pore} \approx A_{A,pore} = 0.14$. This means the specimen contained about 14% porosity. Average pore size can be determined in terms of \bar{L}_3 . For the case of isolated particles $\bar{L}_{3,pore} = \frac{V_{v,pore}}{N_{L,pore}}$ [34].

Conversion 1.98=10 μ m

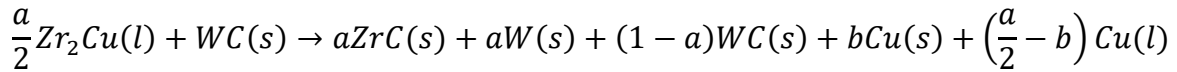
Circle#	Grid diameter	Perimeter L_i [μ m]	N_i	N_{Li}	$\bar{L}_{3,pore}$ [μ m]
1	5.80	92	19	2.06E-01	0.7
2	4.79	76	19	2.50E-01	0.6
3	3.30	52	12	2.29E-01	0.6
4	2.32	37	12	3.26E-01	0.4
5	1.66	26	7	2.66E-01	0.5
6	5.80	92	20	2.17E-01	0.6
7	4.96	79	17	2.16E-01	0.6
8	3.70	59	12	2.04E-01	0.7
9	2.64	42	11	2.63E-01	0.5
10	2.99	47	10	2.11E-01	0.7
Average from 10 circle grid placements					0.6
Standard deviation					0.1



APPENDIX C. SUPPLEMENTARY MATERIALS FOR CHAPTER 3: LIQUID PHASE BONDING OF ZrC/W TO ZrC/W WITH NICKEL- INTERLAYER

C1. Calibration X-ray analysis and mass change data to determine phase content of the ZrC/W-based composited produced via “an *in-situ* alloying, single-step, static melt infiltration” method

During the single step melt infiltration, Zr_2Cu liquid reacted with the WC preform to form ZrC and W following this reaction [8], [19];



On the product side, the solid copper was the copper remained in the specimen, and the liquid copper was the portion that get pushed out upon the pore filling reaction ($WC \rightarrow ZrC + W$). Since not all WC was converted to W. Parameter $a/(1-a)$ which is the molar ratio of W/WC is an indicator of an extent of the reaction. X-ray analysis of the converted specimen can be used to determine the molar ratio of W/WC by dividing ratio of an area under W(110) peak and WC(100) peak by slope of the calibration curved determined in the study by Lipke, et al. [19]. After the parameter a was obtained, the parameter b can be determined by this following equation [19].

$$\frac{\Delta m}{m_o} = \frac{[aMW_{ZrC} + aAW_W + (1 - a)MW_{WC} + bAW_{Cu}] - MW_{WC}}{MW_{WC}}$$

Where m_o is a mass of the WC preform (before the infiltration), Δm is a weight change upon reactive infiltration, MW, or AW is molecular weight or atomic weight of the corresponding component. Hence, by measuring weight change after the reactive melt infiltration, and obtain XRD pattern from the converted specimen. Parameters a and b can be determined. These parameters can be used to quantify phase content via the relationship as shown in the first equation.

For the ZrC/W-based composite that was used in this study, $\frac{\Delta m}{m_o} = 0.62$, and $\frac{A_{W(110)}}{A_{WC(100)}} = \frac{0.3029}{0.02403}$; hence, the phase content of 51.9 vol% ZrC, 32.3 vol% W, 2.0 vol% WC, and 13.8 vol% Cu was obtained.

C2. Weight loss of DCP-derived ZrC/W composite specimens as a function of annealing time at 1100 °C in Ar atmosphere

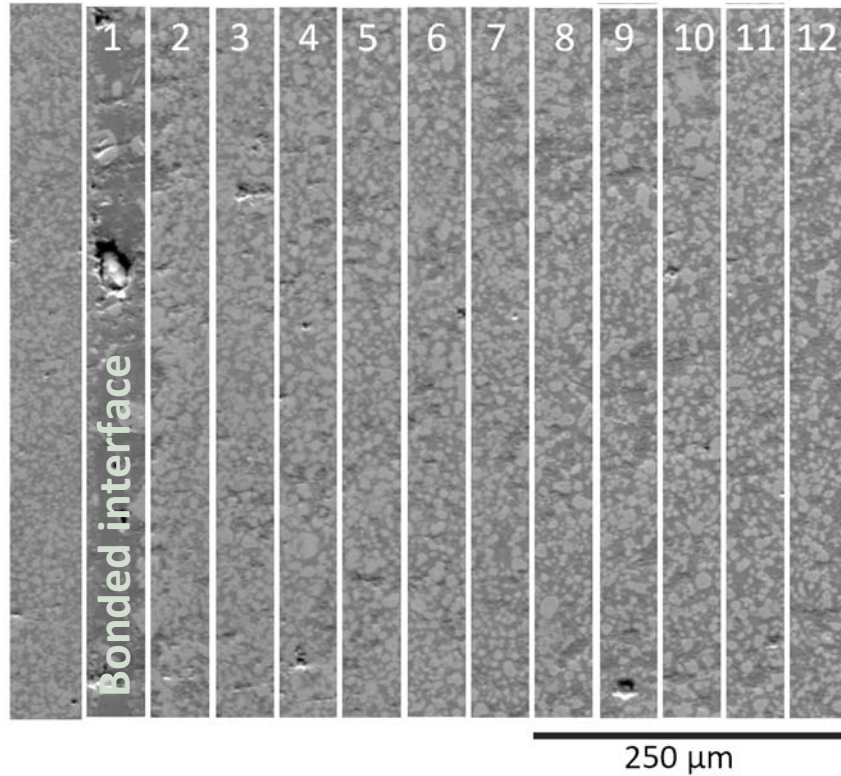
Specimen ID	Total Annealing time@ 1000°C [hour]	$\Delta W_{\text{int-AE}}^*$ (%)
9	2	0.22
10	2	0.32
11	2	0.44
average		0.33
stdv		0.11
17	4	0.20
18	4	0.18
19	4	0.16
20	4	0.17
average		0.18
stdv		0.02
22	6	0.27
23	6	0.28
24	6	0.20
average		0.25
stdv		0.04
25	10	0.24
26	10	0.20
27	10	0.32
average		0.25
stdv		0.06
18	(4+6) = 10	0.26
19	(4+6) = 10	0.23
20	(4+6) = 10	0.24
average		0.24
stdv		0.02

Specimen ID	Total Annealing time@ 1000°C [hour]	$\Delta W_{\text{int-AE}}^*$ (%)
23	(6+10) = 16	0.43
24	(6+10) = 16	0.34
average		0.39
stdv		0.06
18	(4+6+10) = 20	0.38
19	(4+6+10) = 20	0.37
20	(4+6+10) = 20	0.37
average		0.38
stdv		0.01
28	20	0.34
29	20	0.36
30	20	0.39
average		0.36
stdv		0.03
25	(10+20) = 30	0.34
26	(10+20) = 30	0.36
27	(10+20) = 30	0.56
average		0.42
stdv		0.12
18	(4+6+10+20) = 40	0.46
19	(4+6+10+20) = 40	0.43
20	(4+6+10+20) = 40	0.47
average		0.45
stdv		0.02

$$*\Delta W_{\text{int-AE}} = \frac{\text{Initial weight} - \text{weight after etching}}{\text{initial weight}} \times 100$$

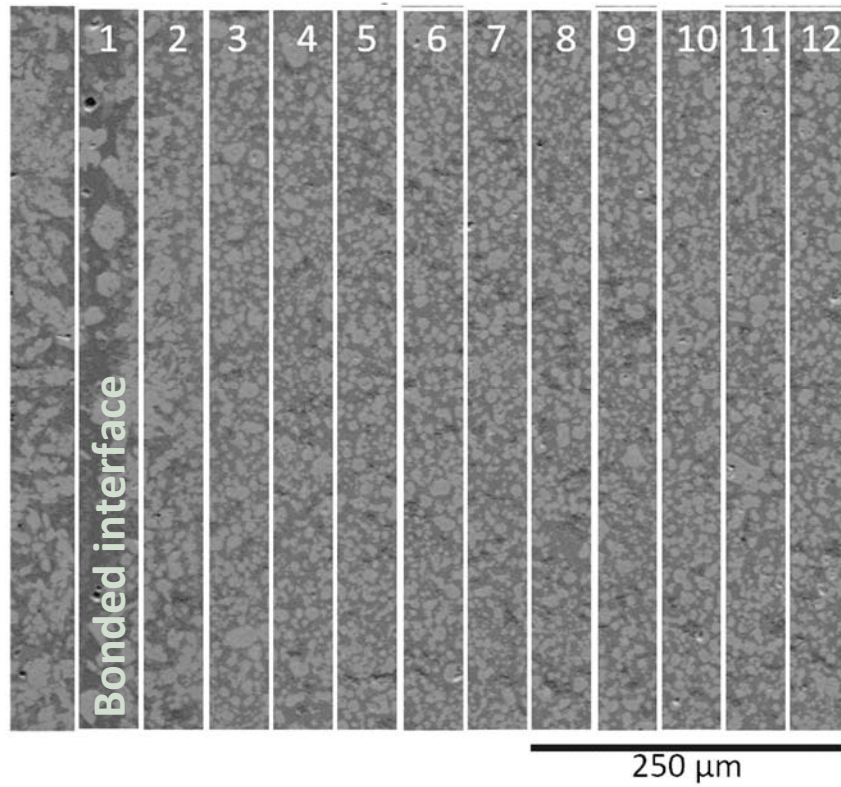
C3. Distribution of elements away from the jointed area from ZrC/W specimens bonded at different temperatures as measured by EDX analysis

- From cross-section of specimen bonded at 1300 °C



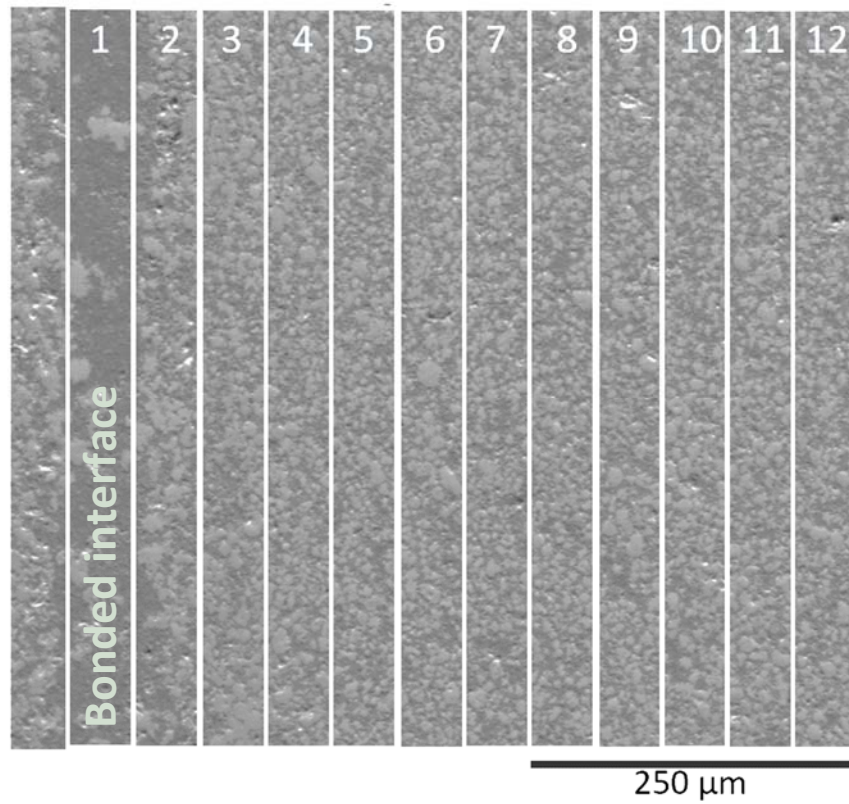
Box#	Distance	Composition (At%)				
		C	Ni	Cu	Zr	W
1	0	25	24	27	17	8
2	50	29	20	11	20	21
3	100	37	12	4	27	19
4	150	39	11	3	27	19
5	200	39	10	3	29	20
6	250	39	9	4	29	20
7	300	39	7	5	30	19
8	350	41	4	4	32	19
9	400	41	3	5	32	18
10	450	42	2	3	33	20
11	500	42	2	4	33	19
12	550	40	2	6	34	18

- From cross-section of specimen bonded at 1400 °C



Box#	Distance	Composition (At%)				
		C	Ni	Cu	Zr	W
1	0	28	14	32	14	12
2	50	34	11	15	19	20
3	100	39	8	8	25	20
4	150	44	3	5	30	19
5	200	45	1	4	31	19
6	250	44	1	5	30	20
7	300	44	1	5	31	19
8	350	45	1	6	30	18
9	400	44	1	7	30	18
10	450	44	1	4	31	20
11	500	44	1	6	30	19
12	550	44	1	6	30	19

- From cross-section of specimen bonded at 1500 °C



Box#	Distance	Composition (At%)				
		C	Ni	Cu	Zr	W
1	0	33	13	24	22	8
2	50	39	8	8	26	19
3	100	39	7	4	27	22
4	150	42	3	3	29	22
5	200	42	2	4	31	22
6	250	41	2	3	31	23
7	300	41	3	4	30	22
8	350	42	3	4	29	22
9	400	41	3	3	30	23
10	450	41	4	4	28	22
11	500	42	3	4	29	23
12	550	42	2	4	30	22

C4. Composition at the bonded interface regions for different bonding temperatures as measured by EDX analysis

- The measurement was made on regions containing bonded interface (like Box#1 in the previous section) from five locations on each specimen.

1300°C	Composition (At%)				
Box#	C	Ni	Cu	Zr	W
1-1	23	25	29	13	10
1-2	27	22	29	14	8
1-3	26	23	29	14	8
1-4	25	24	26	16	10
1-5	29	22	22	19	8
average	26	23	27	15	9
stdv	2	1	3	2	1

1400°C	Composition (At%)				
Box#	C	Ni	Cu	Zr	W
1-1	30	14	31	13	11
1-2	28	15	34	13	10
1-3	27	17	35	12	9
1-4	27	18	30	16	8
1-5	32	13	29	17	10
average	29	16	32	14	10
stdv	2	2	3	2	1

1500°C	Composition (At%)				
Box#	C	Ni	Cu	Zr	W
1-1	36	12	23	21	8
1-2	32	14	26	19	8
1-3	32	14	27	18	9
1-4	33	12	29	20	7
1-5	33	14	27	19	7
average	33	13	26	19	8
stdv	2	1	2	1	1

REFERENCES

- [1] L. Zhou, M. A. Dayananda, and Y. H. Sohn, “Chapter 4 - Diffusion in Multicomponent Alloys,” in *Handbook of Solid State Diffusion, Volume 1*, A. Paul and S. Divinski, Eds. Elsevier, 2017, pp. 203–237.
- [2] M. A. Dayananda and Y. H. Sohn, “A new analysis for the determination of ternary interdiffusion coefficients from a single diffusion couple,” *Metallurgical and Materials Transactions*, vol. 30A, no. 3, p. 535, Mar. 1999.
- [3] S. Liu *et al.*, “Effect of interactions between elements on the diffusion of solutes in NiXY systems and γ' -coarsening in model Ni-based superalloys,” *Scripta Materialia*, vol. 138, pp. 100–104, Sep. 2017, doi: 10.1016/j.scriptamat.2017.05.036.
- [4] X. Xu, N. Zhu, W. Zheng, and X.-G. Lu, “Experimental and computational study of interdiffusion for fcc Ni–Cu–Cr alloys,” *Calphad*, vol. 52, pp. 78–87, Mar. 2016, doi: 10.1016/j.calphad.2015.12.002.
- [5] Y. Wang, J. Wang, H. Wang, X.-G. Lu, and L. Zhang, “Thermodynamic description of the Ni-Mo-W system and interdiffusion study of its fcc phase,” *Calphad*, vol. 61, pp. 165–172, Jun. 2018, doi: 10.1016/j.calphad.2018.03.010.
- [6] J. Wang, Y. Wang, N. Zhu, and X.-G. Lu, “Experimental and Computational Study of Interdiffusion for fcc Ni-Co-W Alloys,” *J. Phase Equilib. Diffus.*, vol. 38, no. 1, pp. 37–50, Feb. 2017, doi: 10.1007/s11669-016-0513-8.
- [7] S. V. Divinski, A. V. Pokoev, N. Esakkiraja, and A. Paul, “A Mystery of ‘Sluggish Diffusion’ in High-Entropy Alloys: The Truth or a Myth?,” *Diffusion Foundations*, 2018. <https://www.scientific.net/DF.17.69> (accessed Dec. 17, 2020).
- [8] M. Caccia *et al.*, “Ceramic–metal composites for heat exchangers in concentrated solar power plants,” *Nature*, vol. 562, no. 7727, pp. 406–409, Oct. 2018, doi: 10.1038/s41586-018-0593-1.
- [9] J. Dąbrowa, W. Kucza, G. Cieślak, T. Kulik, M. Danielewski, and J.-W. Yeh, “Interdiffusion in the FCC-structured Al-Co-Cr-Fe-Ni high entropy alloys: Experimental studies and numerical simulations,” *Journal of Alloys and Compounds*, vol. 674, pp. 455–462, Jul. 2016, doi: 10.1016/j.jallcom.2016.03.046.
- [10] E. L. Semenova, “Chromium – Nickel – Tungsten,” p. 18, 2010.
- [11] H. J. Lee, H. Kim, D. Kim, and C. Jang, “Microstructure evolution of a Ni–Cr–W superalloy during long-term aging at high temperatures,” *Materials Characterization*, vol. 106, pp. 283–291, Aug. 2015, doi: 10.1016/j.matchar.2015.06.018.

- [12] R. Hu, X. L. Meng, B. Tang, C. Y. Wang, H. C. Kou, and J. S. Li, “Interfacial Microstructure Investigation of Diffusion Bonded New Ni-Cr-W Superalloy Using Cu Interlayer,” *Advanced Materials Research*, vol. 634–638, pp. 1844–1849, Jan. 2013, doi: 10.4028/www.scientific.net/AMR.634-638.1844.
- [13] C. Zhang, L. Zhang, Y. Cui, Q. Feng, and C. Cheng, “Effects of High-Temperature Aging on Precipitation and Corrosion Behavior of a Ni-Cr-Mo-Based Hastelloy C276 Superalloy,” *J. of Materi Eng and Perform*, vol. 29, no. 3, pp. 2026–2034, Mar. 2020, doi: 10.1007/s11665-020-04723-y.
- [14] R.-F. Dong, T.-B. Zhang, R. Hu, H.-C. Kou, and J.-S. Li, “Hot corrosion behavior and mechanical properties degradation of a Ni–Cr–W-based superalloy,” *Rare Met.*, vol. 36, no. 1, pp. 23–31, Jan. 2017, doi: 10.1007/s12598-016-0751-2.
- [15] A. F. Rowcliffe, L. K. Mansur, D. T. Hoelzer, and R. K. Nanstad, “Perspectives on radiation effects in nickel-base alloys for applications in advanced reactors,” *Journal of Nuclear Materials*, vol. 392, no. 2, pp. 341–352, Jul. 2009, doi: 10.1016/j.jnucmat.2009.03.023.
- [16] V. B. Kireev, N. V. Kolyasnikova, and V. V. Matyushenko, “Effect of composition on the formation of the sigma-phase in nickel alloys,” *Met Sci Heat Treat*, vol. 31, no. 12, pp. 892–895, Dec. 1989, doi: 10.1007/BF00798232.
- [17] R. Tanaka *et al.*, “Strengthening Factors and Phase Relation in Ni-Cr-W Alloys Developed for Nuclear Steelmaking,” in *Superalloys 1980 (Fourth International Symposium)*, 1980, pp. 481–490, doi: 10.7449/1980/Superalloys_1980_481_490.
- [18] V. Firouzdar, K. Sridharan, G. Cao, M. Anderson, and T. R. Allen, “Corrosion of a stainless steel and nickel-based alloys in high temperature supercritical carbon dioxide environment,” *Corrosion Science*, vol. 69, pp. 281–291, Apr. 2013, doi: 10.1016/j.corsci.2012.11.041.
- [19] D. W. Lipke, Y. Zhang, Y. Liu, B. C. Church, and K. H. Sandhage, “Near net-shape/net-dimension ZrC/W-based composites with complex geometries via rapid prototyping and Displacive Compensation of Porosity,” *Journal of the European Ceramic Society*, vol. 30, no. 11, pp. 2265–2277, Aug. 2010, doi: 10.1016/j.jeurceramsoc.2010.01.011.
- [20] A. Kodentsov and A. Paul, “Chapter 6 - Diffusion Couple Technique: A Research Tool in Materials Science,” in *Handbook of Solid State Diffusion, Volume 2*, A. Paul and S. Divinski, Eds. Elsevier, 2017, pp. 207–275.
- [21] A. Paul, “Chapter 3 - Estimation of Diffusion Coefficients in Binary and Pseudo-Binary Bulk Diffusion Couples,” in *Handbook of Solid State Diffusion, Volume 1*, A. Paul and S. Divinski, Eds. Elsevier, 2017, pp. 79–201.
- [22] J. Zhong, L. Chen, and L. Zhang, “High-throughput determination of high-quality interdiffusion coefficients in metallic solids: a review,” *J Mater Sci*, vol. 55, no. 24, pp. 10303–10338, Aug. 2020, doi: 10.1007/s10853-020-04805-1.

- [23] A. Paul, T. Laurila, V. Vuorinen, and S. V. Divinski, “Interdiffusion in Multicomponent Systems,” in *Thermodynamics, Diffusion and the Kirkendall Effect in Solids*, A. Paul, T. Laurila, V. Vuorinen, and S. V. Divinski, Eds. Cham: Springer International Publishing, 2014, pp. 387–428.
- [24] K. M. Day, M. A. Dayananda, and L. R. Ram-Mohan, “Determination and assessment of ternary interdiffusion coefficients from individual diffusion couples,” *J Phs Eqil and Diff*, vol. 26, no. 6, pp. 579–590, Dec. 2005, doi: 10.1007/s11669-005-0003-x.
- [25] M. A. Dayananda, “MultiDiflux Program for the Analysis of Multicomponent Diffusion,” presented at the Workshop on High Throughput Analysis of Multicomponent Multiphase Diffusion Data, Gaithersburgh, Maryland, Mar. 2003.
- [26] M. A. Dayananda, “Analysis of Multicomponent Diffusion Couples for Interdiffusion Fluxes and Interdiffusion Coefficients,” *Journal of Phase Equilibria & Diffusion*, vol. 26, no. 5, pp. 441–446, Oct. 2005, doi: 10.1361/154770305X66493.
- [27] M. A. Dayananda, “Average effective interdiffusion coefficients and the Matano plane composition,” *Metallurgical and Materials Transactions A*, vol. 27, no. 9, pp. 2504–2509, Sep. 1996, doi: 10.1007/BF02652344.
- [28] M. A. Dayananda, “Average Effective Interdiffusion Coefficients in Binary and Multicomponent Alloys,” *Defect and Diffusion Forum*, vol. 95–98, pp. 521–536, Jan. 1993, doi: 10.4028/www.scientific.net/DDF.95-98.521.
- [29] M. A. Dayananda and D. A. Behnke, “Effective interdiffusion coefficients and penetration depths,” *Scripta Metallurgica et Materialia*, vol. 25, no. 9, pp. 2187–2191, Sep. 1991, doi: 10.1016/0956-716X(91)90297-E.
- [30] D. Karpinos, “Interaction at the interface in composite materials with a Nichrome matrix and tungsten- and molybdenum-based fibers,” in *Poroshkovaya Metallurgiya (Kiev)*, 1974, pp. 64–75, Accessed: Jan. 08, 2020. [Online].
- [31] S. Inomata and M. Kajihara, “Solid-state reactive diffusion between Ni and W,” *Journal of Alloys and Compounds*, vol. 509, no. 15, pp. 4958–4966, Apr. 2011, doi: 10.1016/j.jallcom.2011.01.139.
- [32] S. V. N. Naidu, A. M. Sriramamurthy, and P. Rama Rao, “Ni-W (Nickel-Tungsten),” *Binary Alloy Phase Diagrams, Second Edition*, Ed. T.B. Massalski, ASM International, Materials Park, Ohio, vol. 3, pp. 2882–2883, 1990.
- [33] K. P. Gupta, “The Cr-Ni-W (chromium-nickel-tungsten) system,” *Phase Diagrams Ternary Nickel Alloys*, *Indian Inst. Metals*, vol. 1, pp. 111–133, 1990.
- [34] E. E. Underwood, “Quantitative Stereology for Microstructural Analysis,” in *Microstructural Analysis: Tools and Techniques*, J. L. McCall and W. M. Mueller, Eds. Boston, MA: Springer US, 1973, pp. 35–66.

- [35] E04 Committee, “Test Methods for Determining Average Grain Size Using Semiautomatic and Automatic Image Analysis,” ASTM International. doi: 10.1520/E1382-97R15.
- [36] S. Ueta, M. Hida, and M. Kajihara, “Effects of Fe, W and Mo on Kinetics of Discontinuous Precipitation in the Ni-Cr System,” *MATERIALS TRANSACTIONS*, vol. 53, no. 10, pp. 1744–1752, 2012, doi: 10.2320/matertrans.M2012132.
- [37] M. Kikuchi, M. Kajihara, Y. Kadoya, and R. Tanaka, “Decomposition of sigma phase in a Ni□Cr□W system,” *Scripta Metallurgica*, vol. 17, no. 4, pp. 475–478, Apr. 1983, doi: 10.1016/0036-9748(83)90335-6.
- [38] E. Clementi and D. L. Raimondi, “Atomic Screening Constants from SCF Functions,” *J. Chem. Phys.*, vol. 38, no. 11, pp. 2686–2689, Jun. 1963, doi: 10.1063/1.1733573.
- [39] “Reade Advanced Materials - Nickel-Chromium Alloys (NiCr).” <https://www.reade.com/products/metal-alloy-non-metallic-minerals-ceramic-composite-polymer-powder-sheet-foil-rod-natural-fiber-metal-fiber-nanowire-nanoparticle-nanotube-coatings-aerogel-metal-foam-ceramic-foam-enzymes-magnetic-conductive-abrasives-additives/alloys-metal-inorganic-fusible-intermetallic-powder-sheet-a-wire/nickel-chromium-alloys-nicr> (accessed Mar. 11, 2021).
- [40] M. A. Dayananda, G. E. Murch, Metallurgical Society of AIME, and American Society for Metals Atomic Transport Activity, *Diffusion in solids: recent developments*. Warrendale, Pa.: Metallurgical Society, 1984.
- [41] G. W. Roper and D. P. Whittle, “Interdiffusion in ternary Co-Cr-Al alloys,” *Metal Science*, vol. 14, no. 1, pp. 21–28, Jan. 1980, doi: 10.1179/030634580790438136.
- [42] C. N. Singman, “Atomic volume and allotropy of the elements,” *J. Chem. Educ.*, vol. 61, no. 2, p. 137, Feb. 1984, doi: 10.1021/ed061p137.
- [43] A. L. Hurley and M. A. Dayananda, “Multiphase diffusion in Ag-Zn alloys,” *Metall Mater Trans B*, vol. 1, no. 1, pp. 139–143, Jan. 1970, doi: 10.1007/BF02819253.
- [44] R. D. Sisson and M. A. Dayananda, “Diffusion structures in multiphase Cu-Ni-Zn couples,” *Metall Mater Trans B*, vol. 3, no. 3, pp. 647–652, Mar. 1972, doi: 10.1007/BF02642746.
- [45] Harteck, “Diffusion in Solids, Liquids, Gases, von W. Jost. Academic Press Inc., New York 1952. XI, 558 S., geb. \$ 12.–,” *Angewandte Chemie*, vol. 65, no. 19, pp. 496–496, 1953, doi: <https://doi.org/10.1002/ange.19530651912>.
- [46] L. S. Darken, *Trans. Amer. Inst. Min. (Metall.) Engrs.*, vol. 175, p. 184, 1948.
- [47] Murazen, “Metals Data Book,” Japan Institute of Metals and Materials, 2000, pp. 21–23.
- [48] J. Chen, J. Xiao, L. Zhang, and Y. Du, “Interdiffusion in fcc Ni-X (X = Rh, Ta, W, Re and Ir) alloys,” *Journal of Alloys and Compounds*, vol. 657, pp. 457–463, Feb. 2016, doi: 10.1016/j.jallcom.2015.10.120.

- [49] J. Zhang *et al.*, “Ultrafine Grain Tungsten Heavy Alloys with Excellent Performance Prepared by Spark Plasma Sintering,” *J. Wuhan Univ. Technol.-Mat. Sci. Edit.*, vol. 35, no. 2, pp. 393–398, Apr. 2020, doi: 10.1007/s11595-020-2269-6.
- [50] N. Senthilnathan, A. R. Annamalai, and G. Venkatachalam, “Synthesis of tungsten through spark plasma and conventional sintering processes,” *Materials Today: Proceedings*, vol. 5, no. 2, Part 2, pp. 7954–7959, Jan. 2018, doi: 10.1016/j.matpr.2017.11.478.
- [51] C. Ren, Z. Z. Fang, H. Zhang, and M. Koopman, “The study on low temperature sintering of nano-tungsten powders,” *International Journal of Refractory Metals and Hard Materials*, vol. 61, pp. 273–278, Dec. 2016, doi: 10.1016/j.ijrmhm.2016.10.003.
- [52] R. M. German, *Particulate Composites: Fundamentals and Applications*. Springer International Publishing, 2016.
- [53] C. Ren, M. Koopman, Z. Zak Fang, H. Zhang, and B. van Devenner, “A study on the sintering of ultrafine grained tungsten with Ti-based additives,” *International Journal of Refractory Metals and Hard Materials*, vol. 65, pp. 2–8, Jun. 2017, doi: 10.1016/j.ijrmhm.2016.11.013.
- [54] G. K. Williamson and W. H. Hall, “X-ray line broadening from filed aluminium and wolfram,” *Acta Metallurgica*, vol. 1, no. 1, pp. 22–31, Jan. 1953, doi: 10.1016/0001-6160(53)90006-6.
- [55] H. Wang, Z. Z. Fang, K. S. Hwang, H. Zhang, and D. Siddle, “Sinter-ability of nanocrystalline tungsten powder,” *International Journal of Refractory Metals and Hard Materials*, vol. 28, no. 2, pp. 312–316, Mar. 2010, doi: 10.1016/j.ijrmhm.2009.11.003.
- [56] R. Malewar, K. S. Kumar, B. S. Murty, B. Sarma, and S. K. Pabi, “On sinterability of nanostructured W produced by high-energy ball milling,” *Journal of Materials Research*, vol. 22, no. 5, pp. 1200–1206, May 2007, doi: 10.1557/jmr.2007.0166.
- [57] S. Deng, T. Yuan, R. Li, F. Zeng, G. Liu, and X. Zhou, “Spark plasma sintering of pure tungsten powder: Densification kinetics and grain growth,” *Powder Technology*, vol. 310, pp. 264–271, Apr. 2017, doi: 10.1016/j.powtec.2017.01.050.
- [58] J. Choi, H.-M. Sung, K.-B. Roh, S.-H. Hong, G.-H. Kim, and H. N. Han, “Fabrication of sintered tungsten by spark plasma sintering and investigation of thermal stability,” *International Journal of Refractory Metals and Hard Materials*, vol. 69, pp. 164–169, Dec. 2017, doi: 10.1016/j.ijrmhm.2017.08.013.
- [59] Y. P. Yu, S. Wang, and W. Li, “Research Progress of W/ZrC Ultra-High Temperature Cermets,” *Applied Mechanics and Materials*, 2014. <https://www.scientific.net/AMM.624.152> (accessed Aug. 12, 2020).

- [60] M. B. Dickerson, P. J. Wurm, J. R. Schorr, W. P. Hoffman, P. G. Wapner, and K. H. Sandhage, "Near net-shape, ultra-high melting, recession-resistant ZrC/W-based rocket nozzle liners via the displacive compensation of porosity (DCP) method," *Journal of Materials Science*, vol. 39, no. 19, pp. 6005–6015, Oct. 2004, doi: 10.1023/B:JMSC.0000041697.67626.46.
- [61] G.-M. Song, Y.-J. Wang, and Y. Zhou, "The mechanical and thermophysical properties of ZrC/W composites at elevated temperature," *Materials Science and Engineering: A*, vol. 334, no. 1–2, pp. 223–232, Sep. 2002, doi: 10.1016/S0921-5093(01)01802-0.
- [62] G.-M. Song, Y. Zhou, and Y.-J. Wang, "Effect of carbide particles on the ablation properties of tungsten composites," *Materials Characterization*, vol. 50, no. 4, pp. 293–303, Jun. 2003, doi: 10.1016/S1044-5803(03)00123-2.
- [63] J.-H. Kim, M. Seo, and S. Kang, "Effect of carbide particle size on the properties of W–ZrC composites," *International Journal of Refractory Metals and Hard Materials*, vol. 35, pp. 49–54, Nov. 2012, doi: 10.1016/j.ijrmhm.2012.03.010.
- [64] M. Roosta, H. Baharvandi, and H. Abdizade, "The evaluation of W/ZrC composite fabricated through reaction sintering of two precursors: Conventional ZrO₂/WC and novel ZrSiO₄/WC," *International Journal of Refractory Metals and Hard Materials*, vol. 29, no. 6, pp. 710–715, Nov. 2011, doi: 10.1016/j.ijrmhm.2011.04.017.
- [65] Z. R. Li, J. C. Feng, and J. Cao, "Vacuum diffusion bonding of TiB₂ cermet to TiAl based alloys," *Materials Science and Technology*, vol. 20, no. 12, pp. 1666–1668, Dec. 2004, doi: 10.1179/026708304225016798.
- [66] K. Feng, H. Chen, J. Xiong, and Z. Guo, "Investigation on diffusion bonding of functionally graded WC–Co/Ni composite and stainless steel," *Materials & Design*, vol. 46, pp. 622–626, Apr. 2013, doi: 10.1016/j.matdes.2012.11.006.
- [67] M. Lei, Y. Li, and H. Zhang, "Interfacial microstructure and mechanical properties of the TiC–Ni cermet/Ag–Cu–Zn/Invar joint," *Vacuum*, vol. 168, p. 108830, Oct. 2019, doi: 10.1016/j.vacuum.2019.108830.
- [68] G. H. Han *et al.*, "Interfacial microstructure and mechanical properties of TZM alloy and ZrC particle reinforced tungsten composite joint brazed using Ti–61Ni filler," *Journal of Alloys and Compounds*, vol. 747, pp. 266–275, May 2018, doi: 10.1016/j.jallcom.2018.02.258.
- [69] D. Ye, W. Xiong, X. Zhang, J. Qu, and Z. Yao, "Microstructure and shear strength of the brazed joint of Ti(C,N)-based cermet to steel," *Rare Metals*, vol. 29, no. 1, pp. 72–77, Feb. 2010, doi: 10.1007/s12598-010-0013-7.
- [70] Z. Zhong, H. Jung, T. Hinoki, and A. Kohyama, "Effect of joining temperature on the microstructure and strength of tungsten/ferritic steel joints diffusion bonded with a nickel interlayer," *Journal of Materials Processing Technology*, vol. 210, no. 13, pp. 1805–1810, Oct. 2010, doi: 10.1016/j.jmatprotec.2010.06.012.

- [71] S. B. Dunkerton, “Diffusion Bonding — An Overview,” in *Diffusion Bonding 2*, Springer, Dordrecht, 1991, pp. 1–12.
- [72] “Nickel 200&201.” specialmetals.com, [Online]. Available: <https://www.specialmetals.com/assets/smc/documents/alloys/nickel-duranickel/nickel-200-201.pdf>.
- [73] W. F. Gale and D. A. Butts, “Transient liquid phase bonding,” *Science and Technology of Welding and Joining*, vol. 9, no. 4, pp. 283–300, Aug. 2004, doi: 10.1179/136217104225021724.
- [74] W. D. MucDonald and T. W. Eagar, “TRANSIENT LIQUID PHASE BONDING,” p. 24.
- [75] G. O. Cook and C. D. Sorensen, “Overview of transient liquid phase and partial transient liquid phase bonding,” *J Mater Sci*, vol. 46, no. 16, pp. 5305–5323, Aug. 2011, doi: 10.1007/s10853-011-5561-1.
- [76] J. R. Holaday and C. A. Handwerker, “Transient Liquid Phase Bonding,” in *Die-Attach Materials for High Temperature Applications in Microelectronics Packaging: Materials, Processes, Equipment, and Reliability*, K. S. Siow, Ed. Cham: Springer International Publishing, 2019, pp. 197–249.
- [77] G. P. Dmitrieva and A. K. Shurin, “Investigation of the phase equilibria and structures in alloys Ni-ZrC and Ni-HfC,” *Metallofizika (Akademiya Nauk Ukrainskoi SSR, Institut Metallofiziki)*, vol. 53, pp. 97–100, 1974.
- [78] W. Wang, D. Fan, J. Huang, C. Li, J. Yang, and S. Chen, “Microstructural mechanism and mechanical properties of Cf/SiC composite/TC4 alloy joints composite-diffusion brazed with TiZrCuNi + TiCp composite filler,” *Materials Science and Engineering: A*, vol. 728, pp. 1–9, Jun. 2018, doi: 10.1016/j.msea.2018.04.091.
- [79] W. Wang, J. Huang, Y. Wang, J. Yang, S. Chen, and X. Zhao, “A novel process with the characteristics of low-temperature bonding and high-temperature resisting for joining Cf/SiC composite to GH3044 alloy,” *Journal of the European Ceramic Society*, vol. 39, no. 16, pp. 5468–5472, Dec. 2019, doi: 10.1016/j.jeurceramsoc.2019.08.031.
- [80] D. J. Chakrabarti, D. E. Laughlin, S. W. Chen, and Y. A. Chang, “Cu-Ni (Copper-Nickel),” *Binary Alloy Phase Diagrams, Second Edition, Ed. T.B. Massalski, ASM International, Materials Park, Ohio*, vol. 2, pp. 1442–1446, 1990.
- [81] C. Qiu, Z. Jin, and P. Huang, “Phase equilibria in the W-Ni-Cu system. Pt. 2. Thermodynamic calculation,” *Zeitschrift für Metallkunde*, vol. 79, no. 12, pp. 767–769, 1988.
- [82] S. V. N. Naidu, A. M. Sriramamurthy, and P. R. Rao, “The nickel-tungsten system,” *Journal of Alloy Phase Diagrams*, vol. 2, pp. 1–11, 1986.